Chapter 9

Application of the Simultaneous Transformation Model

The individual phase transformation models described in Chapter 6 were each converted to the simultaneous transformation kinetics method and combined together in turn. At each stage, the combined model was validated on experimental data, to ensure the competition now allowed between the phases still produced the correct transformation behaviour. The allotriomorphic ferrite and pearlite models were amalgamated first, then Widmanstätten ferrite was added, before bainite and martensite were finally included.

9.1 Allotriomorphic Ferrite Model

The evolution of volume fraction as a function of time and temperature, and the ferrite grain size are the key parameters of the allotriomorphic ferrite transformation which can be readily validated against experimental data. The heterogeneous nucleation rate equation contains adjustable values for the density of nucleation sites and the interfacial energy shape factors for the three types of boundary site. A number of fitting parameters are required since important quantities such as interfacial energy at the nucleation stage are unknown. However, the aim was to produce just one set of parameters applicable to "all steels" and conditions. Comparisons were made between calculated and experimental volume fraction and grain size results.

9.1.1 Nucleation Rate Equation Parameters

From classical nucleation theory, as derived in Section 3.1.4, we have for the rate per unit area of boundary:

$$I_b^j = \frac{k_B T}{h} n_s^j \exp\left\{ -\frac{(K_2^j G^* + Q)}{k_B T} \right\} \tag{9.1}$$

where n_s^j is a site factor expressing the density of nucleation sites per unit area of boundary and K_2^j is a shape factor affecting the austenite/ferrite interfacial energy per unit area, $\sigma_{\gamma\alpha}$, according to the type of nucleation site j, where $j = f$ for grain face sites, e for edges and c for corners. Q is an activation energy for self-diffusion of iron, taken as 240 kJ mol^{-1} [50], and $G^* \propto \frac{\sigma_{\gamma\alpha}^3}{\Delta G_v^2}$. Separate rate equations can be written for nucleation at each type of site, and the results combined to give the overall nucleation rate. At different temperatures during cooling, different sites will dominate the transformation. The number of face sites per unit area of boundary is determined by assuming that each atom can act as a site and then halving this number as there are two sides to the boundary. If the atomic spacing is δ, taken as 2.5×10^{-10} m [37], then:

$$n_s^f = K_1^f \frac{1}{2\delta^2} \tag{9.2}$$

where K_1^f is a factor representing the fraction of the total number of face sites that are actually active (for example, nucleation at one site will consume adjacent sites and also prevent others in the vicinity from nucleating due to the carbon diffusion field from the allotriomorph). Following the theory of Christian for site densities per unit volume, [37] in 3.1.4.2, the ratio of face to edge and edge to corner sites is $\frac{\delta}{d_\gamma}$, thus:

$$n_s^e = \frac{K_1^e}{2\delta^2} = \frac{K_1^f}{2\delta^2}\frac{\delta}{d_\gamma} = \frac{K_1^f}{2\delta d_\gamma} \tag{9.3}$$

$$n_s^c = \frac{K_1^c}{2\delta^2} = \frac{K_1^f}{2\delta^2}\left(\frac{\delta}{d_\gamma}\right)^2 = \frac{K_1^f}{2d_\gamma^2} \tag{9.4}$$

where d_γ is the mean lineal intercept austenite grain size. So the fraction of active face nucleation sites is one unknown parameter in the nucleation rate equation.

The other parameter for which a value must be found is the shape factor for each type of site. Clemm and Fisher's equations (3.1.4.3), rely upon the choice of a value for the dihedral angle at grain junctions. Intuitively, it can be seen that the shape factor for faces should be higher than for edges, which in turn is greater than that for corners. Nucleation on a corner site will eliminate a greater area of high energy grain boundary than on an edge or face, for the same amount of matrix/nucleus interfacial energy created. Thus, corner nucleation should be the most energetically favourable and the activation energy barrier to nucleation, G^*, should be lowered accordingly *via* the shape factor. All the shape factors should be less than one, as heterogeneous nucleation is always more favourable than homogeneous nucleation.

Initial calculations were performed with the continuous cooling allotriomorphic ferrite model and the site density and shape factors determined by Reed and Bhadeshia (Table 3.1). They took $\sigma_{\gamma\alpha}$ to be equal to 0.2 J m^{-2} in their calculations. However, it has been proposed by Lange *et al.* in a review of nucleation kinetics theory that the critical nucleus should be surrounded by ostensibly low energy (coherent) interfaces for nucleation to occur at a detectable rate [125]. They compiled interfacial energy values proposed by several researchers, and a value of $\sigma_{\gamma\alpha} = 0.05$ J m^{-2} was chosen from these for the current model. The shape factors therefore had to be adjusted accordingly, to produce values of $K_2^j G^*$ consistent with those of Reed and Bhadeshia. It was also felt that the shape factors should decrease in the order faces > edges > corners, to reflect the increasing potency of these sites. Values of $K_1^f = 1 \times 10^{-9}$ and shape factors of 0.3, 0.1 and 0.01 were taken as a suitable starting point for optimisation of these parameters.

9.1.2 Results from the New Model

The effects of varying the nucleation rate equation parameters on the ferrite transformation are illustrated in this section for a 0.055 C 0.237 Mn wt.% steel (designated HO1) under various conditions. The general trends demonstrated were also observed with all the other steels investigated.

The contributions to the overall boundary nucleation rate from the three types of site vary with undercooling below Ae'_3, as illustrated in Figure 9.1. At temperatures close to Ae'_3, the low activation energy barrier to corner nucleation allows this site to dominate. Edge nucleation then quickly becomes more frequent and takes over, before the larger number density of face sites become active when the undercooling is sufficient to overcome their higher activation barrier. A larger austenite grain size increases the proportion of face sites and thus reduces the contribution from edges and corners accordingly. A slower cooling rate, on the other hand, increases the effect of the corner and edge sites and lowers the temperature at which the face nucleation rate becomes significant.

An increase in the fraction of active face nucleation sites, K_1^f, will increase the nucleation rates at all sites, thus forming a measurable fraction of allotriomorphic ferrite more rapidly and leading to an increase in the ferrite-start temperature, F_s. In the model, this is taken as the temperature at which an allotriomorphic ferrite volume fraction of 0.01 is calculated to have formed. The predicted effect of K_1^f on this temperature at three different cooling rates in steel HO1 is illustrated in Figure 9.2 and is in agreement with

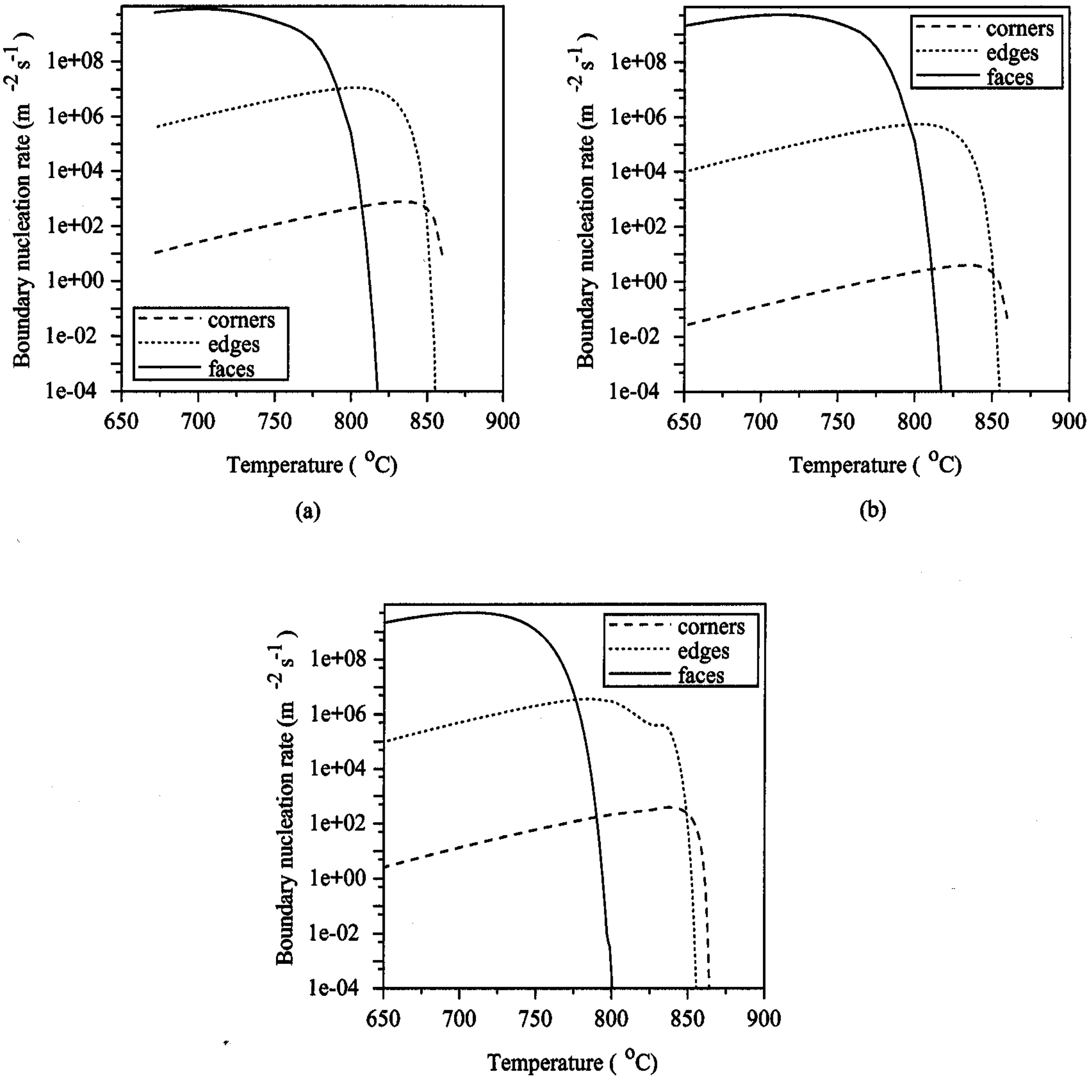

(a)

(b)

(c)

Figure 9.1: Calculated boundary nucleation rates at face, edge and corner sites in steel HO1 at (a) $d_\gamma = 10\,\mu\text{m}$, 10 °C s^{-1}, (b) $d_\gamma = 100\,\mu\text{m}$, 10 °C s^{-1}, and (c) $d_\gamma = 10$ μm, 0.1 °C s^{-1}. Calculated $Ae'_3 = 865$ °C.

this theory. The value of K_1^f also affects the final fraction of allotriomorphic ferrite. At 0.1 °C s^{-1} cooling, the maximum fraction was always obtained for each K_1^f value tested, but at faster cooling rates the amount decreased with the fraction of active sites quite significantly.

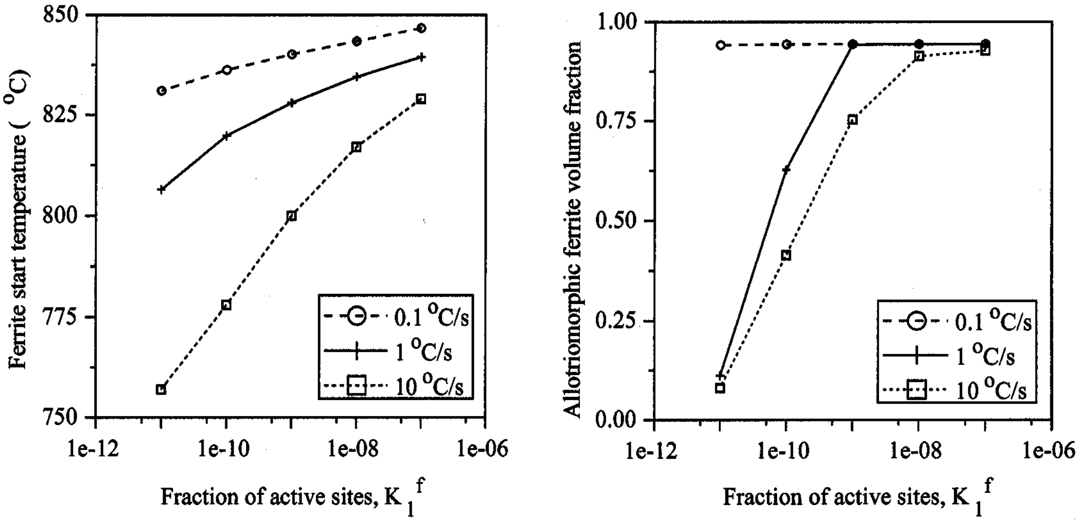

(a) (b)

Figure 9.2: Calculated effect of the fraction of active nucleation sites, K_1^f, in steel HO1 with $d_\gamma = 10\,\mu$m at different cooling rates, on allotriomorphic ferrite (a) start temperature and (b) volume fraction.

The specific effects of the individual shape factors were investigated, by holding two of the factors constant and varying the third. The default values were $K_1^f = 1.0 \times 10^{-9}$, $K_2^f = 0.3$, $K_2^e = 0.1$ and $K_2^c = 0.01$. As suggested by the contributions to the overall nucleation rate by the three sites, the impact of each shape factor will also vary with cooling rate and austenite grain size. Two austenite grain sizes, 100 μm and 10 μm, and three cooling rates, 10, 1 and 0.1 °C s^{-1}, were used. At the large grain size, the number of face sites is proportionally higher and the face shape factor K_2^f was the only one to have an effect on F_s and the allotriomorphic ferrite fraction (Figure 9.3), the former increasing steadily as K_2^f decreased, the latter reaching a maximum and then levelling off. At a smaller austenite grain size, the contribution from the corner shape factor was still negligible but edges began to make a significant difference (Figure 9.4). Reducing both K_2^f and K_2^e increased F_s. The volume fraction went through a maximum as K_2^f decreased, decreasing by about 0.05 as the shape factor and thus the activation barrier for nucleation became smaller. Reducing K_2^e had a smaller effect on volume fraction, leading to an increase of about 0.1. At the small grain size and slower cooling rate, (Figure 9.5), both edge and face sites affected F_s and the volume fraction, causing large increases in both when the face factor was less than 0.5 or the edge factor fell below 0.1. The edge sites have a greater effect at this slower cooling rate compared with 10 °C s^{-1}. Finally, at the slowest cooling rate and the small grain size, the corner sites began to have an effect when the shape factor fell below 0.01, although their effect will likely be swamped by the contributions from the other types of sites. There was no change in the final volume fraction with the shape factors at this slow cooling rate because the equilibrium fraction was achieved for all cases.

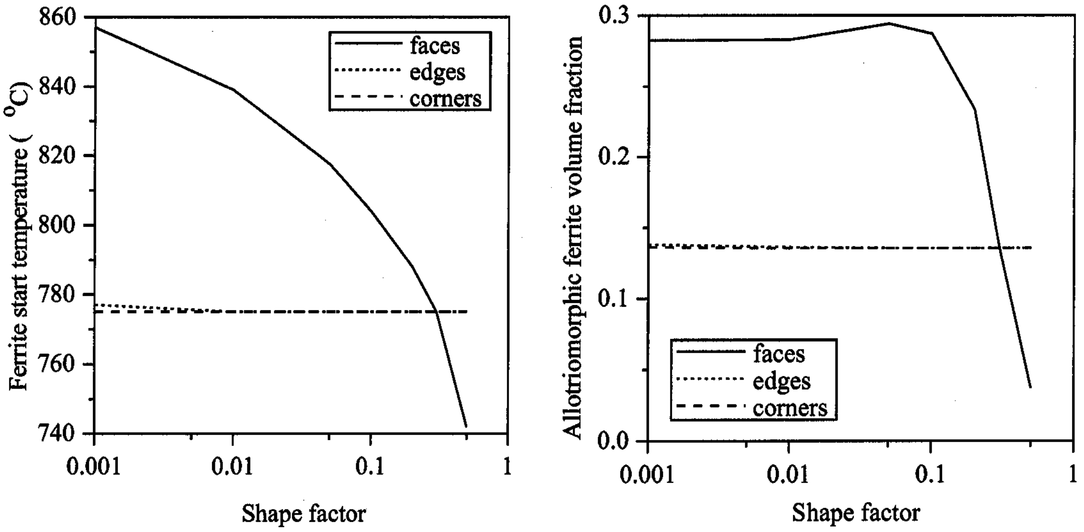

(a)

(b)

Figure 9.3: Calculations for steel HO1 for each shape factor K_2^j at $d_\gamma = 100\ \mu$m and 10 °C s^{-1}, showing effect on (a) ferrite-start temperature and (b) allotriomorphic ferrite volume fraction.

These calculations indicate the effect on the ferrite transformation kinetics of different active site densities and interfacial energy related shape factors for the three types of nucleation site. For a shape factor to have an impact on the transformation kinetics of this steel under these circumstances, it must have a value less than 0.3 for faces, 0.1 for edges and 0.01 for corners. An experimental CCT diagram for this steel showed F_s values of 856 and 836 °C, and ferrite volume fractions of 0.96 and 0.94, at cooling rates of 0.6 and 10 °C s^{-1}, respectively [116]. Figure 9.2 shows that $K_1^f = 1 \times 10^{-9}$ under-estimates the ferrite start temperatures at both cooling rates and the final volume fraction at 10 °C s^{-1}. However, Figure 9.4 and Figure 9.5 indicate that decreasing K_2^f from 0.3 to 0.1 and K_2^e from 0.1 to 0.01 increased both the volume fraction and F_s.

Bearing these results in mind, the model was then tested against different sets of

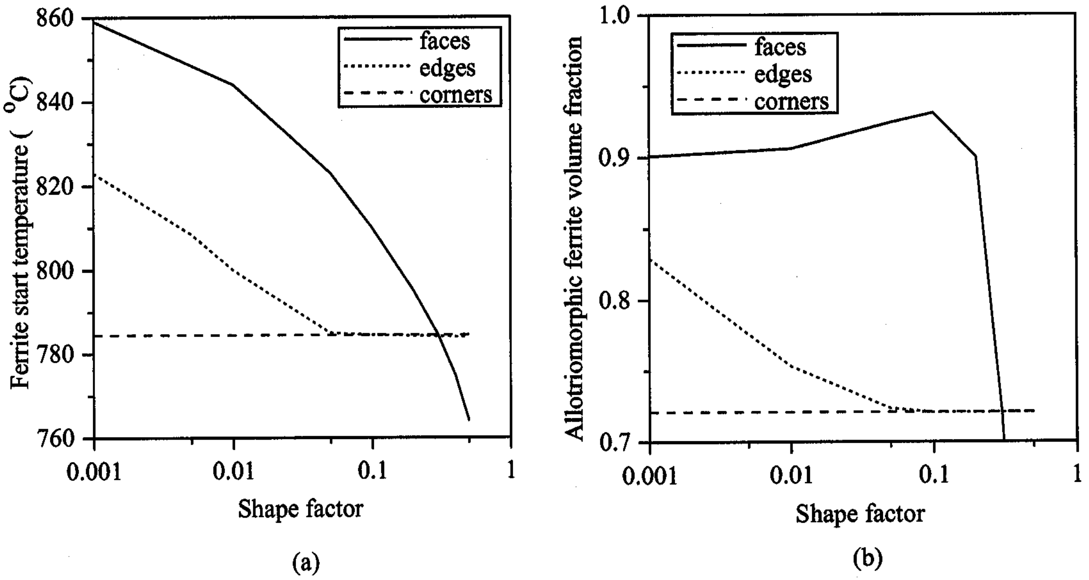

(a)

(b)

Figure 9.4: Calculations for steel HO1 for each shape factor K_2^j at $d_\gamma = 10$ μm and 10 °C s^{-1}, showing effect on (a) ferrite-start temperature and (b) allotriomorphic ferrite volume fraction.

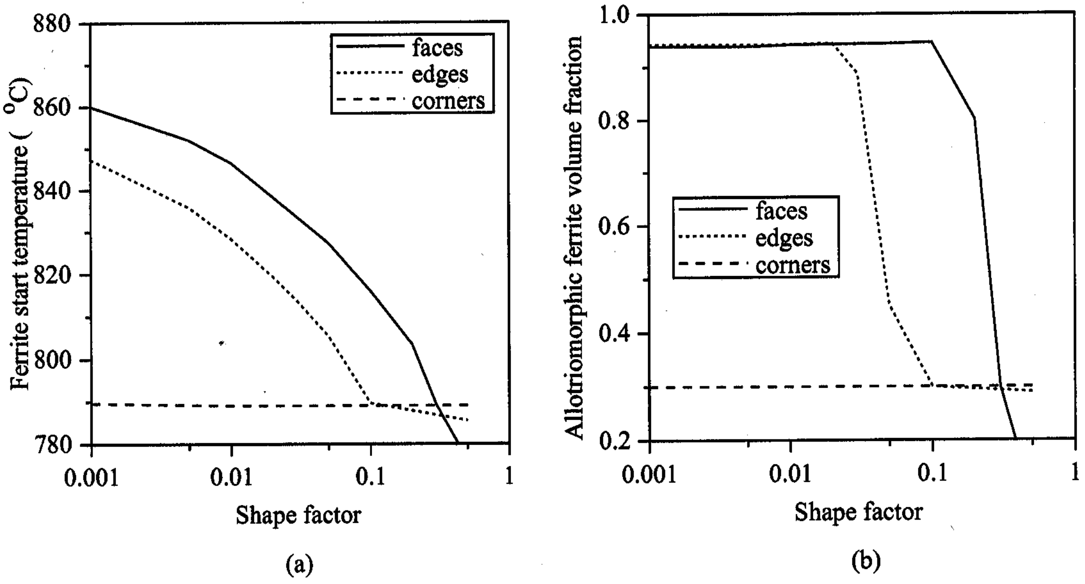

(a)

(b)

Figure 9.5: Calculations for steel HO1 for each shape factor K_2^j at $d_\gamma = 10$ μm and 1 °C s^{-1}, showing effect on (a) ferrite-start temperature and (b) allotriomorphic ferrite volume fraction.

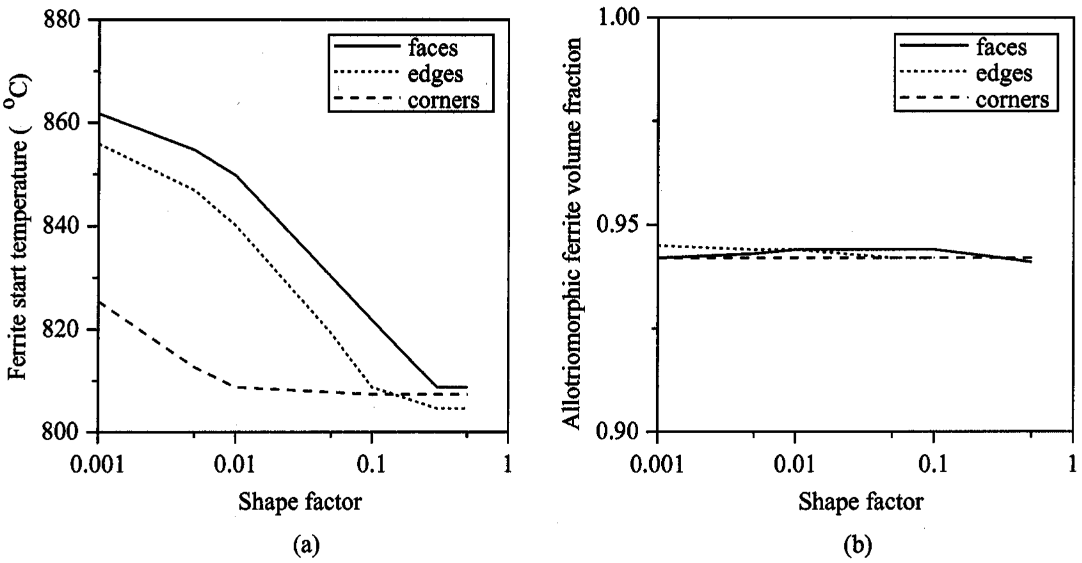

Figure 9.6: Calculations for steel HO1 for each shape factor K_2^j at d_γ = 10 μm and 0.1 °C s^{-1}, showing effect on (a) ferrite-start temperature and (b) allotriomorphic ferrite volume fraction.

experimental data from the literature on the equiaxed ferrite grain size and the evolution of ferrite volume fraction. The values of the site and shape factors were re-evaluated throughout, to find an optimum set of values for all the steels. The final values were selected after incorporation of the Widmanstätten ferrite and pearlite models (Section 9.3.4).

9.1.2.1 Ferrite Grain Size Calculations

The allotriomorphic ferrite grain size was determined from the particle density per unit area, N_s, at the austenite grain boundary when all the boundary had transformed, using equation 3.41:

$$d_\alpha = \left(\frac{2}{3N_sS_v}\right)^{\frac{1}{3}} \tag{9.5}$$

Figure 9.7 shows the variation in d_α with K_1^f for the HO1 steel at 0.1 °C s^{-1}, where the same fraction of allotriomorphic ferrite was formed at each sites value. The grain size decreased steadily as K_1^f increased, because the number density of face sites increases.

The grain size was calculated for a series of commercial steels with compositions and austenite grain sizes as in Table 9.1, at cooling rates of 0.14, 0.96, 2.01 and 32.48 °C s^{-1}, and also for the three steels in Table 9.2 at cooling rates of 1 and 10 °C s^{-1}. Comparisons between calculated and measured results for the steels are shown in Figure 9.8. The experimental results were provided by British Steel [115, 116] and CENIM, Madrid [117].

Grain sizes were measured by the lineal intercept method [112] at magnifications of 500 ×. With the exception of the BS1 results, the errors in the measurements were not quoted. Firstly, considering the BST steels, the agreement between measured and calculated values was good for BST1, the difference being usually less than 10 μm. In BST2, and the higher carbon BST4, 5 and 6, there was a tendency for the model to overestimate the ferrite grain size, by as much as 20 μm in some cases. The results for the BS steels are good, with only a slight over-estimation of the fine grain sizes by a couple of microns.

Steel	C	Si	Mn	Ni/Cr/Cu	Mo/V	Al	austenite grain sizes (μm)
BST1	0.095	0.21	0.84	<0.02	<0.005	0.006	62, 85, 101, 160
BST2	0.097	0.21	1.35	<0.02	<0.005	0.007	38, 57, 104, 290
BST4	0.20	0.20	1.36	<0.02	<0.005	0.006	64, 86, 111, 115
BST5	0.30	0.19	0.83	<0.02	<0.005	0.006	90, 132, 140, 171
BST6	0.31	0.19	1.35	<0.02	<0.005	<0.005	80, 111, 117, 124

Table 9.1: Composition in wt.% of BST steels for which ferrite grain sizes and volume fractions were calculated [115].

Steel	C	Si	Mn	Ni	Mo	Cr	Cu	Al	Nb	d_γ (μm)
BS1	0.10	0.31	1.42	0.02	<0.005	<0.02	<0.02	0.039	0.035	4.2
BS2	0.065	0.37	1.47	0.48	0.008	0.03	0.03	0.036	0.024	8.7
BS3	0.21	0.32	1.10	0.02	<0.005	<0.02	<0.02	0.028	<0.005	9.5

Table 9.2: Composition in wt.% of BS steels for which ferrite grain sizes and volume fractions were calculated [116].

9.1.2.2 Ferrite Volume Fraction Calculations

Data on the evolution of allotriomorphic ferrite fraction with time and temperature during cooling were obtained from British Steel and CENIM, Madrid [116, 117] for the steels in Table 9.2. The measurements were obtained by metallography on dilatometric specimens quenched out at different stages of the transformation. Volume fractions were determined at British Steel using standard lineal intercept techniques (five traverses each of 50 intercepts) and at CENIM by point counting at 500 × magnification on a 100 point grid. Comparisons with the computed allotriomorphic ferrite transformation kinetics at 1 and 10 °C s^{-1} are shown in Figure 9.9. It can be seen that the start temperature of the transformation was well predicted, with only a small under-estimation of about 10 °C. The

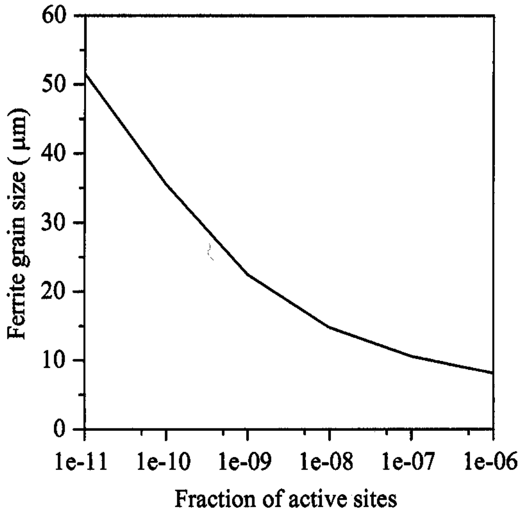

Figure 9.7: Calculated effect of the fraction of active nucleation sites, K_1^f, on allotriomorphic ferrite grain size in steel HO1 with $d_\gamma = 10$ μm, cooled at 0.1 °C s^{-1}.

shape of the calculated curves was an excellent fit with the measured progress of transformation, especially in steel BS2. The final fraction of ferrite was accurately predicted for BS1 and BS2, but slightly over-estimated by about 10% in BS3, the steel with the highest carbon content.

The volume fraction calculations for the BST steels will be discussed in a later section concerning the three phase simultaneous transformation model.

9.2 Allotriomorphic Ferrite and Pearlite

The pearlite model as described in Section 6.3 was the first to be combined with allotriomorphic ferrite within the framework of the simultaneous transformation kinetics theory. The predicted pearlite transformation kinetics were found to be quite rapid. This is due to two factors. Firstly, the pearlite is assumed not to require nucleation in the sense that each colony begins from a single grain of ferrite. Secondly, the pearlite grows at a constant rate since its overall composition is approximately equal to that of the austenite from which it grows. The variation of volume fraction with temperature in a 0.78 C wt.% steel continuously cooled at 1 °C s^{-1} calculated by the current pearlite transformation model is shown in Figure 9.10. Complete transformation to pearlite was correctly predicted for this eutectoid steel. The model has also been successfully validated for isothermal transformation against a series of TTT diagrams for near-eutectoid steels [120].

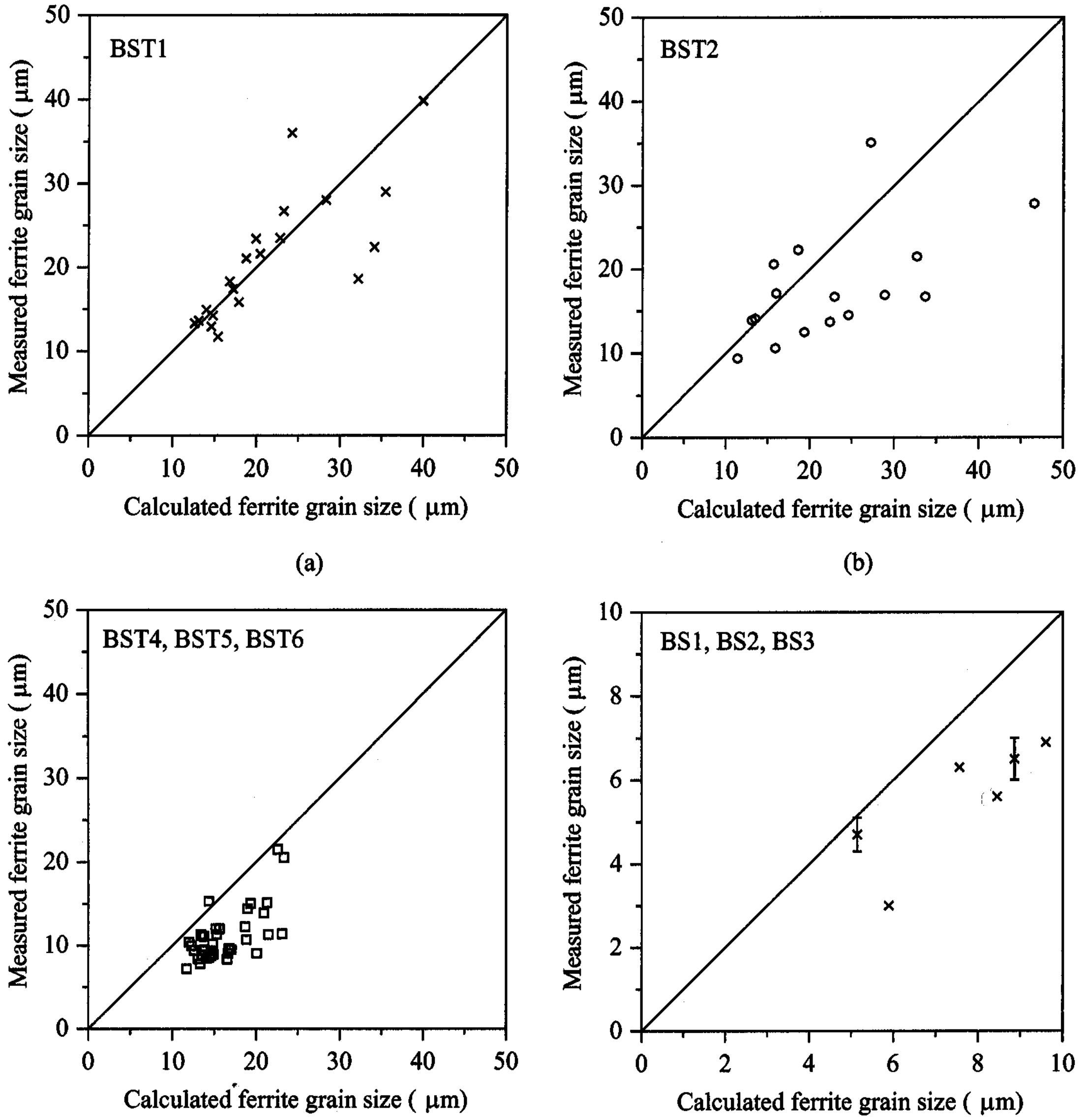

(a)

(b)

(c)

(d)

Figure 9.8: Comparison of measured and calculated ferrite grain sizes in steel (a) BST1, (b) BST2, (c) BST4, BST5 and BST6, and (d) BS1, BS2 and BS3 (error bars on BS1 data are 95% confidence limits).

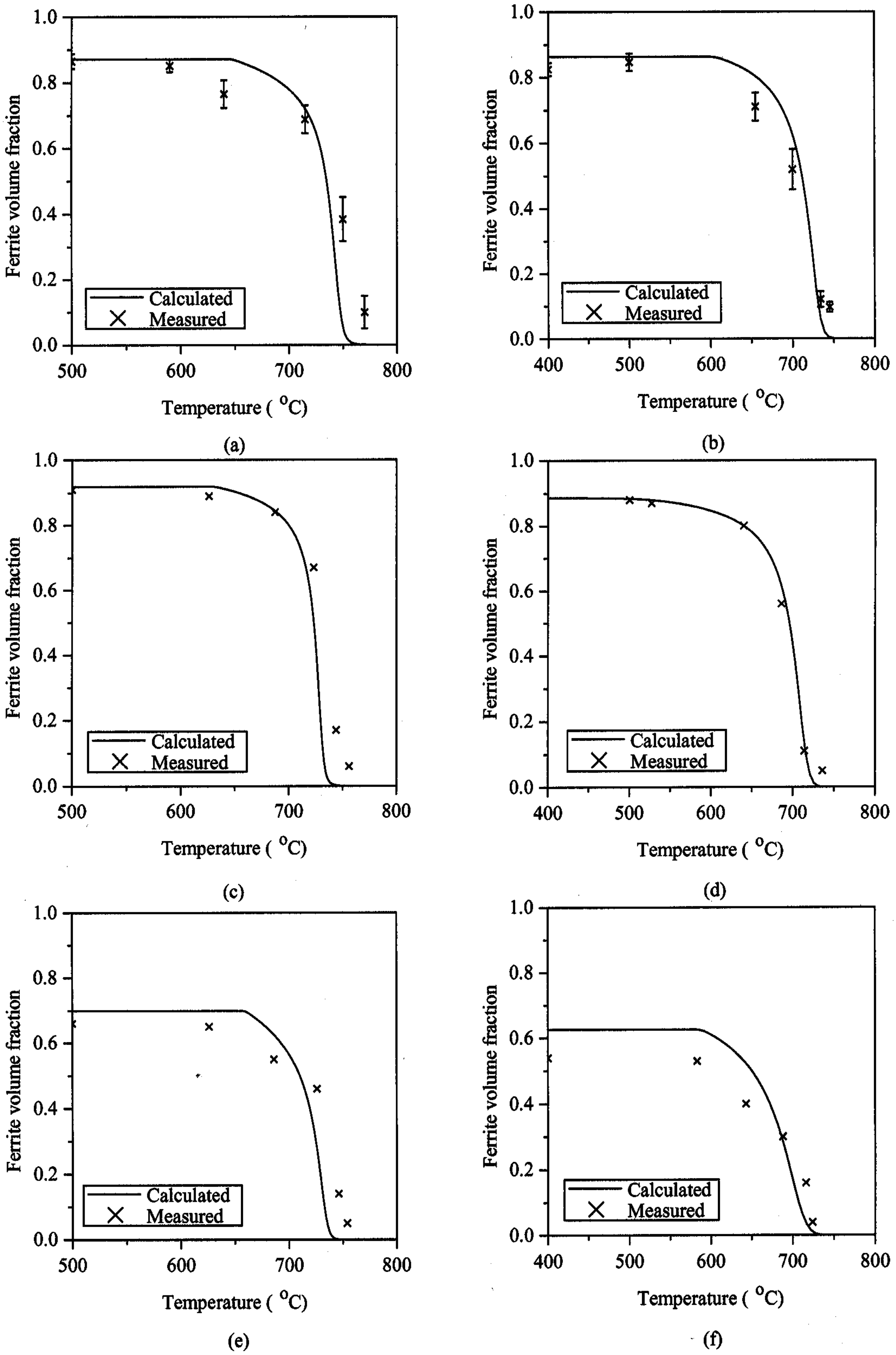

Figure 9.9: Comparison of calculated and measured allotriomorphic ferrite volume fractions during continuous cooling in steel (a) BS1 at 1 °C s^{-1}, (b) BS1 at 10 °C s^{-1} (error bars are 95% confidence limits), (c) BS2 at 1 °C s^{-1}, (d) BS2 at 10 °C s^{-1}, (e) BS3 at 1 °C s^{-1} and (f) BS3 at 10 °C s^{-1}.

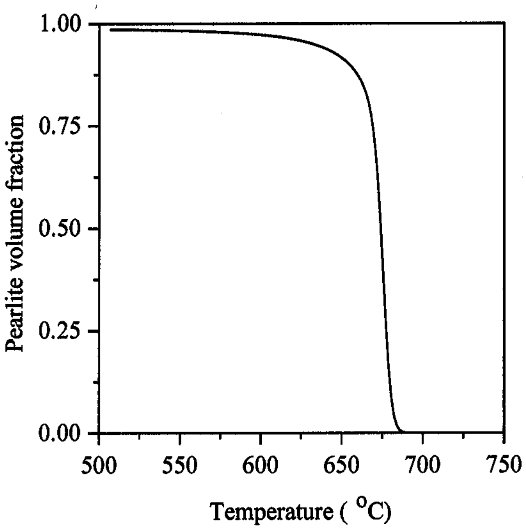

Figure 9.10: Calculated pearlite volume fraction as a function of temperature for a 0.78 C wt.% steel, austenite grain size 50 μm, cooled at a constant rate of 1 °C s^{-1}.

A specific experiment was commissioned from British Steel to investigate the rapid kinetics. Steel BS3 was isothermally transformed at 660 °C, below the experimentally determined pearlite-start temperature, using a dilatometer. A series of specimens were quenched out after different holding times and metallographically analysed using standard techniques to determine the volume fractions of allotriomorphic ferrite and pearlite present [126]. The austenite grain size was measured as 67 ± 6 μm. Figure 9.11 compares the calculated and measured volume fractions as a function of time. It can be seen that the shape of the allotriomorphic ferrite curve was accurately predicted, as were the final fractions of both phases, but the fraction of ferrite at each temperature was under-estimated throughout most of the transformation. The experimental pearlite transformation started much earlier and evolved more gradually than calculated. The experimental microstructures show that only bainite and/or martensite was formed during the quench from 660 °C, and that the pearlite appeared to have genuinely formed during the hold.

One possible explanation for the discrepancy is that because the calculated ferrite volume fraction is lower than the experimental value at each time, less carbon will have been calculated to partition into the residual austenite. The austenite carbon concentration will then take longer to reach the $x^{\gamma\theta}$ boundary composition required for the start of pearlite transformation. Figure 9.12a shows the same calculations but with the ferrite fraction artificially increased at each time by trebling the growth rate. The calculated fraction of ferrite at the experimental pearlite transformation start time is now very close to the measured value. The calculated pearlite-start time has decreased significantly from around 800 s in the original case to about 150 s, which is much closer to the experiment. The calculated carbon concentration of the austenite (black lines) and $x^{\gamma\theta}$ boundary (red lines) for three growth rates are plotted as a function of time in Figure 9.12b. The $x^{\gamma\theta}$ boundary concentration and thus the pearlite-start is reached much earlier with the trebled growth rate. This indicates that the under-estimation of the ferrite fraction and thus enrichment of the austenite is the reason that the model does not predict the correct pearlite-start time.

Further verification of the pearlite routine is considered in the next section concerning the three phase model.

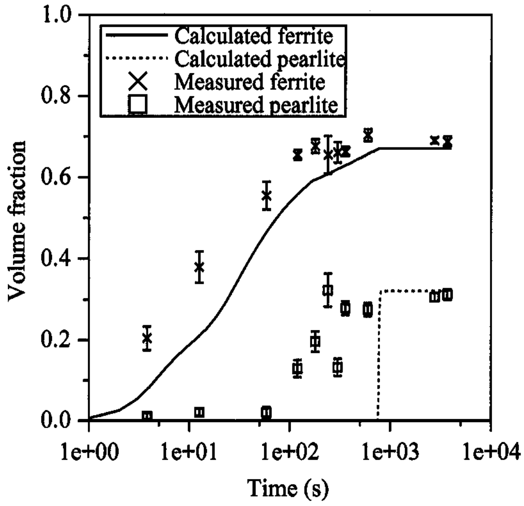

Figure 9.11: Comparison of calculated and measured ferrite and pearlite volume fractions for isothermal transformation of steel BS3 (0.21 C 0.32 Si 1.10 Mn wt.%) at 660 °C, austenite grain size 67 μm. Error bars are 95% confidence limits.

9.3 Three Phase Model

The individual model for Widmanstätten ferrite was combined with the allotriomorphic ferrite and pearlite model using the overall simultaneous transformation kinetics theory for heterogeneous nucleation at austenite grain boundaries. Firstly, the general effects of changing steel composition, austenite grain size and cooling rate were investigated, to ensure that the model replicated basic metallurgical trends. It was then validated against sets of experimental data published recently in the literature or specifically generated

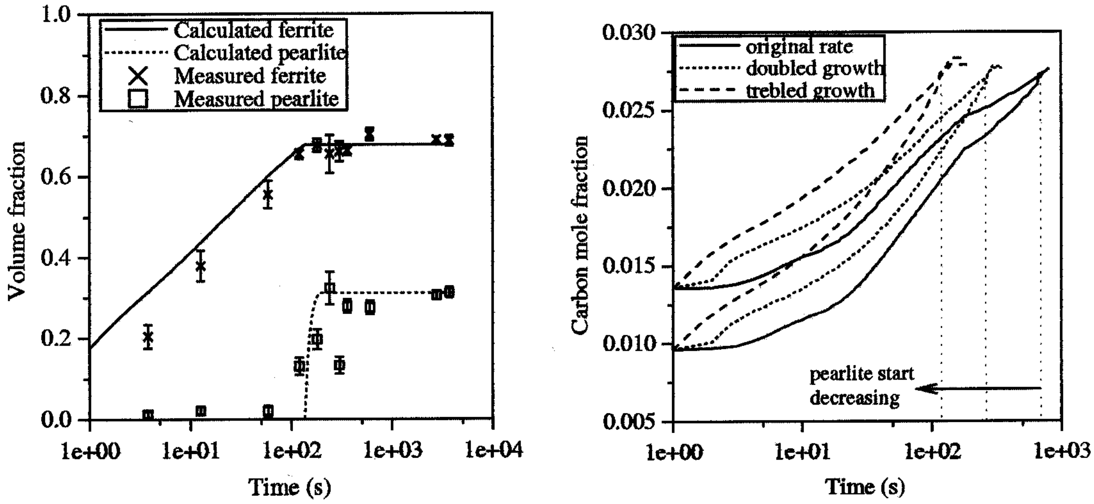

(a)

(b)

Figure 9.12: (a) Ferrite and pearlite volume fractions for isothermal transformation of steel BS3 as in Figure 9.11 but with a trebled parabolic rate constant, showing that an increase in calculated ferrite fraction reduces the pearlite-start time. (b) Calculated carbon concentration of enriched austenite (black) and $x^{\gamma\theta}$ boundary (red) for increasing ferrite parabolic growth rate constants (and thus volume fraction). The intersection of the lines for each rate constant defines the pearlite-start time.

for testing the model. The allotriomorphic ferrite nucleation rate parameters were then reassessed and optimum values chosen for all the data analysed.

9.3.1 Basic Trends

The effect of changing the carbon content of the steel was investigated, by starting with a 0.1 C, 0.5 Si, 0.5 Mn wt.% steel and gradually increasing the carbon up to 0.7 wt.%. The austenite grain size and cooling rate were kept fixed at 50 μm and 1 °C s^{-1}, respectively. The results are shown in Figure 9.13 and several points can be noted. As expected, the allotriomorphic ferrite start temperature was suppressed as carbon content increased, from approximately 800 °C at 0.1 wt.% C down to about 710 °C at 0.5 wt.% C. The Widmanstätten ferrite transformation start was similarly retarded, from 730 to 675 °C. The volume fraction of allotriomorphic ferrite decreased from around 0.6 to zero as carbon increased, and Widmanstätten ferrite from 0.25 to zero, whereas the pearlite fraction increased from 0.15 at 0.1 wt.% C up to almost 1 as the steel approached the eutectoid composition.

The decrease in ferrite transformation kinetics with increasing carbon content is caused by the reduction in the driving force for the austenite to ferrite transformation and the retardation of ferrite growth, which is assumed to be controlled by the diffusion of carbon in the austenite ahead of the α/γ interface. The main effect of increasing the Mn content in a base 0.2 C 0.01 Si 0.01 Mn wt.% steel, Figure 9.14, was to retard the ferrite transformation start, from 800 to 725 °C for allotriomorphic ferrite and 710 down to 670 °C for Widmanstätten ferrite. Manganese is an austenite stabilising element and thus reduces the driving force for ferrite formation. The pearlite-start temperature also decreased from 650 to 600 °C. The Widmanstätten ferrite fraction increased slightly with Mn content. The allotriomorphic ferrite fraction decreased from approximately 0.6 to 0.5 and was balanced by an increase in pearlite from 0.3 to 0.4. These trends are consistent with the well-established effects of C and Mn on transformation kinetics, as illustrated, for instance, in TTT diagram compendia [51], although such diagrams do not contain detailed information about the fraction of Widmanstätten ferrite.

9.3.2 Published Experimental Data

9.3.2.1 British Steel data

A report published by British Steel [115] provided detailed metallographic data for a series of C-Mn steels, each cooled in a furnace, air or vermiculite from four different austenitising temperatures. Five of these steels were selected to test the model (Table

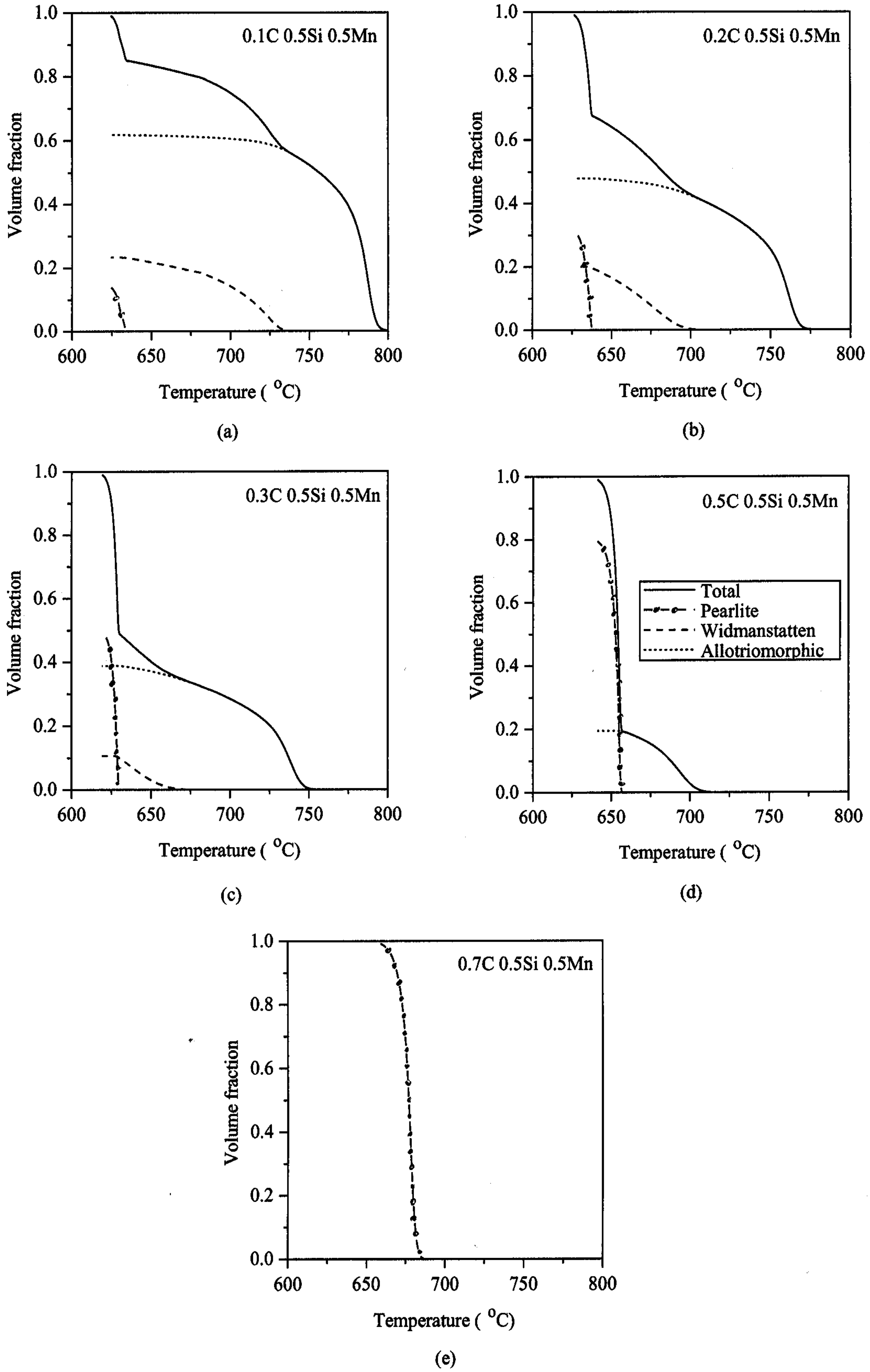

Figure 9.13: Calculated effect of carbon on a 0.5 Si 0.5 Mn wt.% steel, austenite grain size 50 μm, cooled at 1 °C s^{-1}, with (a) 0.1 C, (b) 0.2 C, (c) 0.3 C, (d) 0.5 C and (e) 0.7 C wt.%.

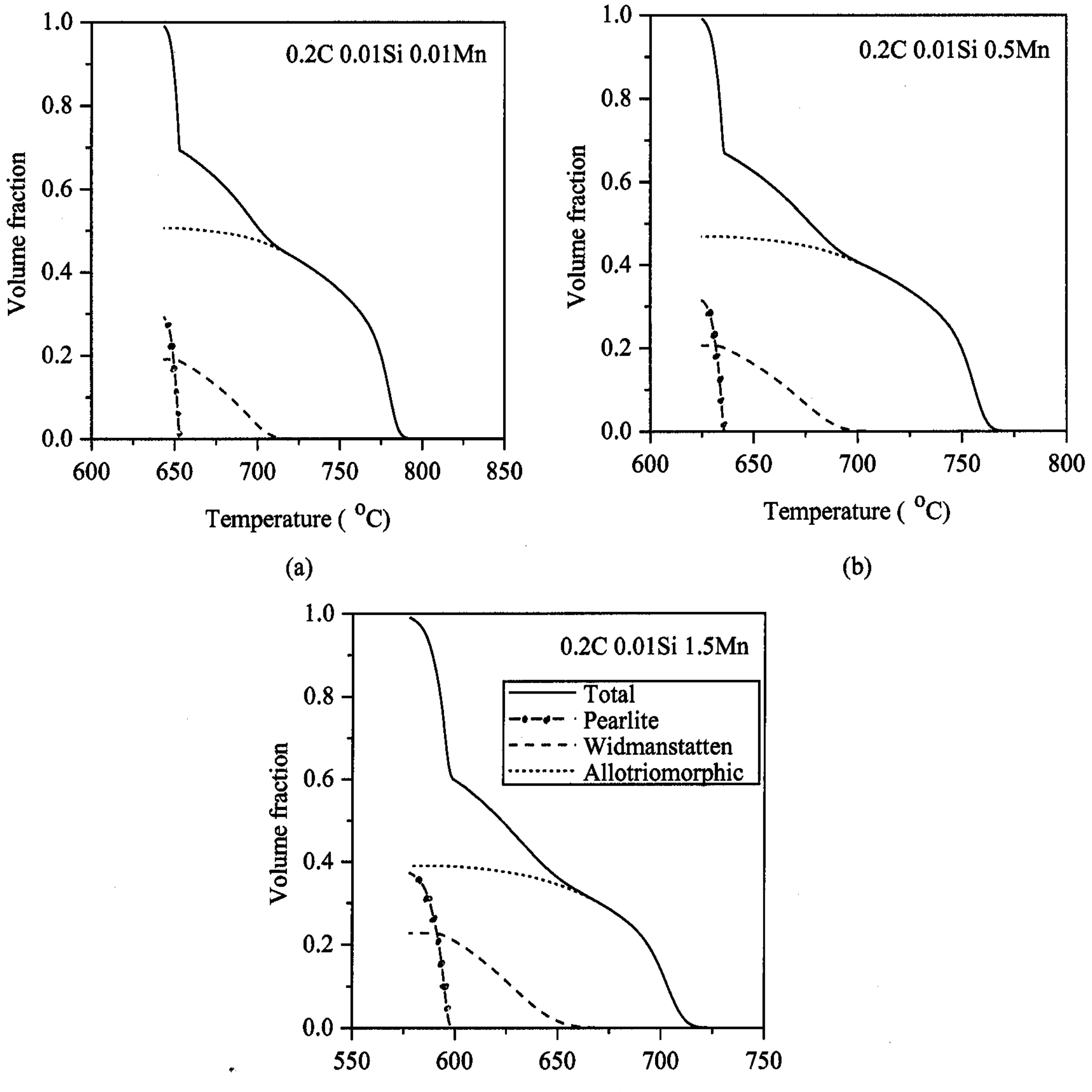

(a)

(b)

(c)

Figure 9.14: Calculated effect of manganese on a 0.2 C 0.01 Si wt.% steel, austenite grain size 50 μm, cooled at 1 °C s^{-1}, with (a) 0.01 Mn, (b) 0.5 Mn and (c) 1.5 Mn wt.%.

9.1), with compositions ranging from 0.1 to 0.3 wt.% C with 0.8 or 1.35 wt.% Mn. In the tabulated experimental results, no distinction was made between allotriomorphic ferrite and Widmanstätten ferrite with just a single "ferrite" volume fraction value quoted (this is also apparent from the micrographs in the report). The data are suitable for testing whether the balance between the total ferrite (= allotriomorphic ferrite + Widmanstätten ferrite) and pearlite is correct in the model. The volume fractions and grain sizes in the report were determined using the lineal intercept method. Austenite grain sizes were quantified from 200 grain boundary intersections along a series of diametrical traverses. Phase fractions and ferrite grain sizes were assessed at 400 to 600 × magnification on a travelling-stage microscope, using two runs each of 15 mm length per sample. No assessment of the errors in the measurements was reported.

The pearlitic fraction of the microstructure varied between less than 0.1 in BST1 to more than 0.8 in BST6. The calculated volume fractions of ferrite and pearlite are compared with the measured results in Figures 9.15 and 9.16, respectively. The large fractions of ferrite in BST1, BST2 and BST4 were well-predicted. However, two erroneous data points were observed in both the BST2 and BST4 data, where the calculated ferrite fraction was several times larger than the measured value. This is because the model predicted large quantities of Widmanstätten ferrite whereas the experimental samples were claimed to contain large amounts of upper bainite. Analysis of some of the micrographs from this report indicated that Widmanstätten ferrite was possibly misinterpreted as bainite, in which case, better agreement is obtained with the calculations. Alternatively, the calculated results are incorrect because the model does not allow for bainite.

The results for BST5 and BST6 were less sensitive to the austenite grain size and/or cooling rate than observed experimentally. Although the relative proportions of allotriomorphic and Widmanstätten ferrite varied, the total ferrite fraction remained approximately constant for each steel. Naturally, this was also the case for pearlite, which forms from the residual austenite. For the same reason, steels BST1, BST2 and BST4 show good agreement for pearlite.

9.3.2.2 Bodnar and Hansen Data

Two published papers by Bodnar and Hansen [127, 128] provided a good source of measured transformation data on allotriomorphic ferrite, Widmanstätten ferrite and pearlite. The data cover three steels with a range of austenite grain sizes and cooling rates. The phase fractions, the ferrite grain size and the Ar_3 temperatures were determined in each case. The volume fractions were determined by point counting with a 100-point grid; the grain sizes using the ASTM standard circular intercept method [112]. However, 95% con-

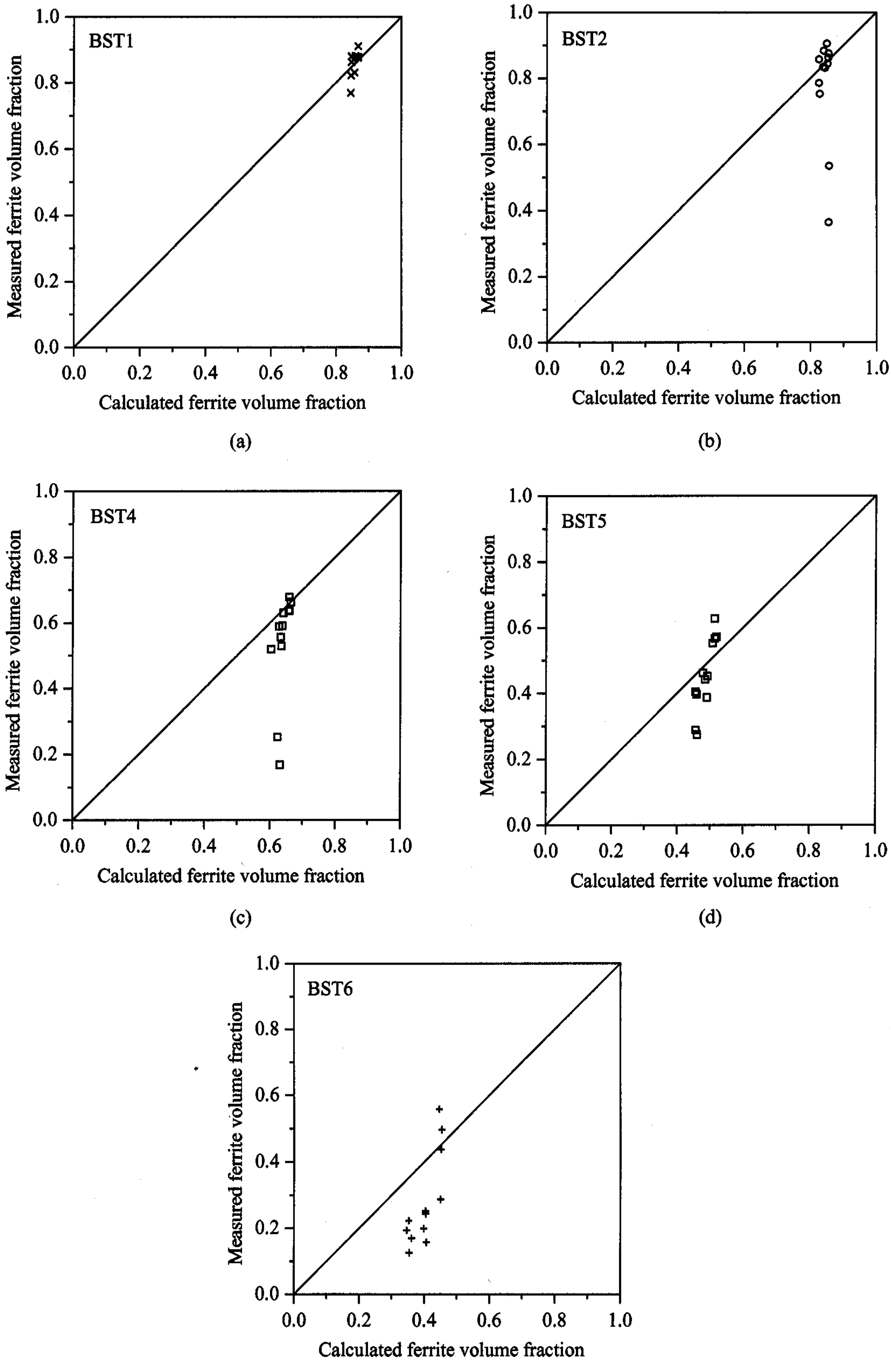

(a) (b) (c) (d) (e)

Figure 9.15: Comparison of measured and calculated ferrite (allotriomorphic + Widmanstätten) volume fractions in steels (a) BST1, (b) BST2, (c) BST4, (d) BST5 and (e) BST6.

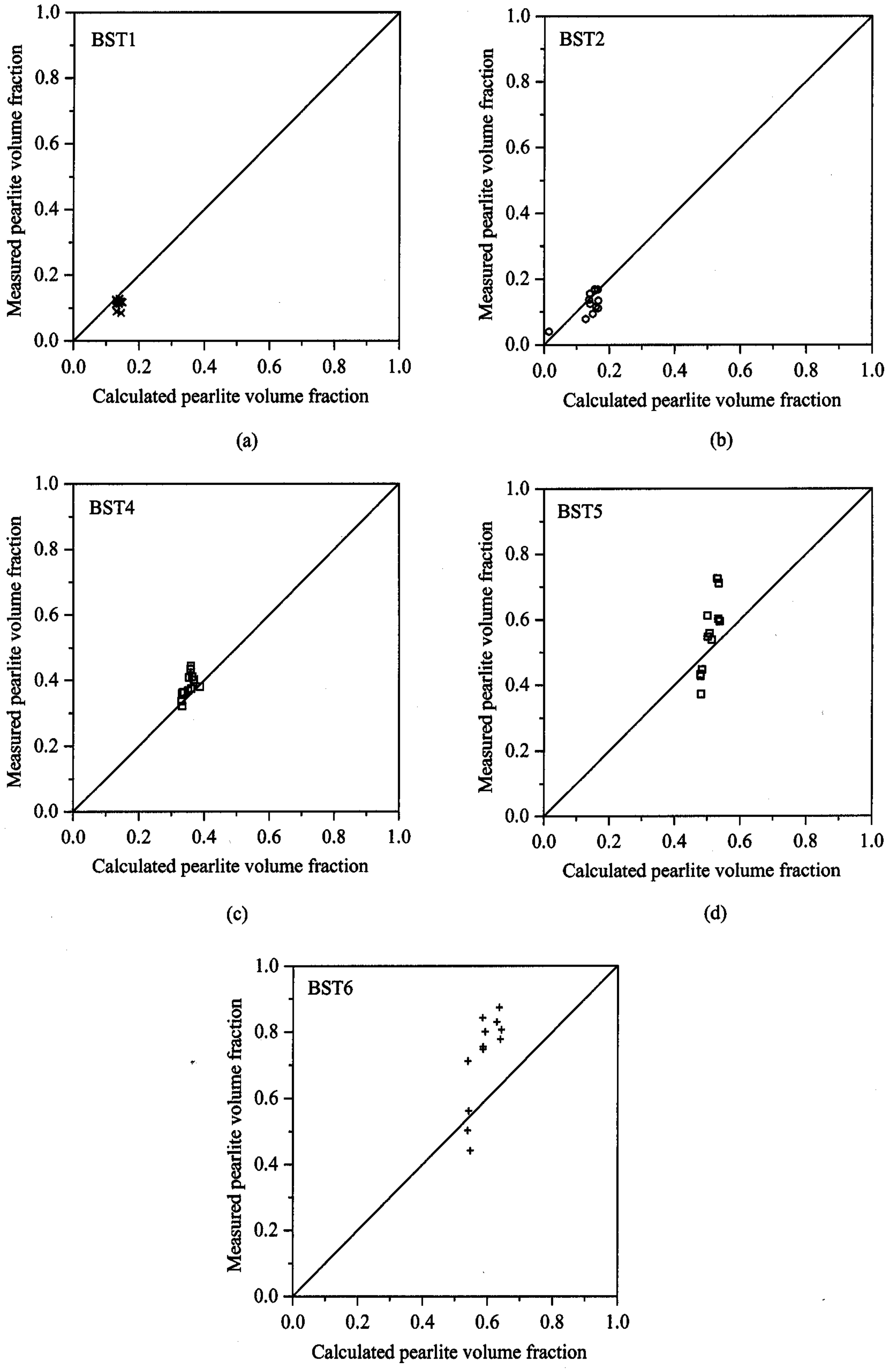

(a)

(b)

(c)

(d)

(e)

Figure 9.16: Comparison of measured and calculated pearlite volume fractions in steels (a) BST1, (b) BST2, (c) BST4, (d) BST5 and (e) BST6.

fidence limits were only cited for two of the austenite grain sizes and these were used to determine the error bars for the C-Mn steel calculations. The compositions and austenite grain sizes of the steels are given in Table 9.3.

Figure 9.17 shows the calculated effect of a change in cooling rate on the C-Mn-Si steel with a 55 μm austenite grain size. An increase in the cooling rate leads to an increase in Widmanstätten ferrite at the expense of allotriomorphic ferrite. The quantity of pearlite increased very slightly. As expected, the ferrite and pearlite start temperatures decreased as the cooling rate increased.

The results for the same steel cooled at 0.98 °C s^{-1} from three different austenite grain sizes are shown in Figure 9.18. Over half of the microstructure consisted of allotriomorphic ferrite at the smallest grain size of 30 μm, but at larger sizes Widmanstätten ferrite became dominant. The fraction of pearlite remained virtually constant. The allotriomorphic ferrite and pearlite transformation start temperatures were virtually unchanged by the variation in grain size but the Widmanstätten ferrite start temperature, W_s, increased with austenite grain size.

The calculated fractions of each phase for all the combinations of composition, grain size and cooling rate are compared with the measured values in Figure 9.19. In steels where the fraction of allotriomorphic ferrite was under-estimated, the Widmanstätten ferrite fraction was over-estimated, and *vice versa.* Figure 9.20 compares the results for allotriomorphic and Widmanstätten ferrite as a function of cooling rate in the C-Mn-Si steel. When $d_\gamma = 30$ μm, the amount of allotriomorphic ferrite is underestimated leading to an exaggerated quantity of Widmanstätten ferrite. By contrast, for $d_\gamma = 100$ μm, the opposite tendency is observed. The sharp transition in the experimental microstructure from mainly allotriomorphic to Widmanstätten ferrite with increasing cooling rate when $d_\gamma = 55$ μm could not be reproduced by the model. The calculated and measured allotriomorphic ferrite grain sizes are in good agreement as shown in Figure 9.21. The grain size is determined during the early stages of transformation, indicating that the calculations have captured these stages rather well.

Steel	C	Si	Mn	Cu	Al	d_γ (μm)
C-Mn-Si	0.18	0.18	1.15	0.09	0.026	30, 55, 100
C-Mn-V	0.19	0.03	1.11	0.11	<0.005	31, 54, 102
C-Mn	0.19	0.079	0.72	0.078	<0.005	59±10, 204±18

Table 9.3: Composition in wt.% and austenite grain size in microns of Bodnar and Hansen steels [127, 128].

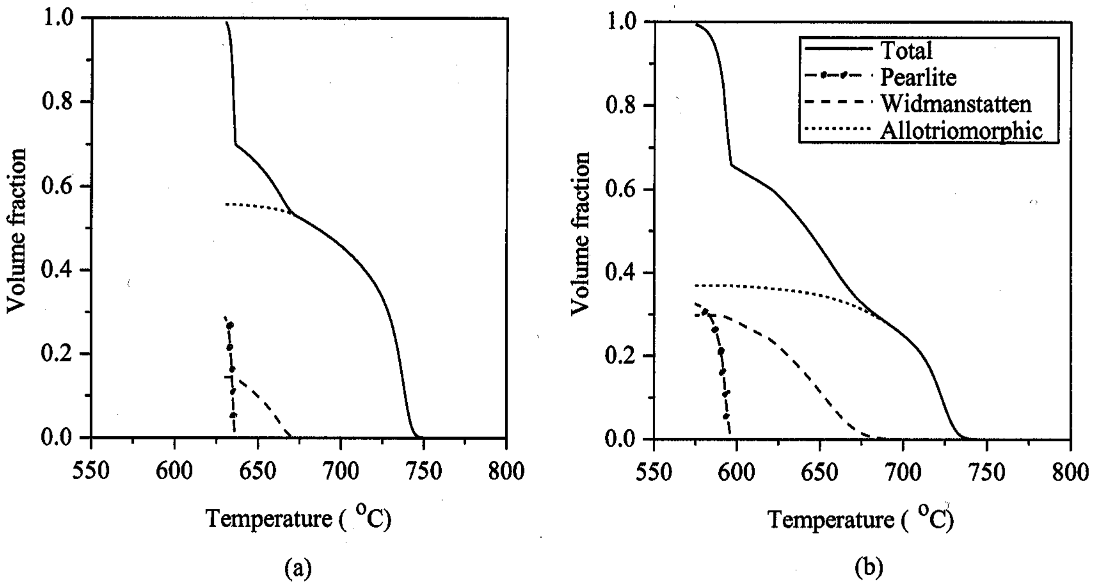

Figure 9.17: Calculated effect of cooling rate on transformation in C-Mn-Si steel with 55 μm austenite grain size, at (a) 0.267 °C s^{-1} (16 °C min^{-1}), (b) 1.65 °C s^{-1} (99 °C min^{-1}).

9.3.3 Thermecmastor Data

The thermomechanical simulation experiments on the 0.21 wt.% carbon steel reported in Chapter 8 are modelled as shown in Figure 9.22. There is evidence in the microstructures that in some cases pearlite continued to form during cooling in specimens after quenching which was intended to stop the transformation. The evolution of pearlite therefore cannot be compared with the calculations.

The calculations do not accurately reproduce the experimental microstructures. The allotriomorphic ferrite volume fraction, V_α, is generally under-estimated at slow cooling rates and small austenite grain sizes (Figures 9.22a, b and c), leading to an over-estimation of Widmanstätten ferrite. The results for 5 °C s^{-1} cooling and the large austenite grain size (1200 °C) (Figures 9.22d and e) are much better.

The allotriomorphic ferrite start temperature is, however, accurately predicted in Figures 9.22a, b and c, but W_s is under-estimated. By contrast, in Figures 9.22d and e, W_s is correct but the F_s is over-estimated. Figure 9.23a compares the measured and calculated room temperature fractions for all phases. Finally, Figure 9.23b shows that in spite of the difficulties in predicting V_α, the calculated grain sizes are very similar to the measured values. (The fraction of allotriomorphic ferrite in the 1200 °C sample was too small to enable a grain size to be measured properly). This suggests that the nucleation kinetics

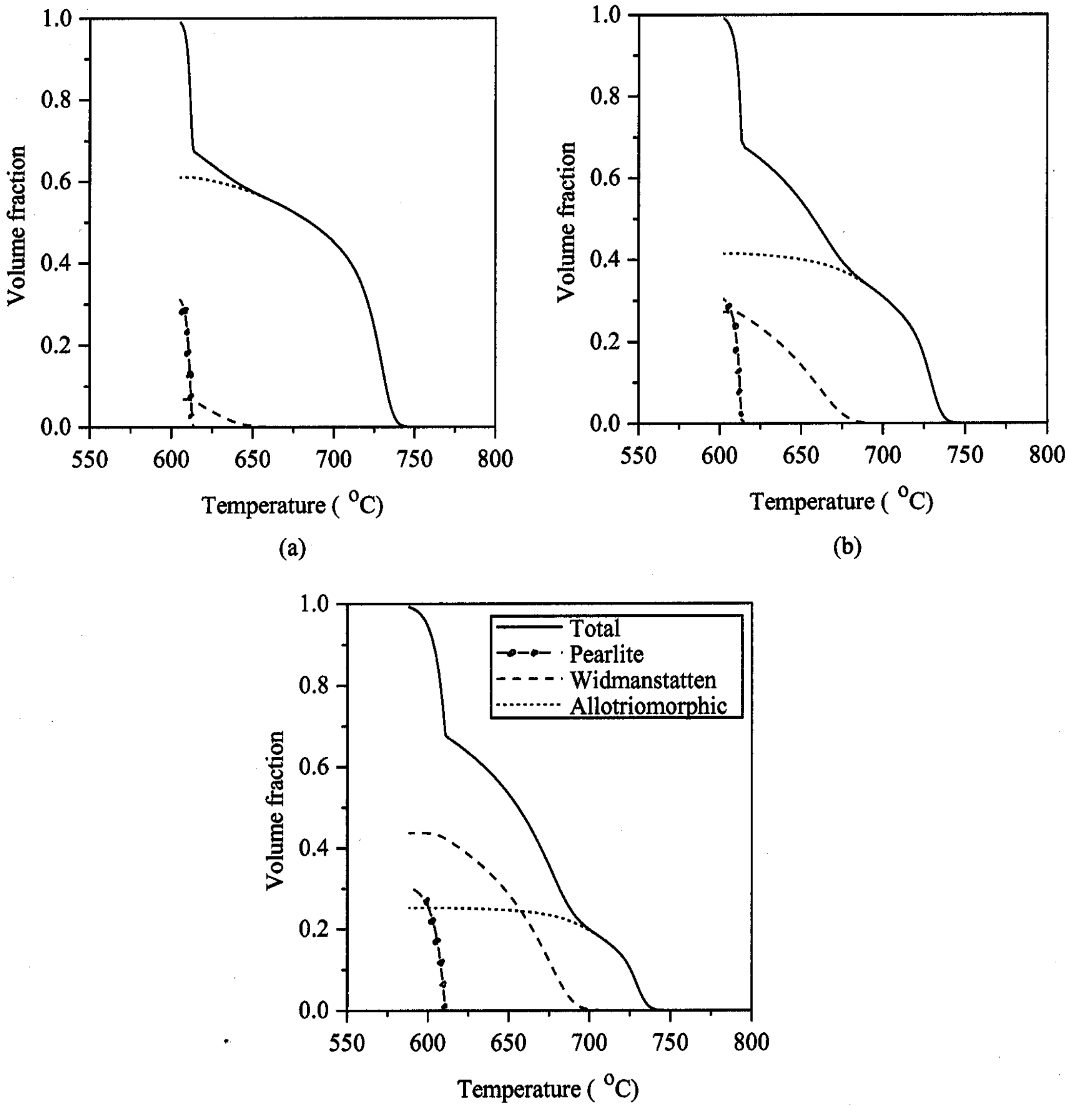

(a)

(b)

(c)

Figure 9.18: Calculated effect of austenite grain size on transformation in C-Mn-Si steel cooled at 0.98 °C s^{-1} (59 °C min^{-1}) , (a) 30 μm, (b) 55 μm and (c) 100 μm.

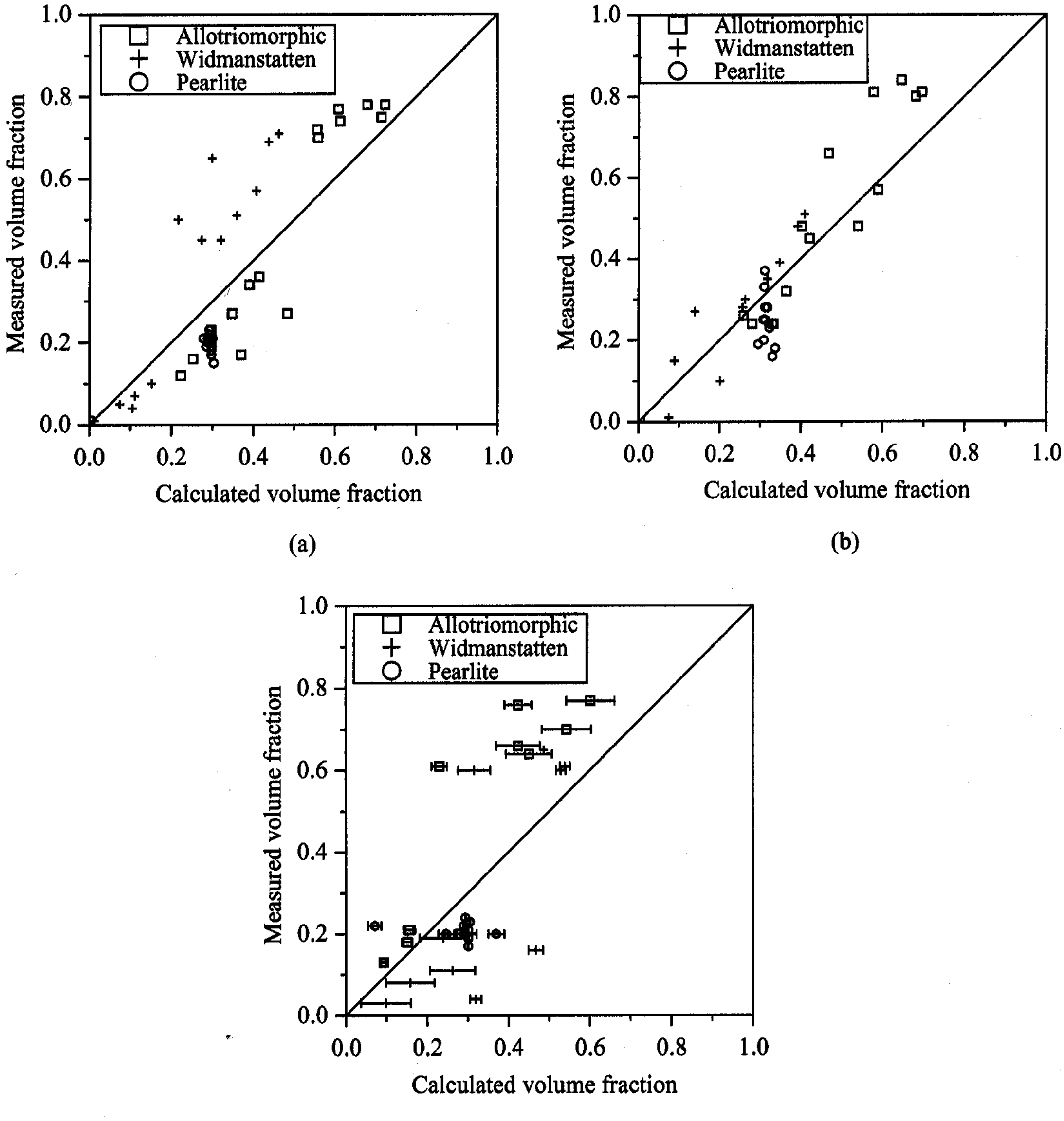

(a)

(b)

(c)

Figure 9.19: Comparison between calculated and measured volume fraction results for (a) C-Mn-Si steel, (b) C-Mn-V steel, (c) C-Mn steel (error bars are 95% confidence limits).

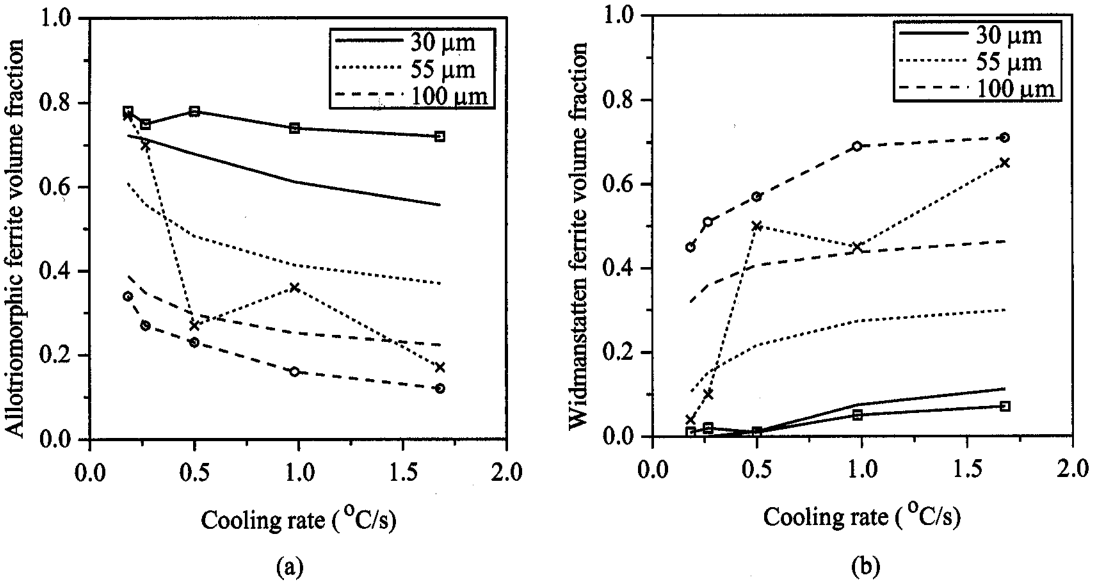

Figure 9.20: Comparison between measured (lines with symbols) and calculated (no symbols) volume fraction in a C-Mn-Si steel as a function of cooling rate, (a) allotriomorphic ferrite, (b) Widmanstätten ferrite.

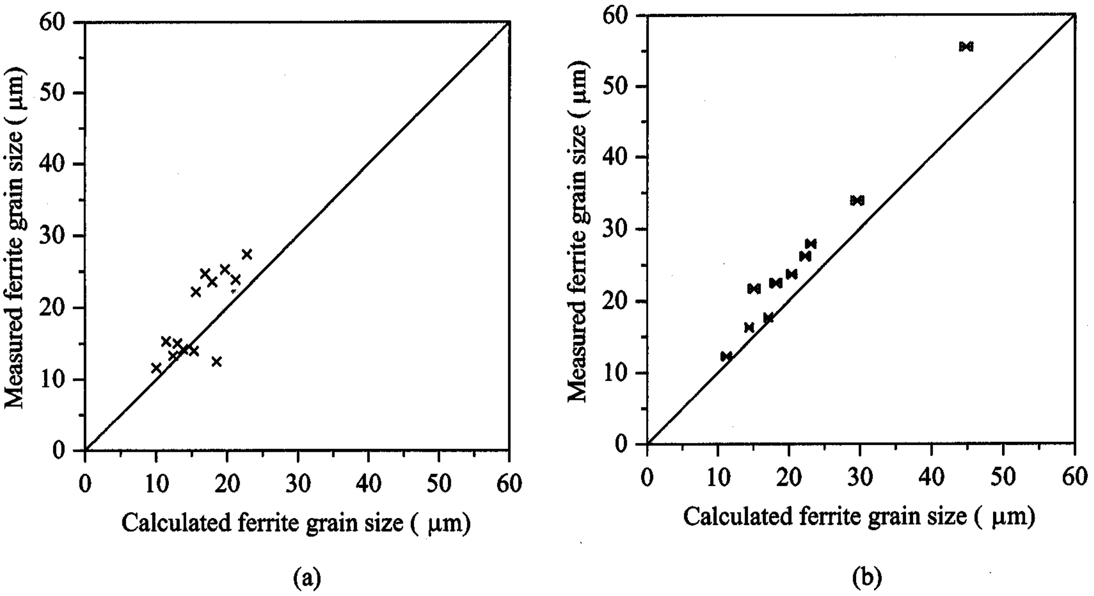

Figure 9.21: Comparison between calculated and measured ferrite grain sizes for (a) C-Mn-Si steel, (b) C-Mn steel.

in the model are satisfactory and the austenite grain boundaries are saturating at the correct point in the transformation. It is the subsequent growth of the ferrite into the grain interior that could be causing the problem.

9.3.4 Discussion

The grain size of allotriomorphic ferrite and the transformation-start temperatures can be reproduced by a careful selection of the relative potencies of grain face, edge and corner nucleation sites. At slow cooling rates and small austenite grain sizes, where the undercoolings are small, corner and edge sites dominate [129, 130] in spite of their lower number densities relative to the high activation energy face sites. Larger grain sizes increase the proportion of face sites and faster cooling rates provide sufficient undercooling and thus driving force for face sites to predominate.

The final microstructures and ferrite grain sizes predicted were generally very good for low-carbon, low-alloy steels with small austenite grain sizes. At higher carbon concentrations (0.3 wt.%), the allotriomorphic ferrite grain size and fraction tended to be over-estimated at the expense of pearlite.

Qualitative changes in the allotriomorphic and Widmanstätten ferrite fractions are correctly predicted as a function of cooling rate and austenite grain size but variations were found to be smaller than expected experimentally. Both the Bodnar and Hansen data and the Thermecmastor results show that the balance between allotriomorphic ferrite and Widmanstätten ferrite at intermediate austenite grain sizes is incorrect. The allotriomorphic ferrite does not grow sufficiently rapidly to establish itself before Widmanstätten ferrite is initiated. This latter phase grows rapidly and tends to take over the transformation. The problem does not arise in very small grains, where allotriomorphic ferrite predominates, or in very large grains where Widmanstätten ferrite is the main phase.

The formation of intragranular allotriomorphic ferrite nuclei is one possibility not accounted for by the model, but there is little evidence for this in the steels studied. A further possibility is that the nucleation of Widmanstätten ferrite at different kinds of sites needs to be considered.

A recurring feature of the calculations is that the pearlite volume fraction does not vary significantly with either austenite grain size or cooling rate, in contrast to the experimental results. The amount of pearlite is largely dependent on the total fraction of ferrite formed and thus the enrichment of the austenite with carbon. This implies that the total ferrite fraction is also more or less constant with the initial composition, regardless of the effects of cooling rate or grain size apparent from the experiments (see Figures 9.15 and 9.16).

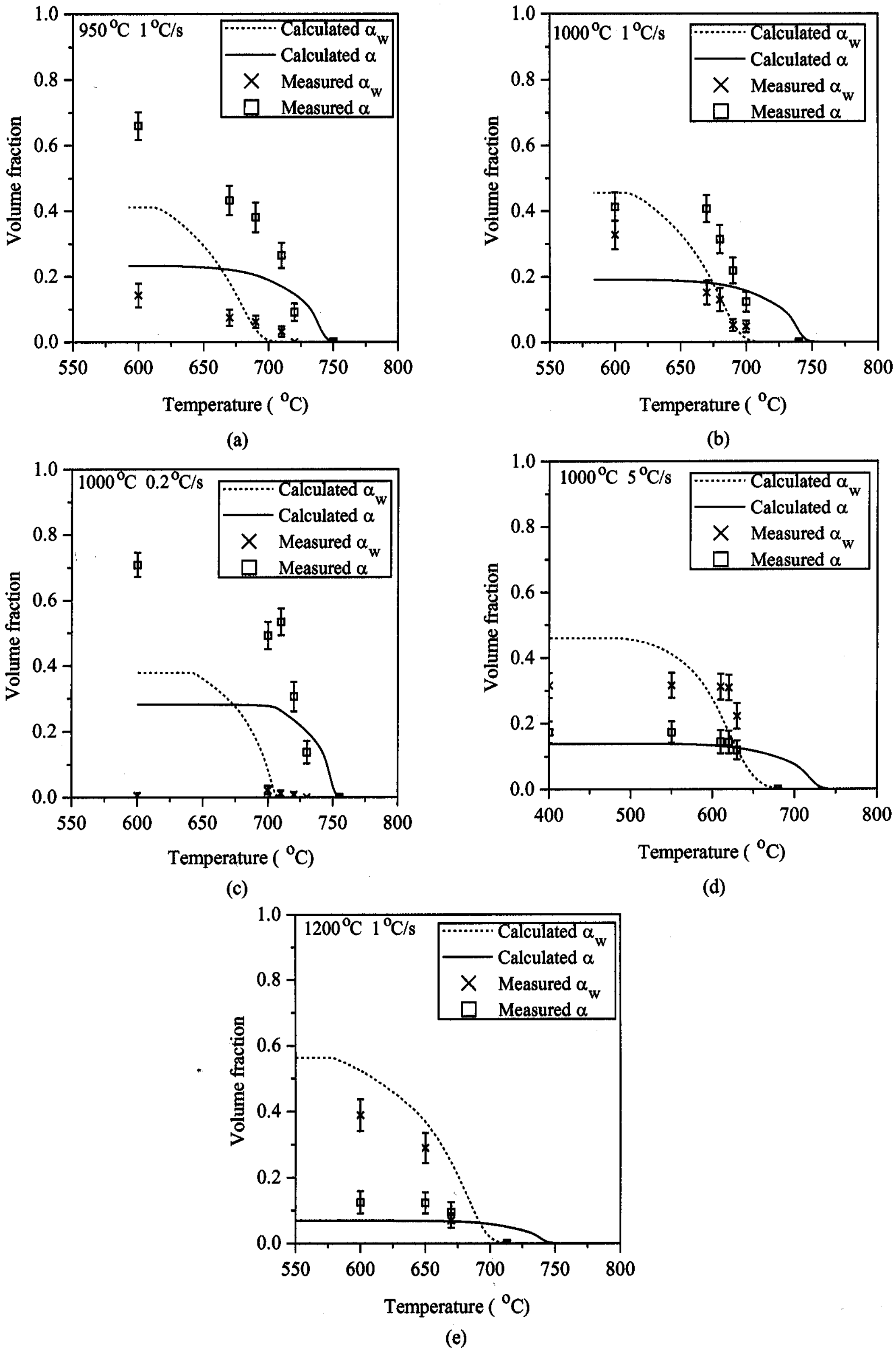

Figure 9.22: Comparison between measured and calculated transformation kinetics for a 0.21 wt.% C steel (Thermecmastor data), with austenitising temperatures and cooling rates of (a) 950 °C, 1 °C s^{-1}, (b) 1000 °C, 1 °C s^{-1}, (c) 1000 °C, 0.2 °C s^{-1}, (d) 1000 °C, 5 °C s^{-1}, (e) 1200 °C, 1 °C s^{-1}. Error bars are 95% confidence limits.

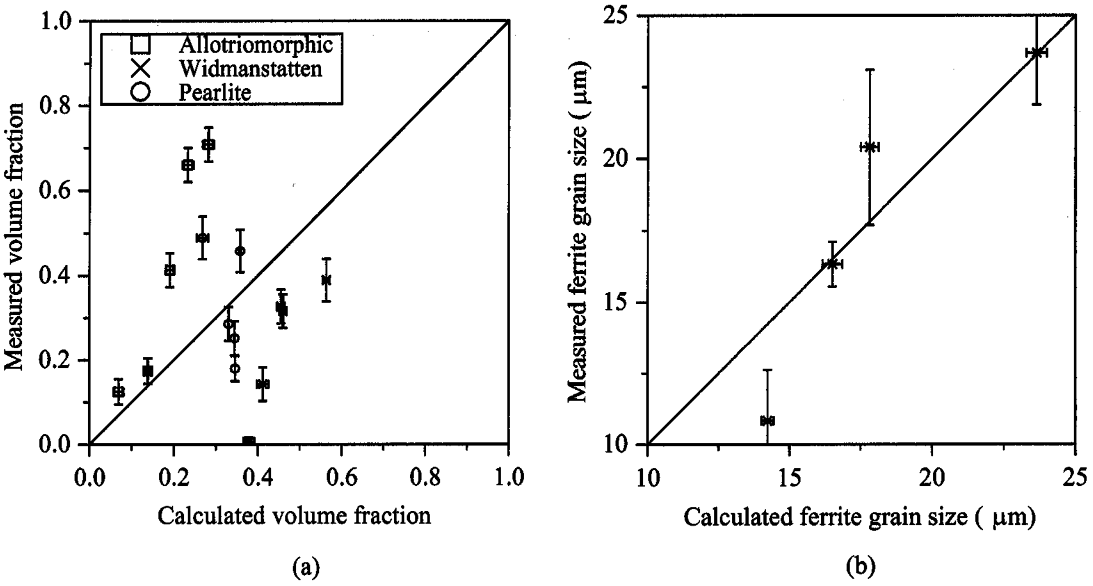

Figure 9.23: Comparison between measured and calculated results for a 0.21 wt.% C steel, (a) room temperature volume fractions of allotriomorphic ferrite, Widmanstätten ferrite and pearlite, (b) final allotriomorphic ferrite grain sizes. Error bars are 95% confidence limits.

The values of the site and shape factors were reassessed in light of the results from the individual and three phase models. The shape factors were reduced from their original values to increase the transformation rate of allotriomorphic ferrite, as this was identified as the major discrepancy between the calculations and experiment. This raises the ferrite-start temperature, refines the ferrite grain size and increases the proportion of allotriomorphic ferrite relative to Widmanstätten ferrite.

The final values selected and applied to all the calculations were:

$$\begin{aligned} K_1^f &= 1 \times 10^{-9} \\ K_2^f &= 0.1 \\ K_2^e &= 0.01 \\ K_2^c &= 0.001 \end{aligned}$$

9.4 Bainite Model

The random nucleation and boundary nucleation bainite models described in Section 7.3.4 were tested against experimental data reported in the literature on the isothermal transformation behaviour of three bainitic steels [79]. The compositions and austenite grain sizes are listed in Table 9.4. The random nucleation assumption was used first. Figure 9.24 illustrates the results for isothermal transformation of the Fe-Ni-Si-C steel at four different temperatures below the bainite-start temperature, B_s. It can be seen that the results assuming that the reaction stops when the carbon concentration of the austenite is given by the T_0 line are less accurate than when the T_0' line is used. Similar results for the Fe-Mn-Si-C and 300M steels are presented in Figures 9.25 and 9.26. The calculated and measured final volume fractions of bainite for all three steels isothermally transformed at temperatures ranging from 350 to 455 °C are compared in Figure 9.27, confirming the good predictions of the model when bainite transformation ceases at the T_0' composition. This is consistent with the published value of the stored energy of bainite as 400 J mol^{-1}.

Steel	C	Si	Mn	Ni	Mo	Cr	V	d_γ (μm)	Ref.
Fe-Mn-Si-C	0.22	2.03	3.00	0.00	0.00	0.00	0.00	47±5	[79]
Fe-Ni-Si-C	0.39	2.05	0.00	4.08	0.00	0.00	0.00	52±6	[79]
300M	0.44	1.74	0.67	1.85	0.83	0.39	0.09	86±9	[79]

Table 9.4: Composition in wt.% and mean lineal intercept austenite grain size of experimental steels used to test the bainite model.

The same calculations were repeated with the boundary transformation model, using only the T_0' line. The results for the Fe-Mn-Si-C and Fe-Ni-Si-C steels are compared with the random nucleation results and the measured data in Figures 9.28 and 9.29. The boundary model produced a better fit to the measured data in all cases, particularly in the shape of the transformation curve and the final bainite volume fraction. Thus, the boundary model was considered to be the better of the two and was combined with the three phase simultaneous transformation kinetics model.

During continuous cooling calculations, it was found to be difficult to obtain substantial amounts of bainite in any of the steels tested. Either allotriomorphic ferrite and/or Widmanstätten ferrite formed first, thus enriching the austenite too much for bainite formation, or at faster cooling rates, when bainite did start to form, it did so too slowly to achieve the required fraction. Little transformation occurred below the B_s until the M_s was reached, at which point the remaining austenite transformed to martensite. In the low-alloy steels of particular interest in this work, bainite is an important constituent. It is often observed experimentally at intermediate cooling rates, which are too fast for allotriomorphic ferrite but too slow for transformation directly to martensite.

If only bainite is permitted to form during the calculation (by setting the nucleation and growth rates of the other phases to zero), then substantial fractions can be achieved at slow cooling rates, Figure 9.30. Thus the model is capable of calculating large quantities

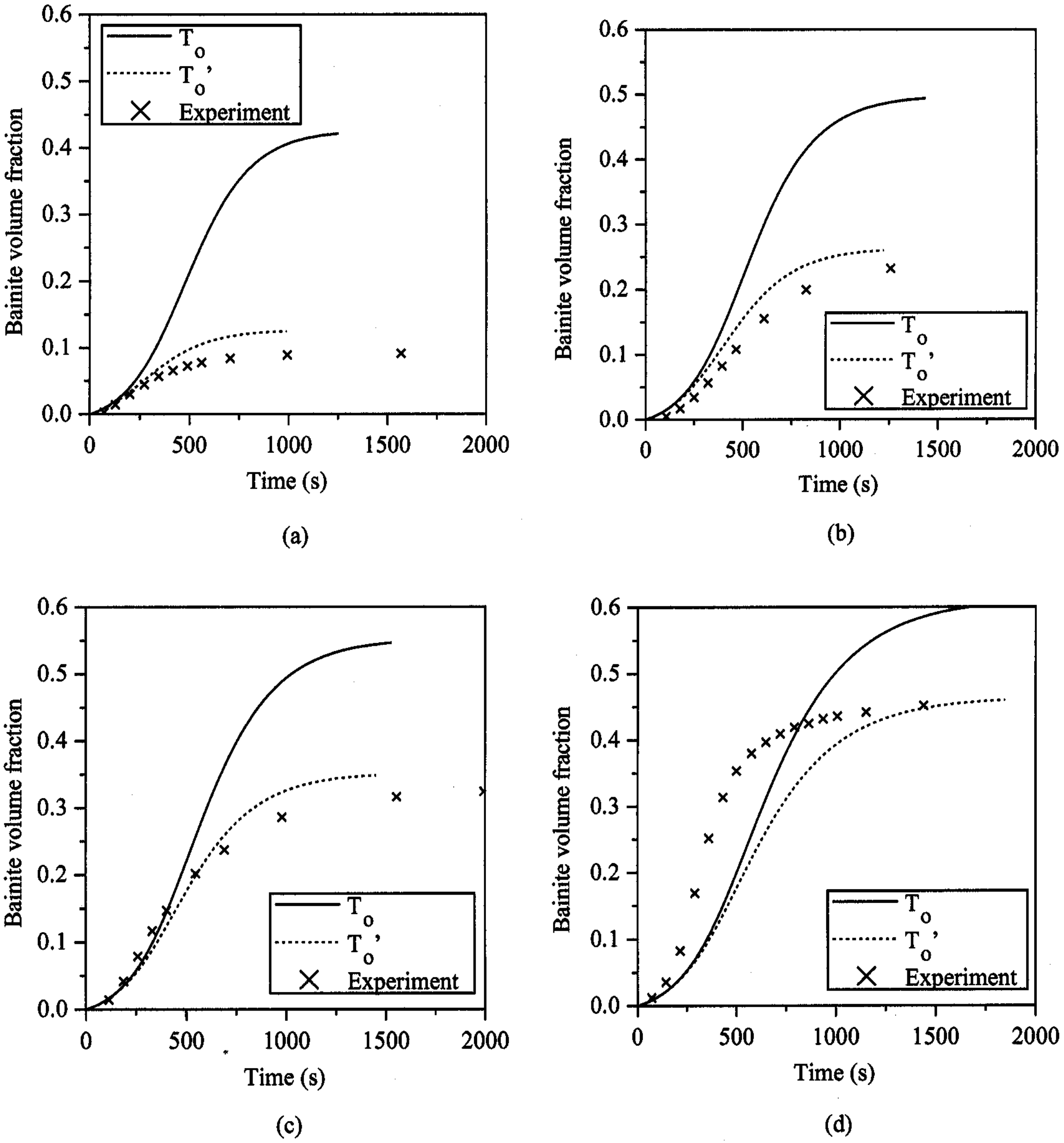

Figure 9.24: Comparison between calculated and measured bainite transformation kinetics for the Fe-Ni-Si-C steel, using the T_o and T_o' lines in the random nucleation model, at (a) 455 °C, (b) 421 °C, (c) 391 °C and (d) 350 °C.

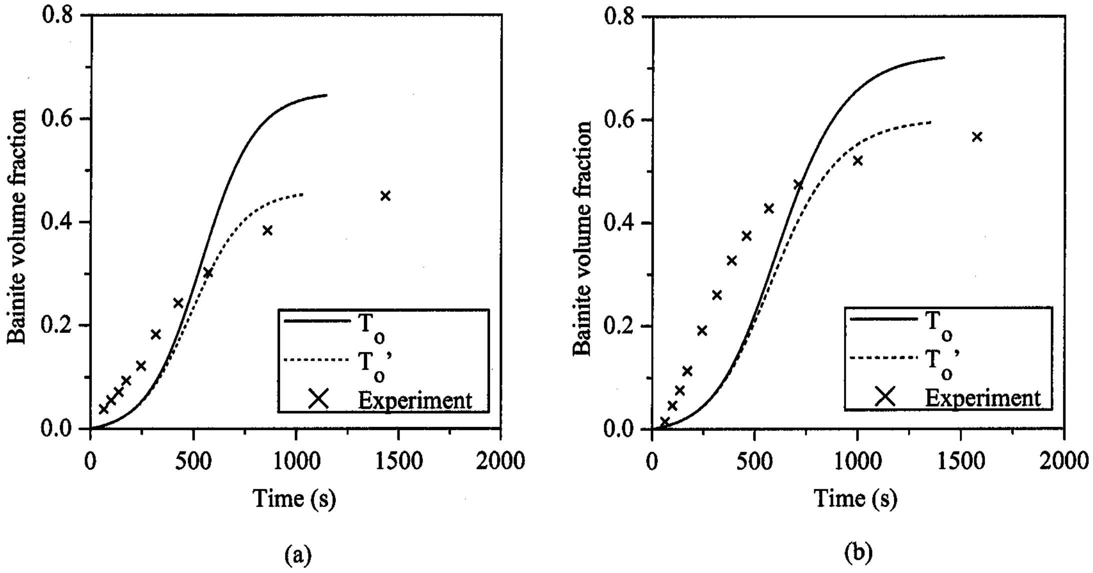

(a)

(b)

Figure 9.25: Comparison between calculated and measured bainite transformation kinetics for the Fe-Mn-Si-C steel, using the T_o and T_o' lines in the random nucleation model, at (a) 408 °C and (b) 353 °C.

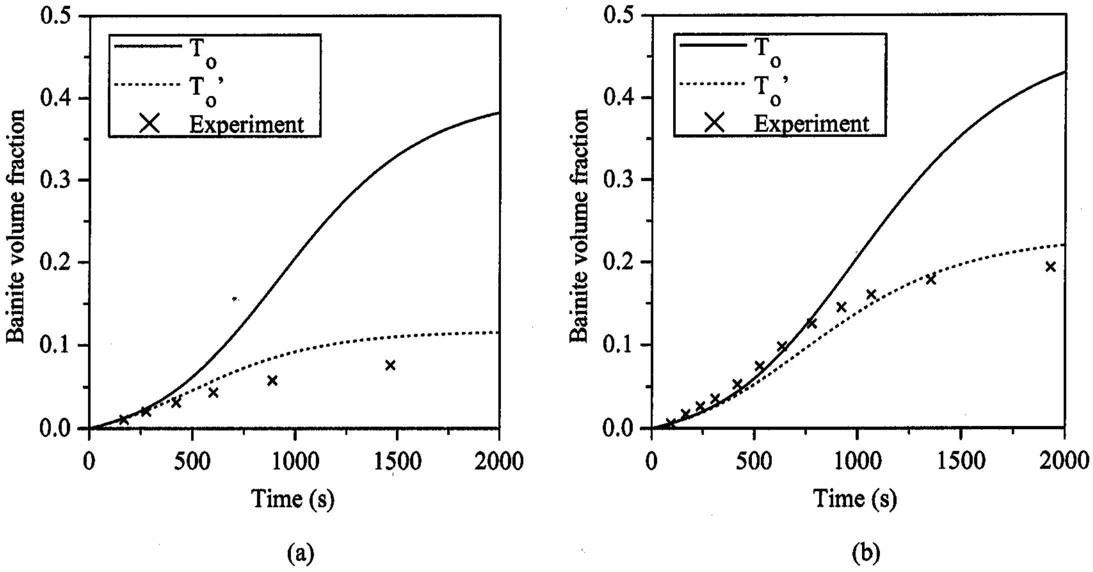

(a)

(b)

Figure 9.26: Comparison between calculated and measured bainite transformation kinetics for the 300M steel, using the T_o and T_o' lines in the random nucleation model, at (a) 425 °C and (b) 391 °C.

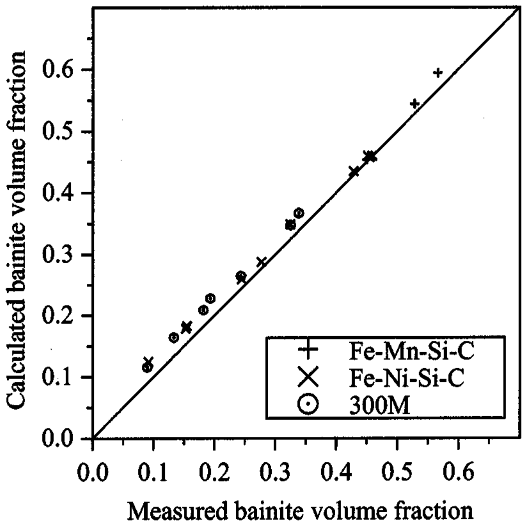

Figure 9.27: Comparison between calculated and measured isothermally transformed bainite volume fractions for three steels, using the random nucleation model.

of bainite under certain conditions, but the formation of the other phases prevents this occurring in reality. This problem proved intractable in the time available, despite detailed analysis of both the metallurgy and mathematics of the theory. Possible areas for further validation include the competition between Widmanstätten ferrite or pearlite and bainite, and the behaviour of the transformation kinetics theory at fast cooling rates. The original bainite theory was developed for Si-rich bainitic steels. It is possible that modifications are required for application to the processing of low-Si HSLA steels.

9.5 Computation Issues

9.5.1 Variable Timestep

During the early work, a constant time step (taken as one second) was used to model continuous cooling transformation, which required the nucleation and growth rates to be recalculated after every second of transformation. This procedure becomes impractical at slow cooling rates and inaccurate at faster rates. Different phases also form at different rates, and time intervals that are sufficiently small for one phase are not necessarily suitable for another. It was therefore decided to allow the time step to vary.

The effect of using different time steps, Δt, on the transformation over a range of cooling rates was investigated (Figure 9.31). There was little effect at the slowest cooling rate

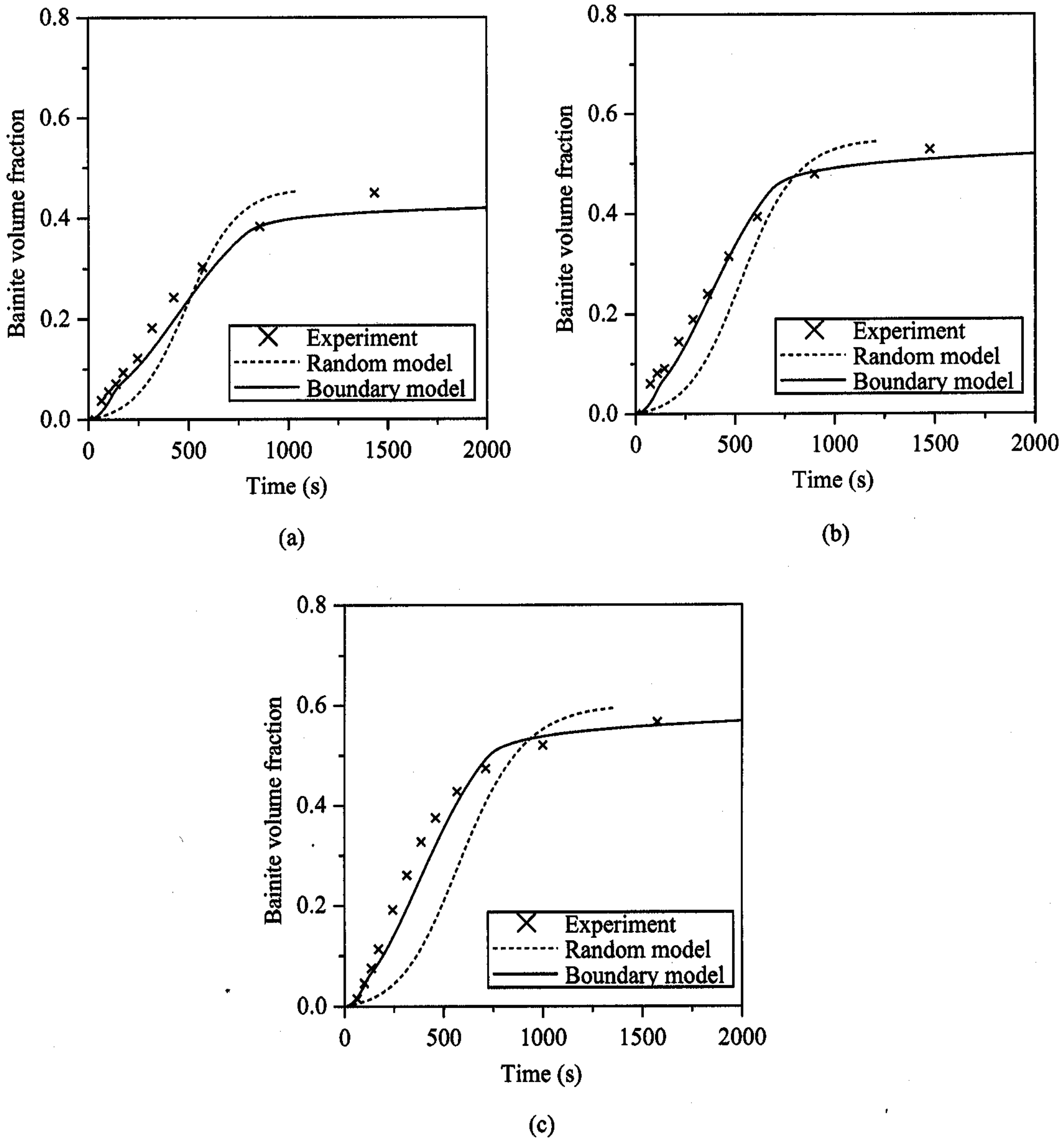

Figure 9.28: Comparison of random and boundary bainite nucleation models with experimental results for the Fe-Mn-Si-C steel at (a) 408 °C, (b) 380 °C and (c) 353 °C.

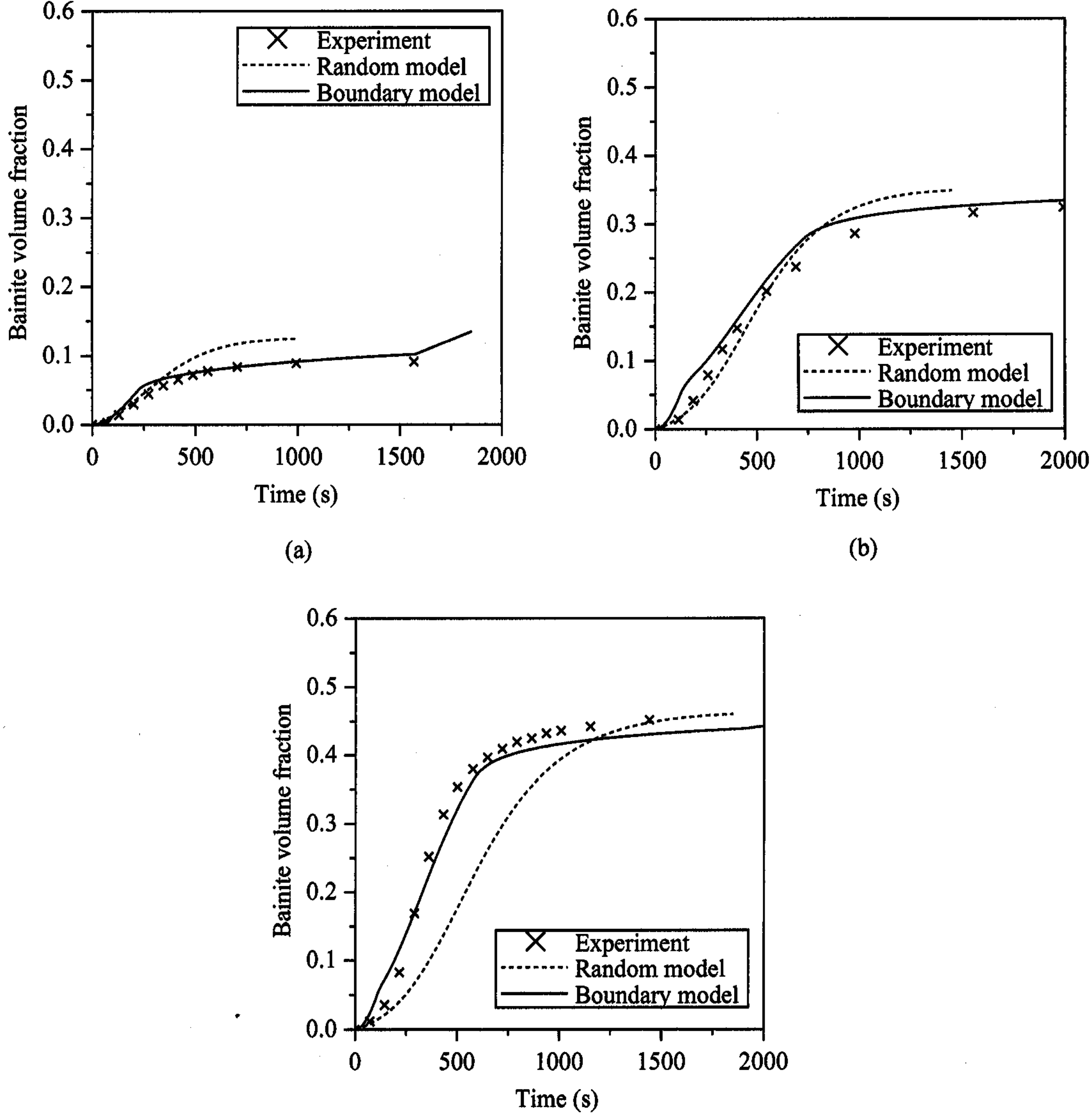

(a)

(b)

(c)

Figure 9.29: Comparison of random and boundary bainite nucleation models with experimental results for the Fe-Ni-Si-C steel at (a) 455 °C, (b) 391 °C and (c) 350 °C.

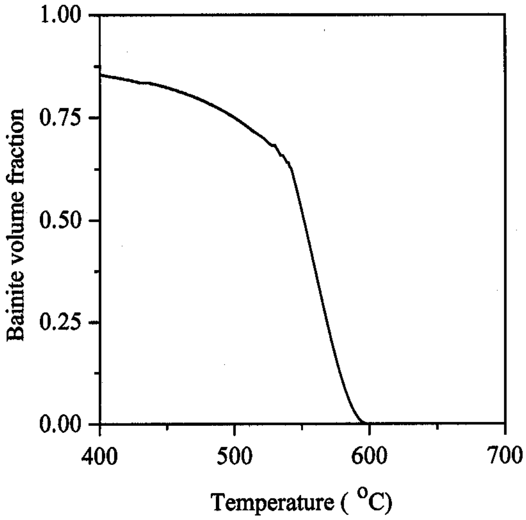

Figure 9.30: Calculated bainite kinetics for steel BS1 (0.1 C, 0.31 Si, 1.42 Mn wt.%), austenite grain size 10 μm, cooled at 1 °C s^{-1}. Nucleation and growth rates of all other phases were set to zero.

but increasing differences appeared at faster rates. Obviously, a suitable time step is one where a further decrease in step size makes minimal difference to the results. Large time steps mean that the nucleation and growth rates are recalculated less frequently, leading to greater inaccuracies in volume fraction at fast cooling rates. This problem becomes even more pronounced for phases that transform very rapidly, such as Widmanstätten ferrite.

It was found that a timestep of 1 s was adequate for the slow cooling rates (0.5 and 0.05 °C s^{-1}) whereas steadily smaller time steps were required as the cooling rate increased to maintain any sort of accuracy, 0.2 s being a typical value for a 20 °C s^{-1} cooling rate.

Several methods of varying the time step during a calculation were incorporated into the model. Firstly, the initial time step for each new cooling rate was selected, according to the criteria in Table 9.5. The time step was then reduced or increased accordingly if transformation was proceeding too rapidly or too slowly, as illustrated by the flowchart in Figure 9.32. This is particularly important when approaching completion at slow cooling rates, when the transformation can slow down considerably. Figure 9.33 shows that increasing the time step to several hundred seconds towards the end of the reaction has little effect on the results when compared against those with a maximum of 10 s steps. The saving in computation time using the larger time step, however, is considerable.

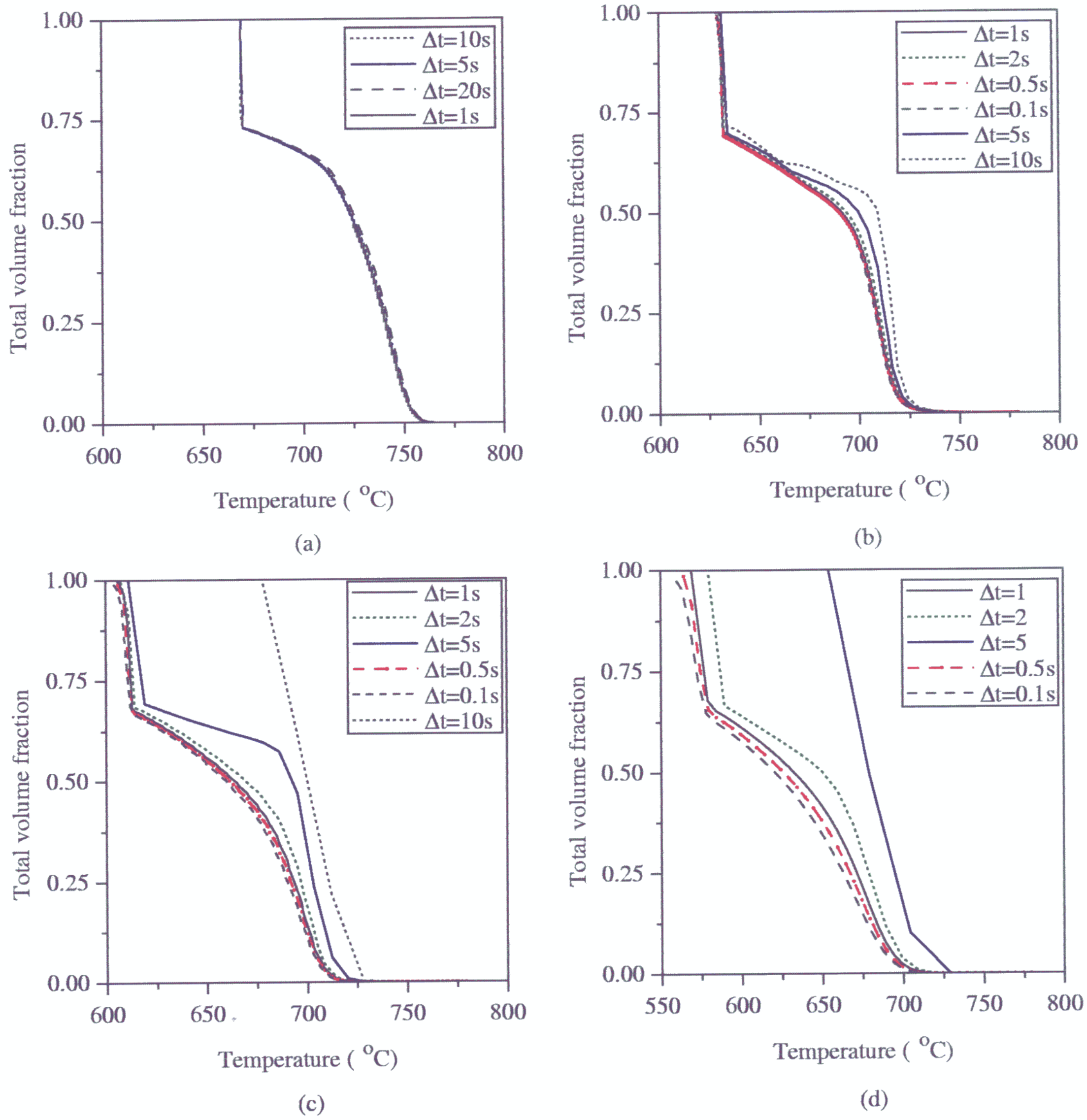

Figure 9.31: Effect of different constant time steps, Δt, on the transformation of a C-Mn-Si steel with austenite grain size 30 μm, at linear cooling rates of (a) 0.05, (b) 0.5, (c) 1.68, and (d) 5.0 °C s^{-1}.

Cooling rate (°C s^{-1})	Δt (s)
< 0.1	10
< 0.5	2
< 1	1
< 5	$CR/10$
< 10	$CR/20$
< 25	$CR/100$
< 100	$CR/1000$
≥ 100	$CR/5000$

Table 9.5: Initial timestep chosen by the transformation model for a particular cooling rate, *CR*.

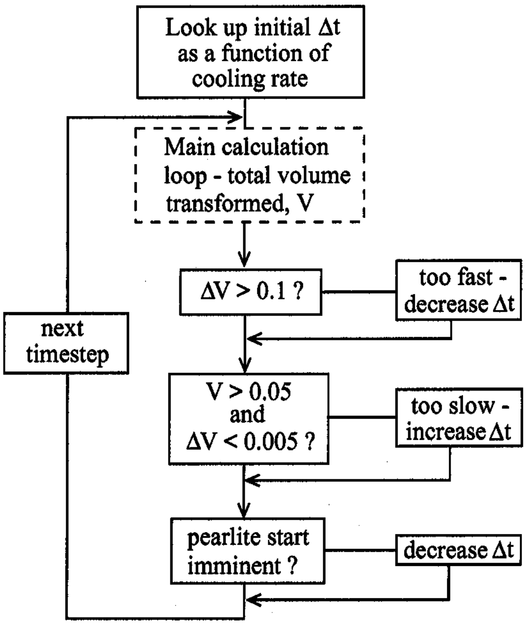

Figure 9.32: Flowchart showing the criteria for changing the timestep within the transformation model. V is the total transformed volume and ΔV is the change in total volume in the current time step.

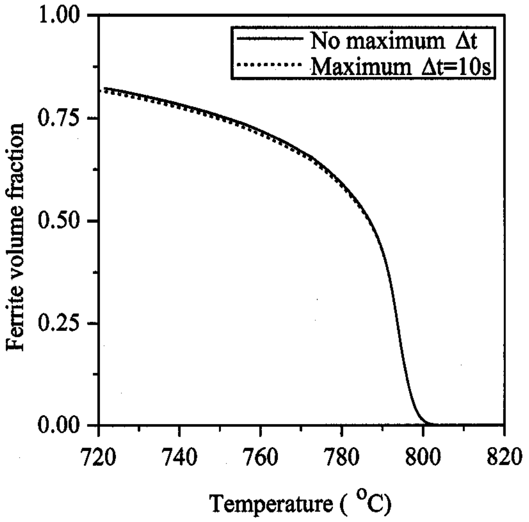

Figure 9.33: Effect of restricted and unrestricted variable time step on steel BST1, cooled at 0.01 °C s^{-1}.

9.5.2 Discontinuous Cooling Schedules

In a real rolling mill, the cooling rates applied to the steel are unlikely to be constant. The computer model has been adapted to allow for this in two ways. Firstly, a non-linear cooling curve can be used as long as it can be expressed as an equation of the form:

$$\Delta T = f\{\Delta t, T\} \tag{9.6}$$

where ΔT is the temperature interval and Δt the time interval for each calculation step in the model. At each temperature during cooling, ΔT and Δt are re-calculated from this equation and the new values used for the current transformation step. This is facilitated by the incorporation of the variable time step discussed in the previous section. Alternatively, the cooling schedule can be expressed as a series of isothermal and anisothermal stages. This would enable a mill schedule containing a hold during cooling, or a change in cooling rate, to be modelled. The program was modified to accept a sequence of these stages, and the time step checked at each temperature interval to ensure that the time spent on each stage was exactly as specified. An example schedule and the resultant calculated transformation curve are shown in Figure 9.34.

9.6 Summary

The simultaneous transformation model for four phases – allotriomorphic ferrite, Widmanstätten ferrite, pearlite and bainite – has been validated against many different sources

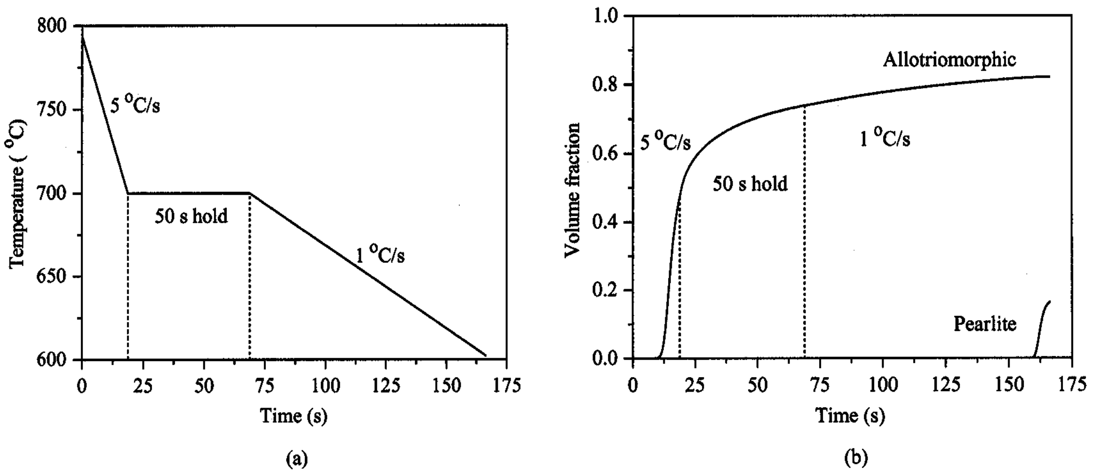

Figure 9.34: (a) Example discontinuous cooling schedule, and (b) corresponding transformation curve for steel BS1, austenite grain size 20 μm.

of experimental data. The effect of changing the density of nucleation sites and the shape factors affecting the energy of these sites has been investigated, and a set of optimum parameters for these values has been derived. The calculated allotriomorphic ferrite grain sizes have been successfully verified against experimental values. The volume fractions of allotriomorphic ferrite, Widmanstätten ferrite and pearlite were compared with data obtained from both isothermal and continuous cooling experiments for a range of low alloy steels. Excellent predictions of the microstructure were obtained at small and large austenite grain sizes. However, the balance between allotriomorphic ferrite and Widmanstätten ferrite at intermediate grain sizes was found to be problematic and requires further investigation. A model for bainitic transformation was adapted for the simultaneous transformation framework, but an insufficient quantity of bainite was calculated during cooling due to competition from the other phases. Some computational issues have also been addressed to improve the accuracy, speed and usefulness of the computer model.

Chapter 10

Transformation from Deformed Austenite

The aim of thermomechanical processing is to refine the austenitic state and thus also the microstructure that forms on transformation. Hot-rolling leads to grain size reduction by successive rolling deformation and recrystallisation into ever finer grains. If the austenite is deformed without recrystallisation then the grains retain an elongated, "pancaked shape" and contain additional defects such as dislocations which contribute to the energy stored in the austenite. Finally, there is a role for microalloying elements (Nb, V, Al) in thermomechanically processed steels. These serve to pin the austenite grain boundaries by forming carbonitrides and hence lead to further refinement. This chapter deals with transformations from austenite which has been plastically deformed. The mechanical stabilisation of displacive transformations has not yet been incorporated in the analysis.

Plastic deformation increases the austenite grain boundary area per unit volume, there is an increase in the stored energy due to defects (which may contribute to the driving force for the $\gamma \rightarrow \alpha$ transformation), and the number density and potency of heterogeneous nucleation sites may increase.

10.1 Austenite Grain Surface Area

Allotriomorphic ferrite usually nucleates heterogeneously on austenite grain boundaries and thus the amount of boundary area per unit volume, S_v, has a significant effect on transformation kinetics. When austenite is deformed, the grains elongate whilst keeping the same volume, leading to an increase in S_v (Figure 10.1). Additional nucleation sites may also be generated at deformation bands leading to a further increase in S_v. Thus, the effective surface area per unit volume of austenite can be written as [49]:

$$S_v^{eff} = S_v^{gb} + S_v^{db} \tag{10.1}$$

where the superscripts *gb* and *db* indicate the contributions from the grain boundary and deformation bands, respectively. The surface area per unit volume in fully recrystallised austenite is a function of the equiaxed austenite grain size, d_γ, expressed as a mean lineal intercept [145]:

$$S_v^o = \frac{2}{d_\gamma} \tag{10.2}$$

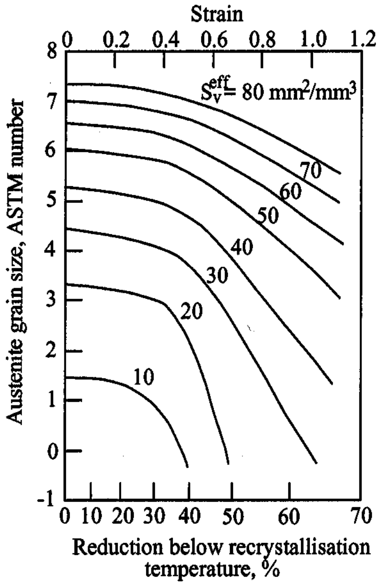

Figure 10.1: Variation of effective austenite surface area per unit volume, S_v^{eff}, with rolling reduction below the recrystallisation temperature (after Kozasu [145]).

Several researchers have derived equations for the effect of rolling reduction on S_v, six of which are summarised in Table 10.1. Some of the relationships are empirical [57, 131], whereas others are based on the geometry of the austenite grain [132–135]. Ouchi *et al.* and workers at CEIT used functions for S_v^{gb} based on the number of grain boundary intercepts a line of unit length would make parallel and perpendicular to the rolling direction. DeArdo and co-workers considered a simple cubic austenite grain under plane strain conditions [132]. Umemoto and Tamura [135] chose a spherical austenite grain of unit radius deformed by a rolling reduction p to an ellipsoid with axes 1, $1-p$ and $\frac{1}{1-p}$ (Figure 10.2). They deduced that the surface area of the grain boundaries is given by:

$$S_v^{gb} = \int_{-1/1-p}^{1/1-p} \left[\left\{ 4x \int_0^{\frac{\pi}{2}} \sqrt{1-(2p-p^2)\sin^2\theta}\, d\theta \right\} \sqrt{\frac{x^2(1-p)^6}{1-x^2(1-p)^2}+1} \right] dx \tag{10.3}$$

The ratio of the surface areas before and after rolling as a function of p and strain $\varepsilon = -\ln(1-p)$ is illustrated in Figure 10.3. A polynomial fitted to this curve for ease of calculation is given in Table 10.1.

Only two of the researchers presented specific equations for S_v^{db}. Ouchi and co-workers found that the density of deformation bands was only a function of strain and was significant when $\varepsilon > 0.3$. Umemoto and colleagues proposed a quadratic relationship with strain, which has also been used by other workers including Anelli.

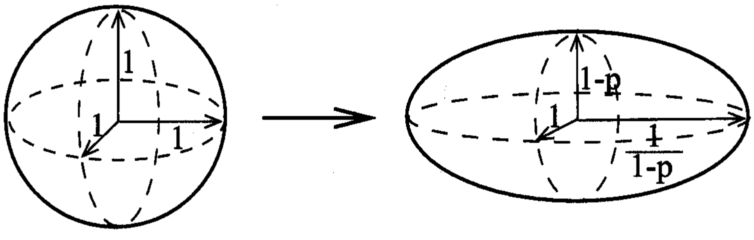

(a) (b)

Figure 10.2: Shape change of a spherical austenite grain due to rolling reduction p, (a) before rolling (sphere), (b) after rolling (ellipsoid) (after Umemoto and Tamura [135]).

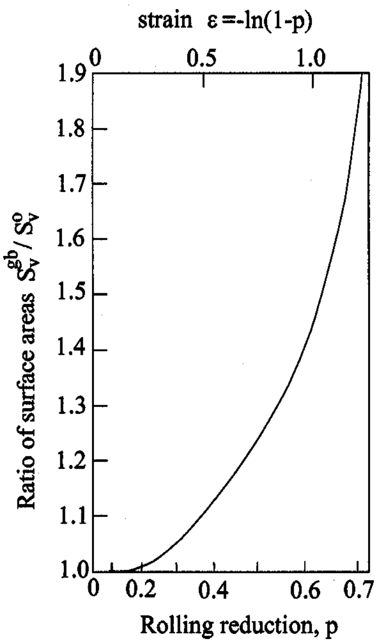

Figure 10.3: Ratio of austenite grain surface area before and after rolling as a function of rolling reduction p and strain ε (after Umemoto and Tamura [135]).

Experimental measurements of S_v^{eff} on a series of Nb and V microalloyed steels after thermomechanical processing were made by Sandberg and Roberts [139]. As expected, both S_v^{gb} and S_v^{db} increased with rolling reduction, the contribution from the grain bound-

Reference	S_v^{gb} **(mm^{-1})**	S_v^{db} **(mm^{-1})**
Anelli *et al.* [57]	$S_v^o(1+0.534\varepsilon)\varepsilon^{0.385\varepsilon}$	$30\varepsilon^2$
Yoshie *et al.* [131]	$\frac{4S_v^o}{\pi}(0.491\mathrm{e}^{\varepsilon}+0.155\mathrm{e}^{-\varepsilon}+0.143\mathrm{e}^{-3\varepsilon})$	–
DeArdo *et al.* [132]	$\frac{S_v^o}{2}[1+\mathrm{e}^{-\varepsilon}+\mathrm{e}^{\varepsilon}]$	$63(\varepsilon-0.3)$
Ouchi *et al.* [133]	$S_v^o[1.67(\varepsilon-0.1)+1]$	$63(\varepsilon-0.3)$
CEIT [134]	$\frac{S_v^o}{2}\left[0.429(3\varepsilon^2+1)^{-\frac{1}{2}}+2.571(3\varepsilon^2+1)^{\frac{1}{2}}-1\right]$	–
Umemoto [135]	$0.1423\varepsilon^3+0.4537\varepsilon^2-0.0475\varepsilon+1.0$	$30\varepsilon^2$

Table 10.1: Equations for S_v^{eff} taken from the literature.

aries always exceeding that of the deformation bands. Their results were divided into two groups according to the nominal equiaxed austenite grain size prior to finishing, $d_\gamma^o = 50$ μm and $d_\gamma^o = 75$ μm, corresponding to S_v^o values of 40 and 27 mm^{-1}, respectively. The predictions of the combined $S_v^{gb} + S_v^{db}$ equations in Table 10.1 for the same conditions are compared in Figure 10.4. The S_v^{db} data are presented separately for the two available equations in Figure 10.5. It can be seen from the latter graphs that the quadratic function of strain used by Umemoto and Tamura accurately predicts the variations in S_v^{db}. The equations of Yoshie, Umemoto and Anelli looked promising for the overall data. However, an inconsistency was found in Anelli's equation at low strains (around 0.1), where S_v^{eff} was incorrectly calculated to be less than S_v^o. Of the two remaining equations, Umemoto's is based entirely on the geometry of the austenite grains and does not contain any composition-specific parameters, so this equation was considered the most suitable for calculating S_v^{eff}.

10.2 Stored Energy for Transformation

When steel is hot-rolled, the work done on the austenite can be determined from the area under the stress-strain curve. Once the flow stress of the steel has been exceeded, the austenite is deformed plastically and a proportion of the work will be stored in the material as strain energy due to the formation of dislocations and other defects, the rest being released as heat. Given sufficient time at a high enough temperature, recovery and recrystallisation will occur, the dislocation density will decrease and the stored energy is released. However, if the austenite does not have the chance to fully recrystallise before the ferrite transformation begins then the stored energy will raise the overall free energy of the austenite and thus increase the driving force for the ferrite transformation, $\Delta G^{\gamma\rightarrow\gamma'+\alpha}$, and for nucleation, ΔG_m (Figure 10.6). As can be seen from this diagram,

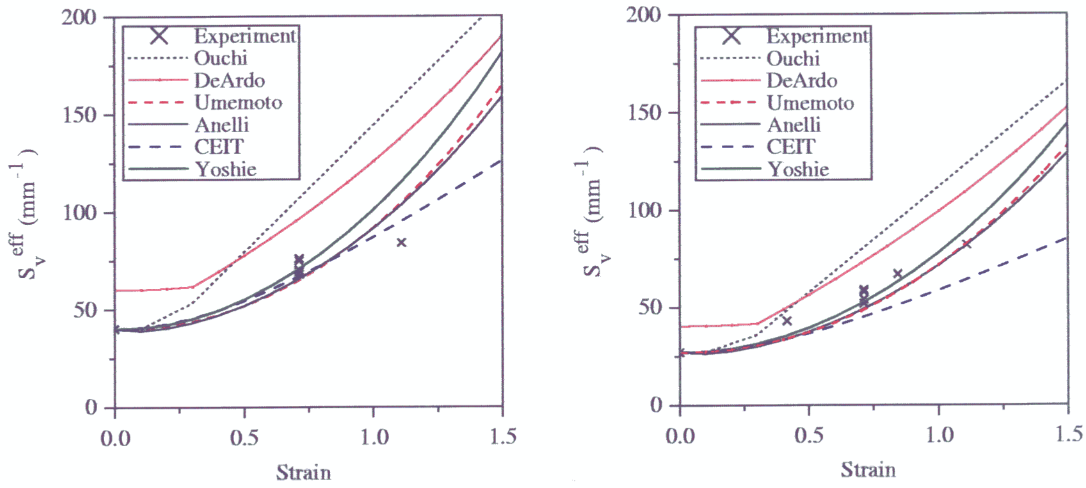

(a)

(b)

Figure 10.4: Comparison of equations for S_v^{eff} from the literature with experimental data of Sandberg and Roberts [139], (a) $S_v^o = 40\,\mathrm{mm}^{-1}$ and (b) $S_v^o = 27\,\mathrm{mm}^{-1}$.

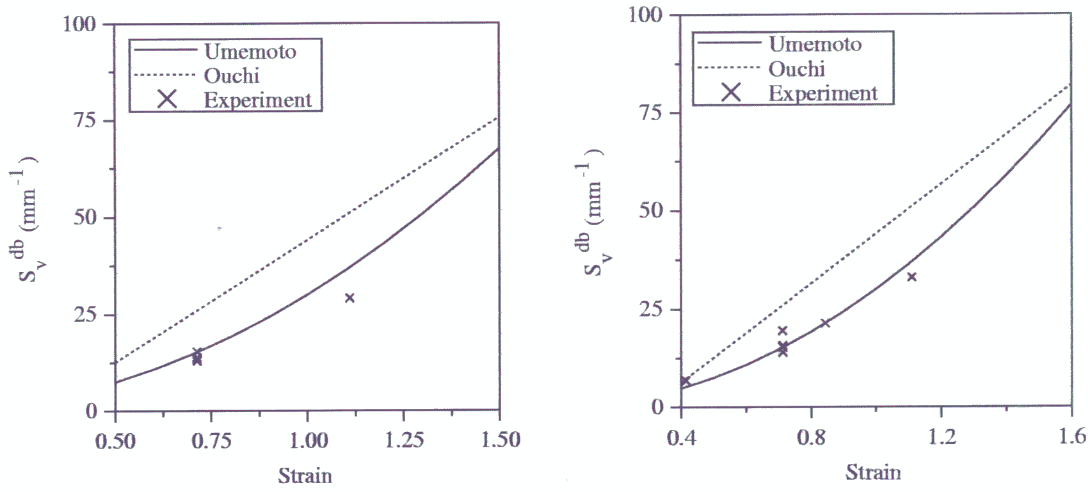

(a)

(b)

Figure 10.5: Comparison of equations for S_v^{db} from the literature with experimental data of Sandberg and Roberts [139], (a) $S_v^o = 40\,\mathrm{mm}^{-1}$ and (b) $S_v^o = 27\,\mathrm{mm}^{-1}$.

the equilibrium compositions of austenite and ferrite, $x^{\gamma\alpha}$ and $x^{\alpha\gamma}$, will also be affected. Figure 10.7 illustrates the effect of different values of stored energy (in J m^{-3}) on the paraequilibrium $\gamma/\gamma+\alpha$ phase boundary in a 0.1 C 0.31 Si 1.42 Mn wt.% steel. It can be seen that an increase in stored energy increases the paraequilibrium carbon content at each temperature. This also affects the parabolic rate constant, α_1, which is dependent on the equilibrium compositions (equation 3.21). The concomitant increase in parabolic rate constant for the same steel cooled at a constant rate of 1 °C s^{-1} is shown in Figure 10.8a. The rate constant is small at high temperatures where the driving force is low, but increases with the driving force as the temperature decreases. At lower temperatures, the growth rate decreases again because diffusion becomes more difficult. The same graph calculated for isothermal transformation at each temperature would show a smooth curve, but under constant cooling conditions other factors such as the carbon enrichment of the austenite affect the growth rate, producing the more irregular shaped curves. A higher stored energy produces a faster growth rate and moves the transformation to elevated temperatures.

The stored energy will also enhance the driving force for ferrite nucleation. The free energy change associated with formation of a new nucleus is given by (see Section 3.1.4):

$$\Delta G = -\frac{4\pi}{3}r^3(\Delta G_v + W) + 4\pi r^2\sigma_{\gamma\alpha} \tag{10.4}$$

where W is the strain energy per unit volume. The activation energy barrier to nucleation is then:

$$G^* \propto \frac{\sigma^3_{\gamma\alpha}}{(\Delta G_v + W)^2} \tag{10.5}$$

Thus, an increase in stored energy will reduce the activation energy barrier to nucleation compared with homogeneous nucleation. The nucleation rate is increased, particularly at temperatures close to the Ae_3 where nucleation is normally difficult, and thus the stored energy has the greatest effect (Figure 10.8b). The distinct sections of each curve are due to the contributions to the nucleation rate from the three grain boundary sites. Corner sites dominate the nucleation rate close to the Ae_3, then edge sites contribute, before the large number density of grain face sites take over. The effect of the stored energy on the overall transformation kinetics is illustrated in Figure 10.9. The volume fraction of allotriomorphic ferrite increases with W at each temperature due to the faster growth rate and the increased paraequilibrium fraction. The ferrite grain size actually increases slightly because the increase in the growth rate exceeds that of the nucleation rate. Therefore, even though more particles can nucleate, they also grow more rapidly and saturate the boundaries earlier in the transformation. The ferrite grain size in the model is determined only by the density of these boundary nuclei. This indicates that an additional mechanism is required to account for the refinement of ferrite grain size from the deformed austenite.

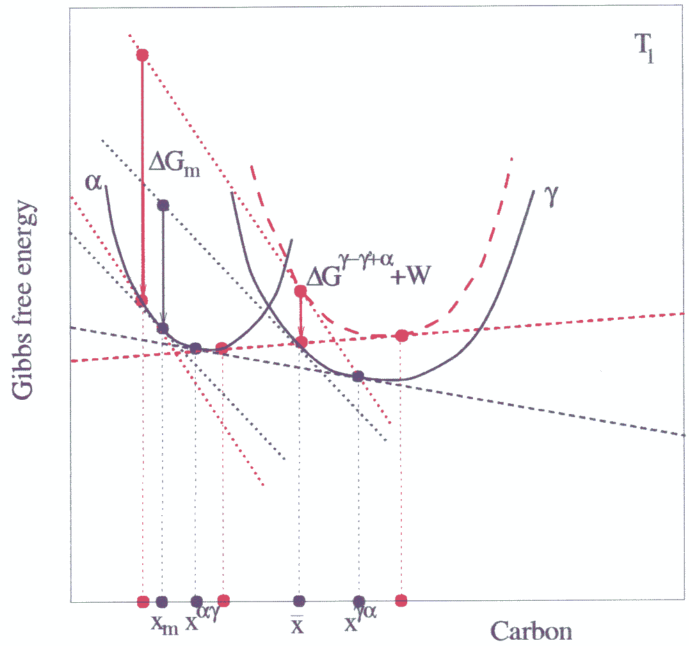

Figure 10.6: Schematic free energy *versus* composition diagram showing the effect of stored energy in austenite on the phase boundaries and driving forces. Tangents, free energy changes and compositions relating to the deformed austenite are highlighted in red, undeformed austenite in black.

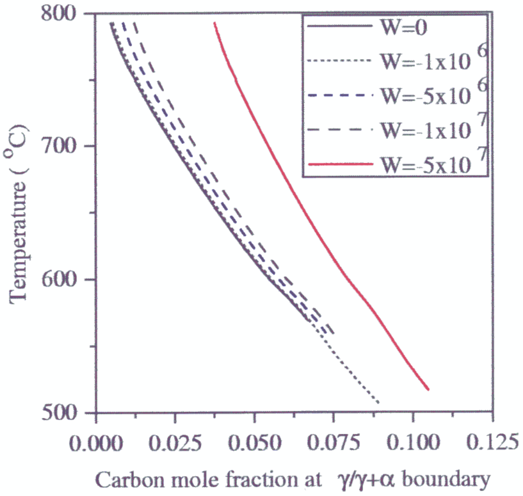

Figure 10.7: Calculated paraequilibrium Fe-C phase diagram for a 0.1 C 0.31 Si 1.42 Mn wt.% steel, showing effect of different values of stored energy (J m^{-3}) on the Ae'_3 boundary.

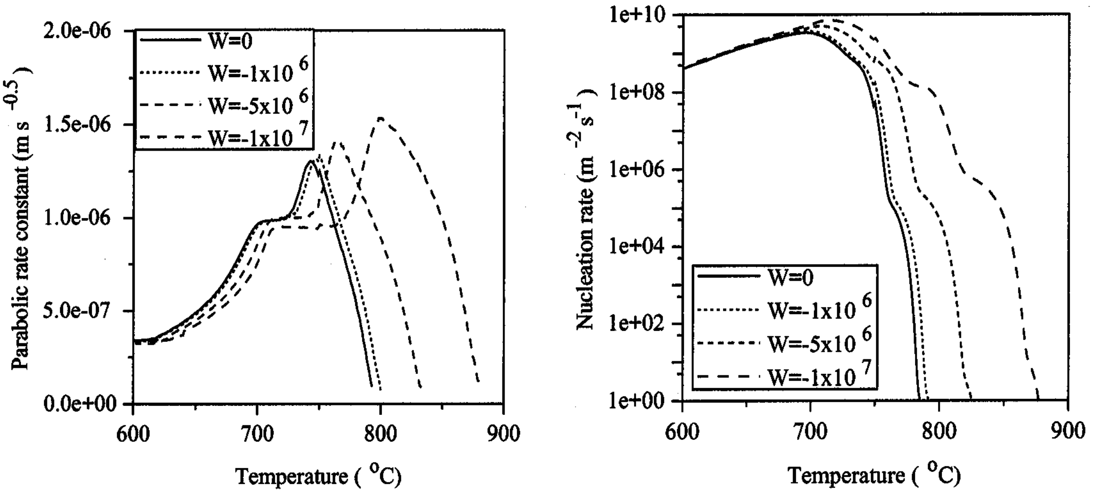

(a) (b)

Figure 10.8: Calculated (a) one-dimensional parabolic thickening rate constant and (b) grain boundary nucleation rate, for a 0.1 C 0.31 Si 1.42 Mn wt.% steel, austenite grain size 50 μm, cooled at 1 °C s^{-1} with different values of stored energy (J m^{-3}).

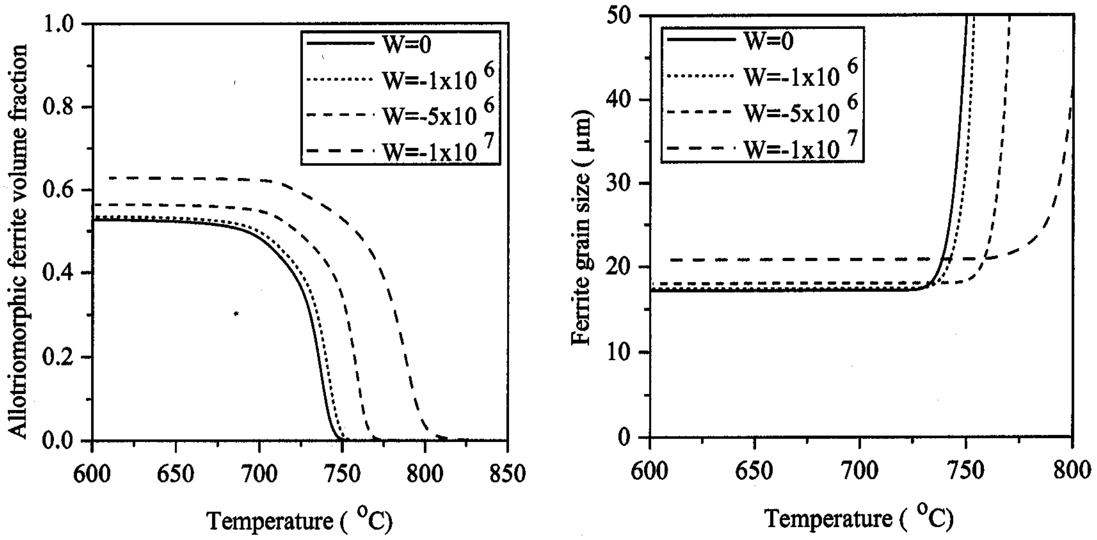

(a) (b)

Figure 10.9: Calculations for a 0.1 C 0.31 Si 1.42 Mn wt.% steel, austenite grain size 50 μm, cooled at 1 °C s^{-1}, illustrating the variation with stored energy (J m^{-3}) of (a) allotriomorphic ferrite volume fraction and (b) ferrite grain size.

10.2.1 Magnitude of Stored Energy

Ferrite can nucleate on deformation bands, which are regions of high dislocation density and thus high energy due to the strain field associated with each dislocation. Umemoto and Tamura showed that nucleation on dislocations was particularly favourable at large undercoolings and was also more favourable than boundary nucleation at lower transformation temperatures [135]. The energy per unit length of dislocation line is approximately:

$$\tau_d \approx \frac{\mu_o b^2}{2} \tag{10.6}$$

where μ_o is the shear modulus of the austenite and b the magnitude of the Burgers vector. If the dislocation densities per unit area before and after deformation are ρ_o and ρ then the stored energy per unit volume due to the new dislocations introduced by the deformation is:

$$W = -\tau_d(\rho - \rho_o) \tag{10.7}$$

Taking $\mu_o = 8.1 \times 10^{10}$ J m^{-3} and $b = 2.5 \times 10^{-10}$ m, typical values of ρ_o and ρ being 10^{12} and 10^{16} m^{-2} for fully recrystallised and heavily worked austenite, then W is of the order of 2.5×10^7 J m^{-3} (180 J mol^{-1}). The dislocation density is difficult to measure experimentally, but there is a proposed method for calculating it from the maximum flow stress, σ_{max}, in the last deformation pass before transformation [136]:

$$\rho = \left[\frac{\sigma_{max}}{k_M M \mu_T b}\right]^2 \tag{10.8}$$

where $k_M = 0.15$ is a constant, M is the Taylor factor (taken as 3.11 for a face-centred cubic structure) and μ_T is the temperature dependent shear modulus,

$$\mu_T = \mu_o \left[1 + \left(\frac{T - 300)}{T_M} \times \frac{T_M}{\mu_o} \times \frac{d\mu_T}{dT}\right)\right] \tag{10.9}$$

In austenite, $T_M = 1810$ K, $\frac{T_M}{\mu_o} \times \frac{d\mu_T}{dT} = -0.91$ and $\mu_o(300\,\text{K}) = 8.1 \times 10^{10}$ J m^{-3}.

An alternative method for calculating the stored energy is to consider the fraction of the work done during deformation that remains in the austenite. Liu and Karjalainen [137] proposed that the total stored energy after n passes below the recrystallisation stop temperature T_{nr} can be evaluated from:

$$W_s^{total} = \sum_{i=1}^{n} \alpha_s \overline{\sigma}_i \varepsilon_i \tag{10.10}$$

where $\overline{\sigma}_i$ and ε_i are the mean flow stress and strain of the i-th pass, respectively, and α_s is the fraction stored, suggested to be 0.1. Some measurements made by British Steel on the same 0.1 C steel discussed above gave average flow stress values of 150 MPa at $\varepsilon = 0.2$

and $\dot{\varepsilon} = 1\,\mathrm{s}^{-1}$, and 220 MPa at $\varepsilon = 0.4$ and $\dot{\varepsilon} = 10\,\mathrm{s}^{-1}$ [138]. Assuming only a tenth of the work is stored as energy, then $W = 3.0 \times 10^6$ and 8.8×10^6 J m^{-3}, respectively.

If the stored energy is to have a significant effect on the nucleation rate, it must be comparable in magnitude to the chemical driving force for nucleation, ΔG_v. This driving force is derived from the maximum free energy change available for the $\gamma \rightarrow \alpha$ transformation, as described in Chapter 3. Figure 10.10 shows the calculated value of ΔG_v for the 0.1 C steel as a function of temperature, and the effect on this of different values of stored energy. It can be seen that a stored energy of at least 1×10^6 J m^{-3} is required to have an effect on G^*. Therefore, the stored energy values determined above by two different methods are of sufficient magnitude to affect the transformation kinetics in the model.

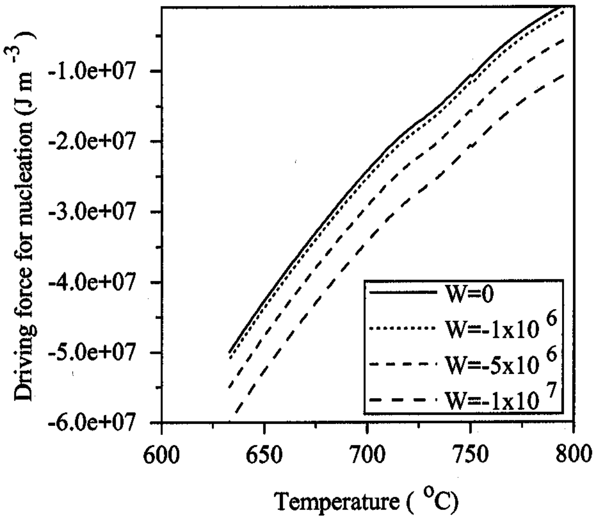

Figure 10.10: Calculated driving force for ferrite nucleation in a 0.1 C 0.31 Si 1.42 Mn wt.% steel, showing effect of different values of stored energy, W (J m^{-3}).

10.3 Nucleation Site Potency

Several researchers have found that for the same S_v, deformed austenite grains transform to a finer ferrite grain size than equiaxed grains [143, 144, 145]. The experimentally observed reduction in ferrite grain size and increase in ferrite nuclei density therefore cannot be explained by an increase in the number of nucleation sites due to an increase in S_v. There must also be an increase in the density per unit area and/or potency of these sites. Two possible mechanisms have been proposed for this. The first envisages 'bulges' in the austenite grain boundary formed by strain-induced boundary migration, which act as sites of similar nucleation potency to grain edges and corners [139]. Umemoto and Tamura [135] proposed a similar mechanism whereby the deformation introduces ledges or steps in the boundary which act as preferential sites due to a lower activation energy barrier. An alternative method suggests that partial recovery of the deformation sub-structure within the grains produces a network of dislocation sub-grains. Precipitates can form on this network and act as ferrite nucleation sites. The sub-grains are finer close to the boundary due to the strain gradient, and thus ferrite nucleation is enhanced in these regions [140].

Liu [141] theoretically assessed the relative effectiveness of grain boundaries and deformation bands at catalysing ferrite nucleation *via* the activation energy barrier, G^*. Assuming that the chemical driving force and strain energy were the same for nucleation at both these sites, he concluded that the boundaries were always more potent than the deformation bands, no matter how heavy the deformation.

Quantifying the increase in nucleation is quite difficult. Umemoto and co-workers [142] estimated the number of ferrite grains intercepted per millimetre of austenite boundary from steel specimens subjected to 0, 30 and 50% reduction as 41, 214 and 330 mm^{-1}, respectively. The number of ferrite grains per unit boundary area is proportional to the square of these numbers and the square root of the nucleation rate per unit area. Therefore, the nucleation rate is approximately 740 ($(\frac{214}{41})^4$) and 4200 ($(\frac{330}{41})^4$) times faster than with no deformation for 30% and 50% reduction respectively.

The nucleation site density, and thus nucleation rate per unit boundary area, in the model can be altered by changing the fraction of active sites K_1^f. The default value for recrystallised austenite, as derived in the previous chapter, was 1×10^{-9}. An increase in K_1^f leads to a decrease in ferrite grain size, as shown in Figure 9.7. This knowledge can be used to attempt to model the increase in nucleation sites due to deformation of the austenite.

10.4 Calibration of the Transformation Model

The increase in allotriomorphic ferrite volume fraction and the decrease in ferrite grain size observed when unrecrystallised austenite is transformed is difficult to model precisely. As discussed in the preceding sections, the fraction of active nucleation sites, K_1^f, refines the ferrite grain size whilst the stored energy W can increase the volume fraction, though often at the expense of an increase in grain size as well. The model was calibrated against several sources of experimental data on allotriomorphic ferrite grain sizes and volume fractions. The compositions of the steels which were investigated are summarised in Table

10.2.

Reference	C	Si	Mn	Ni	Cr	Al	Nb	V	Ti
Cuddy Nb [143]	0.12	0.25	1.55	–	–	0.041	0.049	–	0.018
Cuddy V [143]	0.12	0.24	1.52	–	–	0.023	–	0.096	0.015
Kozasu [145]	0.16	0.36	1.41	–	–	0.02	0.03	–	–
CEIT BS1 [134]	0.10	0.31	1.42	0.02	<0.02	0.039	0.035	<0.005	<0.005
CEIT HO5 [147]	0.082	0.36	1.47	0.03	0.02	0.053	0.051	0.08	<0.005
Siwecki [146]	0.12	0.3	1.3	–	–	0.02	–	0.09	–

Table 10.2: Composition in wt.% of steels used for validating deformed austenite model.

10.4.1 Ferrite Grain Size Calculations

Cuddy investigated ferrite grain refinement after accelerated cooling of recrystallised and unrecrystallised austenite in steels microalloyed with V or Nb [143, 144]. The ferrite grain size was found to decrease as S_v and cooling rate increased, as expected. However, for a given S_v, the grain size derived from deformed, unrecrystallised austenite was consistently smaller than that from a fully recrystallised structure, thus indicating that additional factors other than the increased S_v were contributing to the nucleation. This was attributed to bulges in the austenite boundary producing a higher nucleation potency for a unit area of deformed boundary compared with an undeformed boundary.

Calculations performed with the new transformation model on the base 0.12 C 0.25 Si 1.5 Mn wt.% steel used by Cuddy (but without Nb, which is not included in the model), cooled at 1 °C s^{-1} and assuming fully recrystallised austenite, showed a decrease in ferrite grain size consistent with the recrystallised experimental results, but over-estimated the grain sizes from deformed austenite (Figure 10.11). Figure 10.12 compares the initial predictions for recrystallised and unrecrystallised austenite against experimental data on a recrystallised V steel and an unrecrystallised Nb steel at three cooling rates. The calculations again fit the recrystallised data successfully but over-estimate the unrecrystallised results by about 2 μm. Only the increase in S_v due to the deformation was included in the unrecrystallised calculations. In an attempt to model the increased potency of the deformed boundaries, the nucleation site density was increased by raising K_1^f. An increase of between 100 and 1000 times produced a good fit to the unrecrystallised data at each cooling rate. Applying the same increases to the data in Figure 10.11, it was found that a 1000 times increase in the active sites replicated the experimental data quite accurately. Figure 10.13 now compares the original recrystallised and new, increased sites, unrecrystallised results.

The accumulated strain in each of the experimental specimens was not precisely stated in the papers, but reductions of between 75 – 85 % were applied below T_{nr}. The thousand-fold increase in boundary nucleation rate is smaller than that suggested by Umemoto for a less severe deformation (4200 times) [142], though of the same order of magnitude. Multiplication of the nucleation rate by 4200 tended to produce a too small ferrite grain size at large values of S_v, whereas the results at smaller S_v were very similar to the 1000 times values. This is because at larger austenite grain sizes, the available boundary area saturates quite early in the transformation, thus fixing the ferrite grain size before any differences in the nucleation rate can have a major effect on the number of boundary nuclei (which define the grain size in the model). With smaller austenite grains, the amount of boundary area is much greater and often it is not completely saturated until the end of the transformation. Differences in nucleation rate have a more significant effect on ferrite grain size in this case, as the total number of boundary particles builds up throughout the whole transformation.

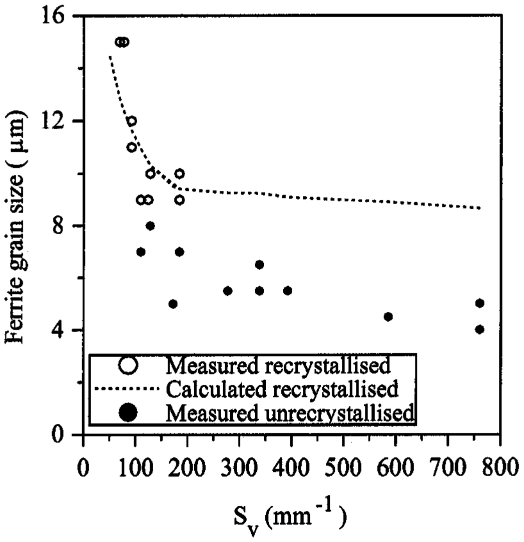

Figure 10.11: Calculated variation of ferrite grain size with S_v in a 0.12 C 0.25 Si 1.5 Mn wt.% steel cooled at 1 °C s^{-1}, assuming fully recrystallised austenite, compared with experimental data for recrystallised and unrecrystallised austenite [143].

Kozasu [145] reported some detailed experiments on the thermomechanical processing of a 0.16 C 0.36 Si 1.41 Mn 0.03 Nb wt.% steel. Specimens were air-cooled from three different initial austenite grain sizes, 225, 50 and 25 μm, which had been subjected to reductions of between 0 and 70% below T_{nr}. The measured variation of ferrite grain size with S_v is compared with the calculations of the model in Figure 10.14. It can

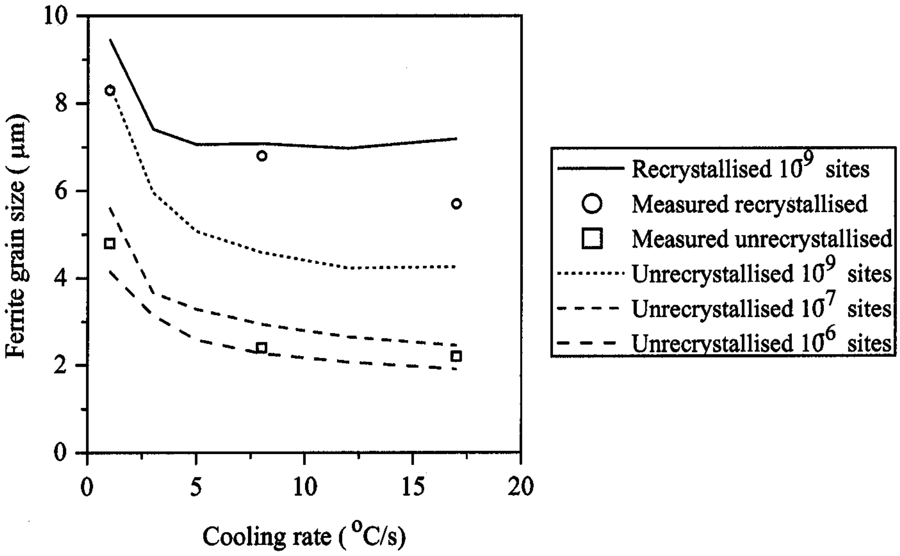

Figure 10.12: Calculated variation of ferrite grain size with cooling rate in a 0.12 C 0.25 Si 1.5 Mn wt.% steel, compared with experimental data for a recrystallised V steel and an unrecrystallised Nb steel [143].

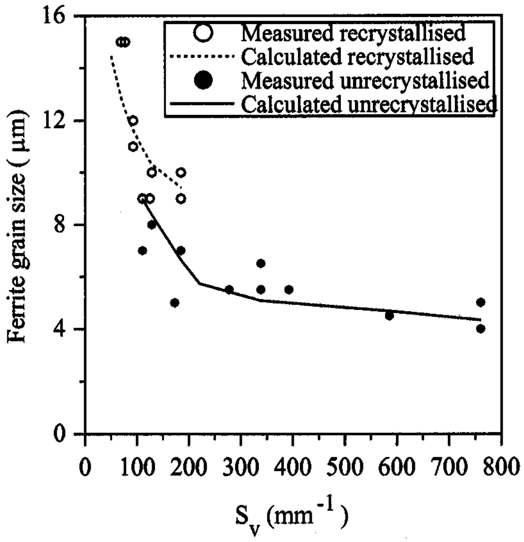

Figure 10.13: Calculated variation of ferrite grain size with S_v in a 0.12 C 0.25 Si 1.5 Mn wt.% steel cooled at 1 °C s^{-1}, with a 1000 times increase in active nucleation sites between the recrystallised and unrecrystallised austenite calculations.

be seen that the model can predict the recrystallised grain sizes quite accurately with $K_1^f = 1 \times 10^{-9}$. The effect of increasing K_1^f to account for the additional sites introduced by the deformation is also illustrated. At small values of S_v, an increase of 10 or 100 times in the fraction of active sites was sufficient to refine the grain size, whilst at larger S_v values, a 10,000-fold increase was required ($K_1^f = 1 \times 10^{-5}$). It might be expected that the more heavily deformed samples would require a larger fraction of active sites to model the grain size. However, no consistent relationship was found.

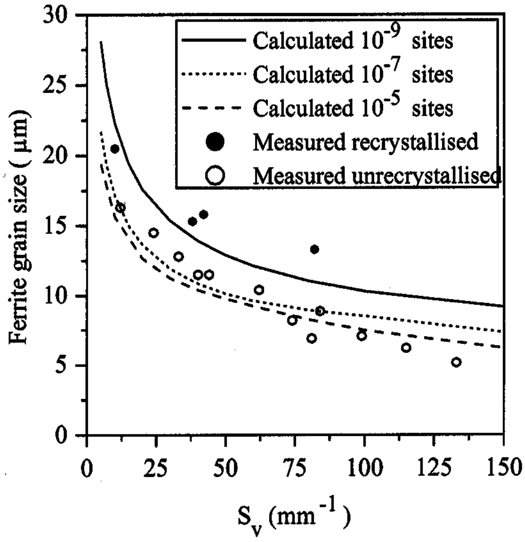

Figure 10.14: Calculated variation of ferrite grain size with S_v and K_1^f in a 0.16 C wt.% steel cooled at 1 °C s^{-1}, compared with experimental data of Kozasu for recrystallised and unrecrystallised austenite [145].

Hot-torsion experiments were performed by CEIT, Spain on steel BS1 [134] to investigate the change in microstructure after cooling from unrecrystallised austenite at rates of 1 and 5 °C s^{-1}. Figure 10.15 plots the calculated and measured ferrite grain sizes as a function of S_v. In both cases, the model initially over-estimated the grain sizes, so once again K_1^f was increased to refine them. An increase of at least 10,000 times was required at both cooling rates to predict the experimental data. The calculated results for the 5 °C s^{-1} cooling rate were slightly closer to the measured values.

In contrast to the work on niobium steels, Siwecki *et al.* found that the ferrite grain sizes formed in vanadium microalloyed steels varied with S_v only, independent of the processing route by which they were obtained, *i.e.* from recrystallised or unrecrystallised austenite [146]. This was attributed to the finer austenite grain size of the V steel, where the site densities of edge and corner sites are high and are suggested to be as effective nu-

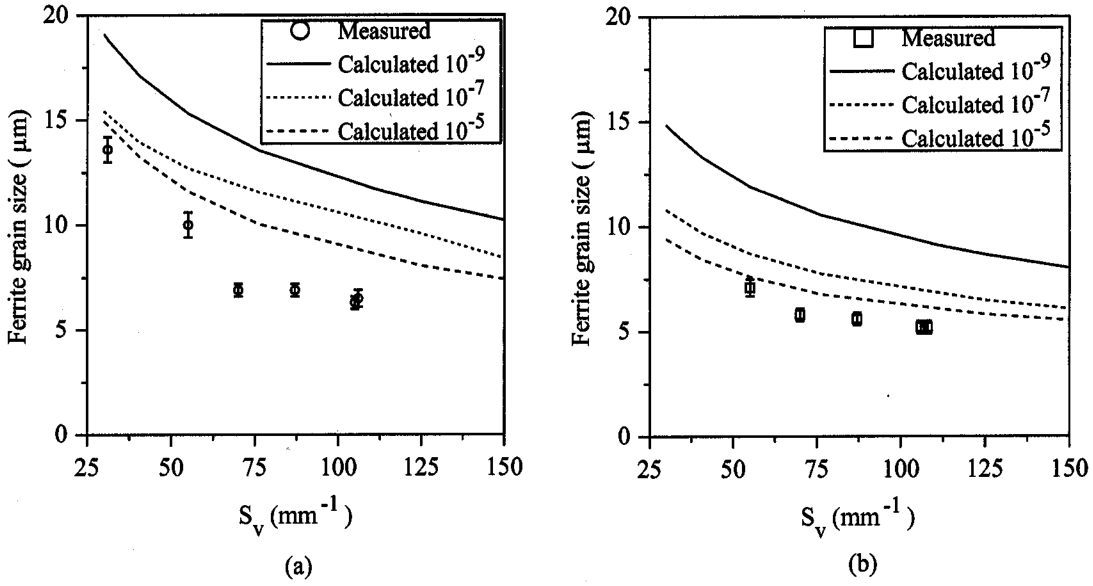

(a)

(b)

Figure 10.15: Calculated variation of ferrite grain size with S_v and K_1^f in steel BS1 compared with experimental data of CEIT [134] cooled from unrecrystallised austenite at (a) 1 °C s^{-1}, (b) 5 °C s^{-1}. Error bars are 95% confidence limits.

cleation sites as the bulges in the deformed grain surfaces. Therefore, the same nucleation sites would tend to dominate for both equiaxed, recrystallised grains and deformed grains and the variation of ferrite grain size with S_v would be very similar regardless of grain shape. Figure 10.16 shows that the calculations of the model for a 0.12 C 0.3 Si 1.3 Mn 0.09 V wt.% steel, cooled at 0.88 and 5 °C s^{-1}, over-estimated the ferrite grain size for both the recrystallised and unrecrystallised steels. The over-estimation was smaller at the faster cooling rate. A ten-fold increase in site density was sufficient to accurately predict the 5 °C s^{-1} results, whereas at least a 100 times increase was necessary at 0.88 °C s^{-1}, but as there appears to be no distinction between the recrystallised and unrecrystallised experimental results, then this does not help calibrate the model.

It does, however, highlight the difficulty of accurately predicting the effects of unrecrystallised austenite on subsequent transformation. Although the ferrite grain size from the recrystallised austenite was accurately predicted for the Cuddy and Kozasu data, it was not for the Siwecki results. The increase in site density required to correct the latter predictions casts doubt on the exact magnitude of the increase needed for the other steels which can be attributed solely to unrecrystallised austenite. There was also no indication of the magnitude of the error in the experimental measurements as reported in the papers. The ferrite grain sizes themselves are quite small and the difference between those from recrystallised and unrecrystallised austenite is only a few micrometres, so a large error in the measurements could be significant. Another important factor not incorporated in the model is the possible effect of Nb and Nb or V carbide/nitride precipitates on the ferrite transformation. These precipitates not only inhibit grain growth in the austenite to refine its structure, but can also act as nucleation sites for ferrite. Nb has also been observed to lower the ferrite transformation start temperature [133]. Soluble Nb segregates to the austenite grain boundaries where it lowers the boundary energy and thus increases the activation energy for ferrite nucleation. These effects could be obscuring the true effect of the deformation on the transformation.

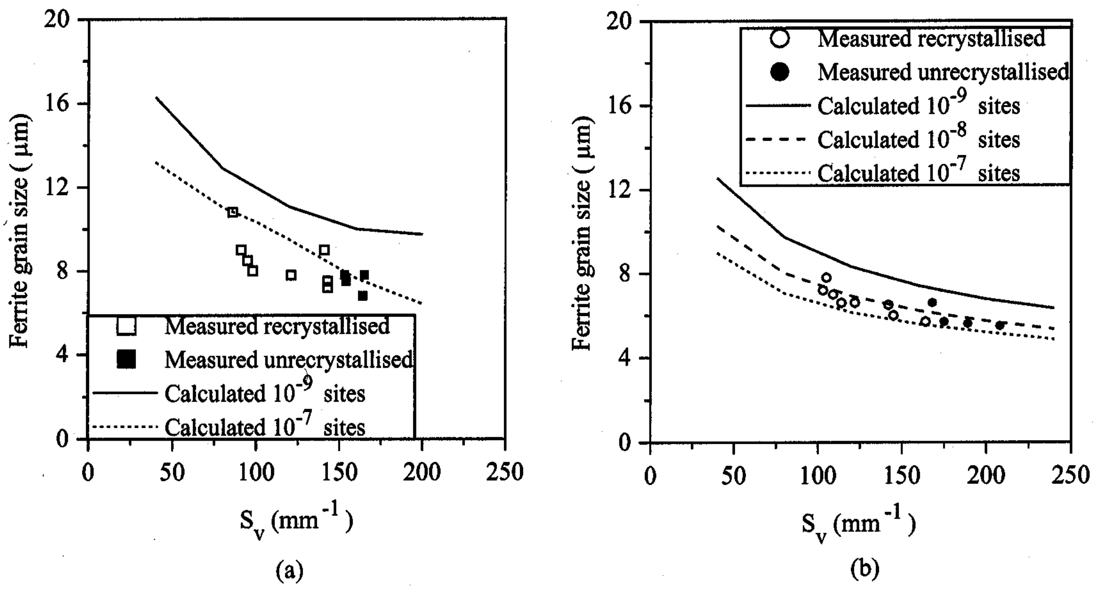

Figure 10.16: Calculated variation of ferrite grain size with S_v in a 0.12 C 0.3 Si 1.3 Mn 0.09 V wt.% steel compared with experimental data of Siwecki *et al.* [146], cooled at (a) 0.88 °C s^{-1}, (b) 5 °C s^{-1}.

10.4.2 Ferrite Volume Fraction Calculations

Thermomechanical simulation experiments were performed on a hot torsion machine at CEIT, Spain [147, 134] on steel HO5. Samples were transformed under the same conditions from both a fully recrystallised and an unrecrystallised austenite structure to enable comparison between the kinetics and microstructure produced in each case. Samples were reheated at 1200 °C for 15 minutes, and then deformed using a 7-pass torsion test at decreasing temperatures to refine the austenite grain size by static recrystallisation. The unrecrystallised austenite structure was generated by a further 7 passes below the recrystallisation stop temperature at a strain rate of 1 s^{-1} and strain per pass of 0.2, finishing at 800 °C. In both cases, a controlled cooling rate of 1 °C s^{-1} was applied after the deformation. Specimens were quenched out at a series of temperatures during cooling and quantitatively analysed by optical microscopy. The recrystallised austenite grain size was measured as 43 μm. The unrecrystallised austenite structure comprised elongated grains and the effective grain boundary area per unit volume, S_v^{eff}, was measured as 116 mm^{-1}, which corresponds to an effective equiaxed grain size of approximately 17 μm. The room temperature microstructure of both samples consisted of primarily allotriomorphic ferrite.

The transformation from both austenite grain sizes was modelled and the volume fraction results are compared in Figure 10.17. The transformation from the fully recrystallised, equiaxed austenite grains was accurately predicted by the model. The results calculated assuming an equiaxed 17 μm grain size for the unrecrystallised structure correlated quite well with the experiments, although the kinetics of the transformation start were slightly under-estimated. Two improvements to the model were considered to cater for the deformed austenite. Firstly, a value for the stored energy due to the deformation, determined by CEIT as 2.6 $\times 10^6$ J m^{-3} [147] by the method of [136], was added to the overall free energy change for the austenite/ ferrite transformation, as described in Section 10.2. Secondly, the fraction of active nucleation sites was increased by factors of 10, 100 and 1000. Figure 10.17b shows that including the stored energy and increasing K_1^f by a factor of 100 to 10^{-7} produced an excellent fit with the experimental data, reproducing both the correct volume fractions and the transformation start temperature.

The final volume fraction of allotriomorphic ferrite formed as a function of S_v from deformed austenite was measured by CEIT on steel BS1 and Kozasu on a 0.03 Nb wt.% steel (Table 10.2). Figure 10.18 shows the calculations for the CEIT data at cooling rates of 1 and 5 °C s^{-1}. Without any adjustment for the stored energy, the model fitted the data quite well, although the amount of ferrite at 1 °C s^{-1} was under-estimated at low S_v values. Including the stored energy and fraction of active sites that fitted the curve in Figure 10.17b had no significant effect on the final ferrite fraction. The results for Kozasu's data are compared in Figure 10.19. Again, the model predicted the volume fractions of ferrite formed from recrystallised austenite successfully, using $K_1^f = 1 \times 10^{-9}$. The effect of increasing the stored energy, W, is also shown and a value of 2×10^7 J m^{-3} was found to reproduce the unrecrystallised experimental results. Reductions of up to 70% were applied below the recrystallisation stop temperature in the experiments, but no data suitable for determining stored energy values were reported.

However, the effects of the stored energy and the fraction of active sites on the volume fraction and ferrite grain size cannot be properly combined. Increasing the stored energy affects the ferrite growth rate more strongly than the nucleation rate, leading to faster grain growth and a larger ferrite grain size than with no stored energy (Figure 10.20). On

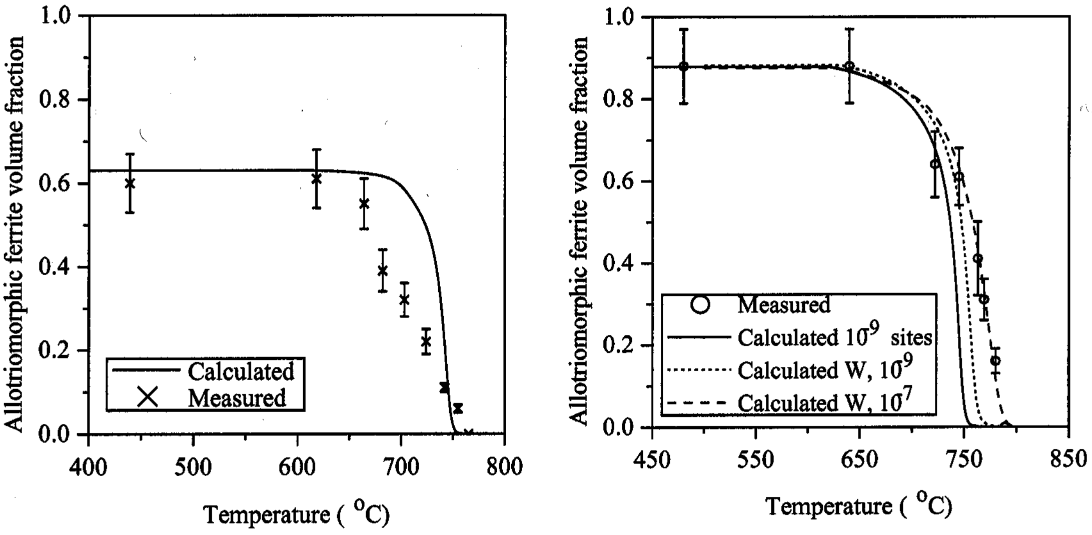

(a) (b)

Figure 10.17: Calculated evolution of allotriomorphic ferrite volume fraction in steel HO5 compared with experimental data of CEIT [147], cooled at 1 °C s^{-1} from (a) recrystallised austenite, (b) unrecrystallised austenite with stored energy $W = -2.6 \times 10^6$ and different K_1^f values. Error bars are 95% confidence limits.

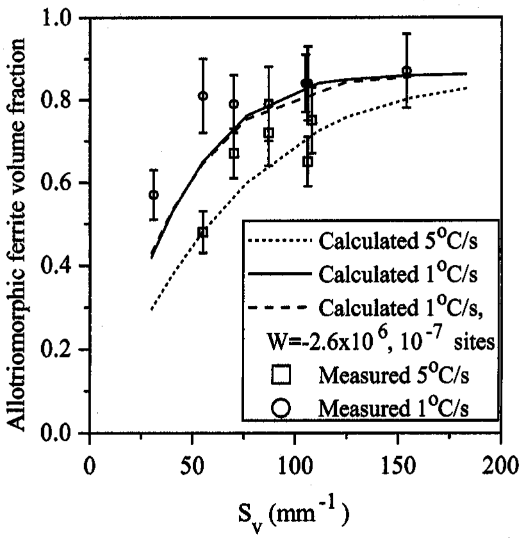

Figure 10.18: Calculated variation of allotriomorphic ferrite volume fraction as a function of S_v for steel BS1 cooled at 1 and 5 °C s^{-1}, compared with experimental data of CEIT [134]. Error bars are 95% confidence limits.

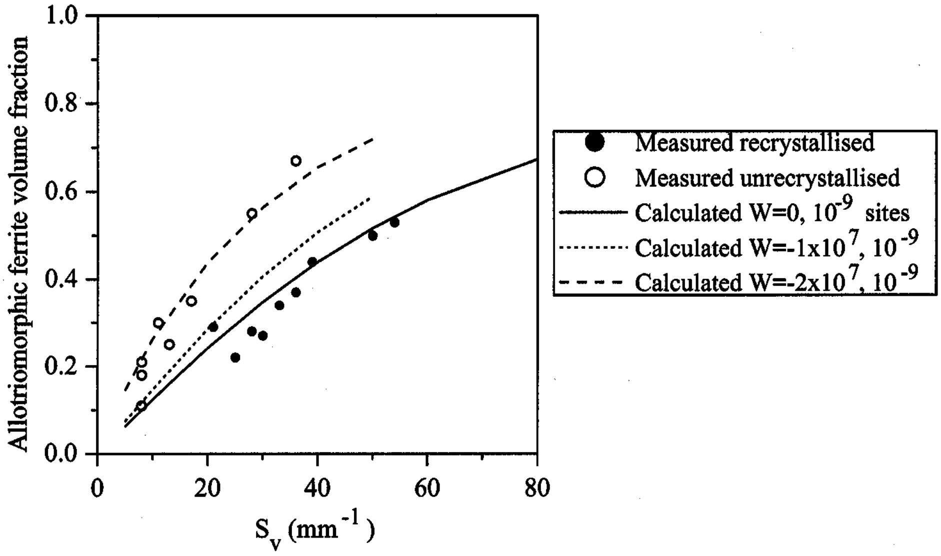

Figure 10.19: Calculated variation of allotriomorphic ferrite volume fraction as a function of S_v, showing effect of stored energy W and K_1^f on a 0.16 C wt.% steel cooled at 1 °C s^{-1}, compared with experimental data of Kozasu for recrystallised and unrecrystallised austenite [145].

the other hand, increasing K_1^f to refine the ferrite grain size does not have a major effect on the volume fraction, merely decreasing it by one or two percent (Figure 10.21). When both W and K_1^f are combined in the model the effect of the stored energy on the ferrite grain size swamps that of K_1^f. The volume fraction is increased successfully but the grain size is only partially refined.

10.5 Summary

The effects of deformation in the austenite phase field on the subsequent transformation to allotriomorphic ferrite have been reviewed. Three main factors were considered and incorporated into the transformation model.

Several methods of calculating the increase in austenite grain surface area per unit volume, S_v, were compared with experimental measurements. An equation based on the change in geometry of a spherical austenite grain as a function of rolling reduction was selected.

The magnitude of the stored strain energy of the unrecrystallised austenite calculated by two different methods was found to be sufficient to affect the driving force for the

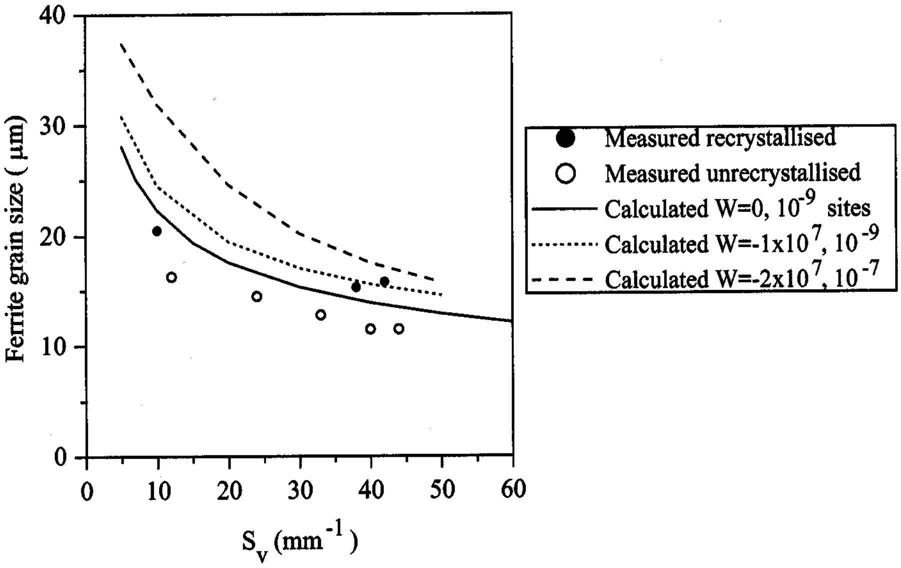

Figure 10.20: Calculated variation of ferrite grain size as a function of S_v, showing effect of stored energy and K_1^f on a 0.16 C wt.% steel cooled at 1 °C s^{-1}, compared with experimental data of Kozasu for recrystallised and unrecrystallised austenite [145].

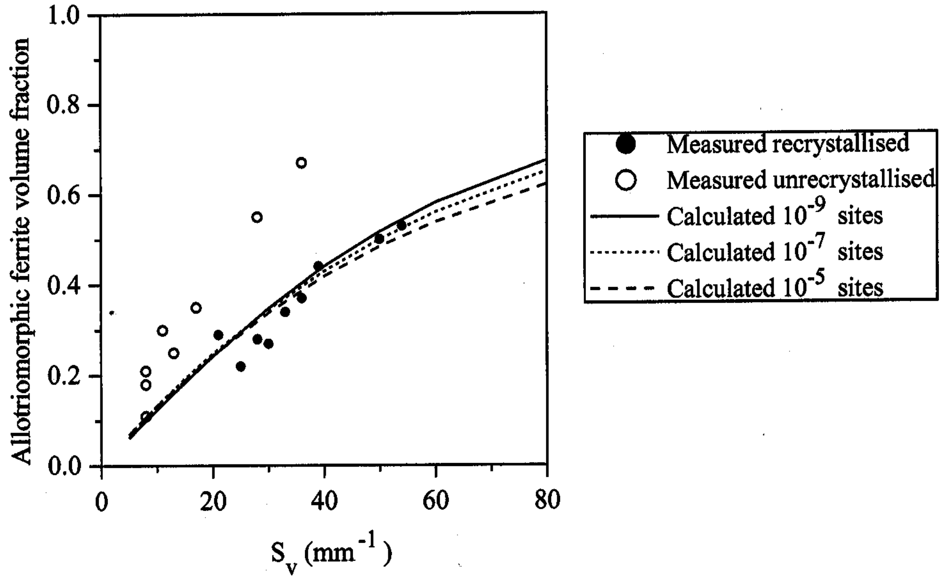

Figure 10.21: Calculated variation of allotriomorphic ferrite volume fraction as a function of S_v and K_1^f for a 0.16 C wt.% steel cooled at 1 °C s^{-1}, compared with experimental data of Kozasu for recrystallised and unrecrystallised austenite [145].

transformation in the model - of the order of $10^6 - 10^7$ J m^{-3}. As the stored energy increased, the growth rate, nucleation rate and volume fraction of allotriomorphic ferrite increased. However, the increase in growth kinetics tended to outweigh that of the nucleation kinetics and thus the ferrite grain size also increased, rather than being refined by the stored energy. The experimentally determined evolution of ferrite volume fraction during continuous cooling of deformed austenite was successfully modelled by addition of a stored energy value calculated from the maximum flow stress in the last deformation pass before cooling.

Mechanisms proposed in the literature to explain the observed increase in nuclei density at deformed austenite grain boundaries include 'bulges' in the boundary and dislocation sub-grains formed close to the boundary. In the model, the nucleation site density is altered by changing the fraction of active sites, K_1^f. Comparisons of measured allotriomorphic ferrite grain size and volume fraction data were made between recrystallised and unrecrystallised austenite over a wide range of S_v values. The ferrite grain size formed from recrystallised austenite could be correctly calculated with $K_1^f = 1 \times 10^{-9}$. An increase in active sites in the unrecrystallised austenite of between 1000 to 10,000 times ($K_1^f = 10^{-6} - 10^{-5}$) was found to refine the ferrite grain size sufficiently to agree with several sets of published data. However, contradictory experimental data which show no distinction between ferrite grain sizes from recrystallised and unrecrystallised austenite indicate that further verification of the magnitude of the increase in nuclei density is required. The contribution of microalloying elements such as Nb, V and Ti to the transformation kinetics were not included in this analysis and further work to investigate their effects on the model should be undertaken.

The transformation model can always reproduce the correct trends and there is good qualitative agreement between calculations and experiment, although some of the parameters have to be chosen arbitrarily.

Chapter 11

Conclusions and Suggestions for Further Work

The phase transformations that occur during the decomposition of hot-rolled austenite have been mathematically modelled based on the underlying thermodynamic and kinetic metallurgical theory. A quasichemical solution model was used to determine the paraequilibrium phase diagram and driving forces for the reconstructive and displacive transformations. Classical nucleation at several austenite grain boundary sites and diffusion-controlled growth were applied for allotriomorphic ferrite and pearlite. Displacive nucleation criteria were used for Widmanstätten ferrite and bainite; the former requiring carbon diffusion for growth, the latter being diffusionless.

The formation of allotriomorphic ferrite, Widmanstätten ferrite, pearlite, bainite and martensite can occur competitively and concurrently, but previous work has tended to consider only sequential reactions. A new model to calculate the overall, simultaneous transformation kinetics under isothermal and continuous cooling conditions for the five phases has been developed. The number of empirical parameters in the calculations has been minimised and a set of parameters for classical nucleation kinetics applicable to a wide range of steels has been determined.

The model has been validated using published and new experimental data with particular emphasis on the allotriomorphic ferrite, Widmanstätten ferrite and pearlite transformations. Allotriomorphic ferrite grain sizes and the volume fractions of each phase were compared against theory. Very good agreement was obtained at small and large austenite grain sizes. However, an imbalance in the computed proportions of allotriomorphic ferrite and Widmanstätten ferrite at intermediate austenite grain sizes was noted and this requires further investigation. The under-estimation of allotriomorphic ferrite then leads to a corresponding over-estimation of Widmanstätten ferrite.

A model for bainite kinetics has been separately verified and then incorporated into the overall scheme. Further verification of this model under the fast cooling rates that generate bainite in high strength low alloy steels and of the competition between the pearlite and bainite reactions is required.

Thermomechanical simulation experiments were carried out on a low alloy steel to provide test data for the model. Quantitative metallographic data were obtained for combinations of three austenite grain sizes and three cooling rates. As expected, the amount of allotriomorphic ferrite increased and Widmanstätten ferrite decreased as the austenite grain size and/or cooling rate was reduced.

The transformation of unrecrystallised austenite to allotriomorphic ferrite has been incorporated partially into the model. The surface area per unit volume of the deformed austenite grains was calculated as a function of rolling reduction based on the grain geometry. The calculated variation of ferrite grain size and volume fraction with S_v was compared with experimental results from the literature. Good qualitative agreement was obtained, although the stored energy and nucleation site density parameters had to be chosen arbitrarily.

There is plenty of scope for the further development of the transformation model, in addition to the immediate improvements mentioned above. Verification with additional sets of reliable experimental data obtained from a wider variety of steel compositions and processing conditions is always valuable. Extension to higher carbon grades would require a model for cementite formation and other carbides. The effects of microalloying elements such as Nb and Ti on the thermodynamics and kinetics could be included, enabling proper application to microalloyed steels which are of great commercial importance. Theory for the precipitation kinetics of nitrides and carbo-nitrides in the austenite and their effect on transformation could be coupled with the transformation model. The effects of austenite deformation on the displacive phase transformations could be incorporated.

An ultimate aim would be to develop a complete model of the hot-rolling process, linking together calculations of the austenite deformation, recovery and recrystallisation processes during rolling with the subsequent transformations after rolling is finished. Finite element techniques can compute the distribution of temperature and strain in the steel stock during the hot-rolling process. Instead of assuming a homogeneous austenite structure throughout the stock, the phase transformation model could then be applied to each element to obtain a more realistic prediction of the microstructure of the final product.

Appendix A

FORTRAN Subroutines

The phase transformation model described in this thesis is implemented in FORTRAN 77. The source code is portable and can be compiled in a variety of operating environments. The FORTRAN code for the main simultaneous transformation subroutine, the classical and displacive nucleation rate equations, and for calculating the Widmanstätten ferrite and bainite transformation start temperatures is provided in this Appendix.

A.1 Simultaneous Transformation Kinetics – VOLSIMGB

```
C S.V. Parker 22/7/97 Swinden Technology Centre, British Steel plc/Phase
C Transformations Group, Materials Science Dept., University of Cambridge
C Simultaneous Transformation routine to calculate volume fractions
C assuming boundary nucleation for all phases.
C Letter at end of variable name indicates which phase it concerns
C Phase A = allotriomorphic ferrite
C Phase B = Widmanstatten ferrrite
C Phase C = pearlite
C Phase D = bainite

      SUBROUTINE VOLSIMGB(VTOTAL,VA,VB,VC,VD,AREATOTAL,AREASIMA,AREASIMB,
     &AREASIMC,AREASIMD,VFERRITE,DALPHA,NUMPARTICLES,
     &ALP1,BI,VMAX,WI,VELPEARL,PEARLI,BAINI,
     &DT,TIME,SV,I,KTEMP,XBARN,BSGROW,THETA)
      IMPLICIT REAL*8(A-H,K-Z),INTEGER(I,J)
      DOUBLE PRECISION EXDSA,EXDSB,EXDSC,EXDSD,DSA,DSB,DSC,DSD
      DOUBLE PRECISION VTOTAL,VFERRITE,VA,VB,VC,VD,ALPA,ALPB,ALPC
      DOUBLE PRECISION BIA(10000),BIB(10000),BIC(10000),BID(10000)
      DOUBLE PRECISION Y(10000),SA(10000),SB(10000),SC(10000),SD(10000)
      DOUBLE PRECISION WIDTHB(10000),HEIGHTA(10000),OLDHEIGHTA(10000)
      DOUBLE PRECISION RADIUSA(10000),HEIGHTB(10000),OLDHEIGHTB(10000)
      DOUBLE PRECISION STOTAL(10000),OLDSA(10000),OLDSB(10000)
      DOUBLE PRECISION RADIUSC(10000),OLDSC(10000),OLDHEIGHTC(10000)
      DOUBLE PRECISION PARTICLESUMA(10000),DALPHA,NOPARTD(10000)
      DOUBLE PRECISION NOPARTA(10000),NOPARTB(10000),NOPARTC(10000)
```

```
      DOUBLE PRECISION TSINCENUCA(10000),TSINCENUCB(10000),TSINCENUCC(10000)
      DOUBLE PRECISION OLDSD(10000),DVOLD,OLDVOLD,TSINCENUCD(10000)
      DOUBLE PRECISION HEIGHTD(10000),OLDHEIGHTD(10000),HEIGHTC(10000)

C Reset variables for each new cooling rate
      IF (I .EQ. 1) THEN
            EXDSA=0.0
            EXDSB=0.0
            EXDSC=0.0
            EXDSD=0.0
            DO 7, IY=1,OLDIYMAX,1
                  SA(IY)=0.0
                  SB(IY)=0.0
                  SC(IY)=0.0
                  SD(IY)=0.0
7           CONTINUE
      ENDIF

C austenite grain size (m)
      DGAMMA=2.0/SV
C total volume of system
      V=1.0
C total grain boundary surface area (per unit volume)
      S=1.0D+00
C Widmanstatten plate thickening:lengthening ratio
      BETAWID=0.05
C equilibrium or maximum fractions of each phase set to 1.0
C with exception of bainite, which is limited by To line
      OMEGA=1.0
      OMEGA50=1.0
      OMEGAP=1.0
C growth rates
      ALPA=ALP1
      ALPB=VMAX
      ALPC=VELPEARL
      ALPD=1D-05
C nucleation rates per unit area
      BIA(I)=BI
      BIB(I)=WI
      BIC(I)=PEARLI
C Bainite autocatalysis parameters (see Rees & Bhadeshia, 1992)
      LAMBDA1=147.50D+00
      LAMBDA2=30.327d+00
      BETA=LAMBDA1*(1.0D+00-LAMBDA2*XBARN)
C Prevent BETA becoming negative and producing negative areas 6/12/96
      IF (BETA .LT. 0.0D+00) BETA=0.0D+00
      BID(I)=BAINI

C YSTEP is the distance between Y-planes parallel to g.b.
C varied to reduce computation time
      YSTEP1=1.0D-08
      YSTEP2=1.0D-07
      YSTEP3=1.0D-06
      YSTEP4=1.0D-05
```

```
C YMAX is the maximum distance a particle nucleated at t=0 has grown in
C the total transformation time. Compare maximums for each phase.
      IF (I .EQ. 1) THEN
            YAMAX=ALPA*DT**0.5
            YBMAX=ALPB*DT
            YCMAX=ALPC*DT
            YDMAX=ALPD*DT
      ELSE
            YAMAX=YAMAX+(0.5*ALPA*DT/(TIME)**0.5)
            YBMAX=YBMAX+(ALPB*DT)
            YCMAX=YCMAX+(ALPC*DT)
            YDMAX=YDMAX+(ALPD*DT)
      ENDIF
      IF (YBMAX .GE. YAMAX) THEN
            YMAX=YBMAX
      ELSE
            YMAX=YAMAX
      ENDIF
      IF (YCMAX .GE. YMAX) YMAX=YCMAX
      IF (YDMAX .GE. YMAX) YMAX=YDMAX
      IF (YMAX .LE. 10.0D-06) THEN
            IYMAX1=DABS(YMAX/YSTEP1)+1
            YMAX1=YMAX
      ELSEIF (YMAX .LE. 100D-06) THEN
            IYMAX2=DABS((YMAX-YMAX1)/YSTEP2)+1
            YMAX2=YMAX
      ELSEIF (YMAX .LE. 1000D-06) THEN
            IYMAX3=DABS((YMAX-YMAX2)/YSTEP3)+1
            YMAX3=YMAX
      ELSE
            IYMAX4=DABS((YMAX-YMAX3)/YSTEP4)+1
            YMAX4=YMAX
      ENDIF
      IYMAX=IYMAX1+IYMAX2+IYMAX3+IYMAX4
C IYMAX is the number of planes used to calculate extended area. It
C increases with time. YMAX is divided into different step sizes
C to help speed up calculation and improve accuracy.

C Store number of particles nucleated in current time interval
      NOPARTA(I)=S*BIA(I)*DT
      NOPARTB(I)=S*BIB(I)*DT
      NOPARTC(I)=S*BIC(I)*DT
      NOPARTD(I)=S*BID(I)*DT
C Store time since each set of particles nucleated
C This would be (I-J)*DT for a constant DT
      TSINCENUCA(I)=0.0
      TSINCENUCB(I)=0.0
      TSINCENUCC(I)=0.0
      TSINCENUCD(I)=0.0
      DO 5, J=1, I-1, 1
            TSINCENUCA(J)=TSINCENUCA(J)+DT
            TSINCENUCB(J)=TSINCENUCB(J)+DT
            TSINCENUCC(J)=TSINCENUCC(J)+DT
            TSINCENUCD(J)=TSINCENUCD(J)+DT
```

```
5     CONTINUE

C For each incubation time, tau (J)
      DO 3, J=1,I,1
C HEIGHT(J) is current height above boundary of particle nucleated after
C incubation time corresponding to J
            IF (J .EQ. I) THEN
            OLDHEIGHTA(J)=0.0
            OLDHEIGHTB(J)=0.0
            OLDHEIGHTC(J)=0.0
            OLDHEIGHTD(J)=0.0
            HEIGHTA(J)=ALPA*DT**0.5
            HEIGHTB(J)=ALPB*DT
            HEIGHTC(J)=ALPC*DT
                  IF (BID(I) .GT. 0.0) THEN
                  HEIGHTD(J)=ALPD*DT
                  ELSE
                  HEIGHTD(J)=0.0D+00
                  ENDIF
            ELSE
C Add on growth in current time interval to total growth
            OLDHEIGHTA(J)=HEIGHTA(J)
            OLDHEIGHTB(J)=HEIGHTB(J)
            OLDHEIGHTC(J)=HEIGHTC(J)
            OLDHEIGHTD(J)=HEIGHTD(J)
            HEIGHTA(J)=HEIGHTA(J)+(0.5*ALPA*DT/(TSINCENUCA(J))**0.5)
            HEIGHTB(J)=HEIGHTB(J)+(ALPB*DT)
            HEIGHTC(J)=HEIGHTC(J)+(ALPC*DT)
C Only increase max possible height of bainite if growth flag set
                  IF (BSGROW.EQ.1.0) THEN
                  HEIGHTD(J)=HEIGHTD(J)+(ALPD*DT)
                  ENDIF
            ENDIF
            RADIUSA(J)=3*HEIGHTA(J)
            WIDTHB(J)=HEIGHTB(J)*BETAWID
            RADIUSC(J)=1.0*HEIGHTC(J)
C Restrict Wid plate length to be no greater than austenite grain size
            IF (HEIGHTB(J) .GT. DGAMMA) HEIGHTB(J)=DGAMMA
3     CONTINUE

C Y(IY) is the distance of the IY-th plane from the boundary
      DO 2, IY=1,IYMAX,1
            IF (IY .LE. IYMAX1) THEN
                  Y(IY)=(IY-1)*YSTEP1
            ELSEIF (IY .LE. (IYMAX1+IYMAX2)) THEN
                  Y(IY)=Y(IYMAX1)+((IY-IYMAX1)*YSTEP2)
            ELSEIF (IY .LE. (IYMAX1+IYMAX2+IYMAX3)) THEN
                  Y(IY)=Y(IYMAX1+IYMAX2)+((IY-IYMAX1-IYMAX2)
     &            *YSTEP3)
            ELSE
                  Y(IY)=Y(IYMAX1+IYMAX2+IYMAX3)+
     &            ((IY-IYMAX1-IYMAX2-IYMAX3)*YSTEP4)
            ENDIF
```

```
C Reset change in extended area of each phase
            EXDSA=0.0
            EXDSB=0.0
            EXDSC=0.0
            EXDSD=0.0
C calculate change in extended area in current time step due to growth
C of previously nucleated particles, using corresponding nucleation rate
C but current growth rate

            DO 1, J=1,I,1
C Ex. area added only if particle reaches plane at distance Y from boundary.

C Allotriomorphic ferrite -- parabolic growth of discs
            IF (HEIGHTA(J) .GE. Y(IY)) THEN
C           Disc has reached plane at Y
                  IF ((OLDHEIGHTA(J) .LT. Y(IY)) .OR.
     &            (OLDHEIGHTA(J) .EQ. 0.0)) THEN
C  Disc first reached Y in current time interval so all its area
C  contributes to change in ex. area
                  EXDSA=EXDSA+NOPARTA(J)*3.14159*(RADIUSA(J)**2)
                  ELSE
C  Disc reached Y previously, so only growth in the plane
C  contributes to change in ex. area
                  EXDSA=EXDSA+NOPARTA(J)*3.14159*DT*(3*ALPA)**2
                  ENDIF
            ENDIF

C Widmanstatten ferrite -- linear growth of plates
            IF (HEIGHTB(J) .GE. Y(IY)) THEN
C  Plate has reached plane at Y
                  IF (OLDHEIGHTB(J) .LT. Y(IY)) THEN
c     &           (OLDHEIGHTB(J) .EQ. 0.0)) THEN
C  Plate first reached Y in current time interval so all its area
C  contributes to change in ex. area
                  EXDSB=EXDSB+NOPARTB(J)*WIDTHB(J)*HEIGHTB(J)
                  ELSE
C  PLate reached Y previously, so only growth in the plane
C  contributes to change in ex. area
                  EXDSB=EXDSB+NOPARTB(J)*2*BETAWID*ALPB**2*TSINCENUCB(J)*DT
                  ENDIF
            ENDIF

C Pearlite -- linear growth of hemispheres
            IF (HEIGHTC(J) .GE. Y(IY)) THEN
C  Hemisphere has reached plane at Y
                  IF (OLDHEIGHTC(J) .LT. Y(IY)) THEN
C  Hemisphere first reached Y in current time interval so all its area
C  contributes to change in ex. area
                  EXDSC=EXDSC+NOPARTC(J)*3.14159*(RADIUSC(J)**2-Y(IY)**2)
                  ELSE
C  Hemisphere reached Y previously, so only growth in the plane
C  contributes to change in ex. area
                  EXDSC=EXDSC+NOPARTC(J)*2.0*3.14159*(1*ALPC)**2*DT
     &            *TSINCENUCC(J)
```

```
                 ENDIF
            ENDIF

C Bainite plate size temperature dependence
            USCALAR=(KTEMP-528)/150
C fix a lower limit on plate width at 300 degrees C
            IF (USCALAR .LT. 0.3) USCALAR=0.3
            WIDTHD=0.2D-06*USCALAR
            LENGTHD=1.0D-05
            IF ((HEIGHTD(J) .GE. Y(IY)) ) THEN
                  IF ((OLDHEIGHTD(J) .LT. Y(IY)) .OR.
     &            (OLDHEIGHTD(J) .EQ. 0.0)) THEN
C Bainite sheaf first reached Y in current time interval so all its area
C contributes to change in extended area
                  EXDSD=EXDSD+WIDTHD*LENGTHD*NOPARTD(J)
                  ELSE
C no growth in the plane
                  ENDIF
            ENDIF

1           CONTINUE

C Convert changes in ex. area into changes in real area
            IF (I .EQ. 1) THEN
                  DSA=EXDSA
                  DSB=EXDSB
                  DSC=EXDSC
                  DSD=EXDSD
            ELSE
                  IF (STOTAL(IY)/S .GE. 1.0) THEN
                  SUNTRANS=0.0
                  ELSE
                  SUNTRANS=1.0-(STOTAL(IY)/S)
                  ENDIF
C actual change in area is change in extended area modified by fraction of
C total area still untransformed SUNTRANS
                  DSA=EXDSA*SUNTRANS
                  DSB=EXDSB*SUNTRANS
                  DSC=EXDSC*SUNTRANS
                  DSD=EXDSD*SUNTRANS
            ENDIF
C Sum to find total actual area transformed on IY-th plane for each phase
            IF (I .EQ. 1) THEN
                  SA(IY)=DSA
                  SB(IY)=DSB
                  SC(IY)=DSC
                  SD(IY)=DSD
            ELSE
                  SA(IY)=SA(IY)+DSA
                  SB(IY)=SB(IY)+DSB
                  SC(IY)=SC(IY)+DSC
                  SD(IY)=SD(IY)+DSD
            ENDIF
C Calculation of no. of ferrite particles on boundary plane (Y=0, IY=1)
```

```
            IF (SA(1) .GT. 0.9999*S) THEN
                  BBIA=BIA(I)*S/SA(1)
            ELSE
                  BBIA=BIA(I)
            ENDIF
            IF (I .EQ. 1) THEN
                  PARTICLESUMA(I)=BBIA*DT*S
            ELSE
                  PARTICLESUMA(I)=PARTICLESUMA(I-1)+(BBIA*DT*(S-STOTAL(1)))
            ENDIF
C Prevent area of each phase exceeding total area of plane
      IF ((SA(IY) .GT. S)) SA(IY)=S
      IF ((SB(IY) .GT. S)) SB(IY)=S
      IF ((SC(IY) .GT. S)) SC(IY)=S
      IF ((SD(IY) .GT. S)) SD(IY)=S
C Prevent combined areas of phases exceeding total area of plane
      IF (SA(IY)+SB(IY) .GT. S) THEN
C modified again 22/10/96 due to problems with VA decreasing
      IF ((OLDSA(IY)+OLDSB(IY)) .GT. 0.9995D+00*S) THEN
            SA(IY)=OLDSA(IY)
            SB(IY)=OLDSB(IY)
      ELSE
            SPARE=SA(IY)+SB(IY)-S
            PROPA=SA(IY)/(SA(IY)+SB(IY))
            PROPB=SB(IY)/(SA(IY)+SB(IY))
            SPAREA=SPARE*PROPA
            SPAREB=SPARE*PROPB
            SA(IY)=SA(IY)-SPAREA
            SB(IY)=SB(IY)-SPAREB
      ENDIF
      ENDIF
C Calculate total area of all phases on the IY-th plane
      STOTAL(IY)=SA(IY)+SB(IY)+SC(IY)+SD(IY)
      OLDSA(IY)=SA(IY)
      OLDSB(IY)=SB(IY)
      OLDSC(IY)=SC(IY)
      OLDSD(IY)=SD(IY)
      IF (STOTAL(IY) .GT. S) STOTAL(IY)=S

2     CONTINUE

C AREASIM is the fraction of g.b. area covered
      AREASIMA=SA(1)
      AREASIMB=SB(1)
      AREASIMC=SC(1)
      AREASIMD=SD(1)
      AREATOTAL=AREASIMA+AREASIMB+AREASIMC+AREASIMD
C calculate total ex. volume for all planes Y from 0 to YMAX by
C integration of areas (SA) over Y
      CALL TRAPE(Y,SA,ANSA,IYMAX)
      CALL TRAPE(Y,SB,ANSB,IYMAX)
      CALL TRAPE(Y,SC,ANSC,IYMAX)
      CALL TRAPE(Y,SD,ANSD,IYMAX)
      EXVA=2*ANSA*SV
```

```
      EXVB=ANSB*SV
      EXVC=ANSC*SV
      EXVD=ANSD*SV

      IF (I .EQ. 1) THEN
            EXDVA=EXVA
            EXDVB=EXVB
            EXDVC=EXVC
            EXDVD=EXVD
            DVA=EXDVA
            DVB=EXDVB
            DVC=EXDVC
            DVD=EXDVD
C Normalise with equilibrium volume fractions of each phase
C These are set to 1.0 so not actually used
            DVOLA=DVA/OMEGA
            DVOLB=DVB/OMEGA50
            DVOLC=DVC/OMEGAP
            DVOLD=DVD/THETA
            VA=DVA
            VB=DVB
            VC=DVC
            VD=DVD
            VOLA=DVOLA
            VOLB=DVOLB
            VOLC=DVOLC
            VOLD=DVOLD
      ELSE
C convert change in extended volume to real volume using total
C untransformed volume VUNTRANS
            EXDVA=EXVA-OLDEXVA
            EXDVB=EXVB-OLDEXVB
            EXDVC=EXVC-OLDEXVC
            EXDVD=EXVD-OLDEXVD
            DVA=EXDVA*VUNTRANS
            DVB=EXDVB*VUNTRANS
            DVC=EXDVC*VUNTRANS
            DVD=EXDVD*VUNTRANS
C Normalise with equilibrium volume fractions of each phase
C These are set to 1.0 so not actually used
            DVOLA=DVA/OMEGA
            DVOLB=DVB/OMEGA50
            DVOLC=DVC/OMEGAP
            DVOLD=DVD/THETA
C Sum total actual volumes of each phase
            VA=OLDVA+DVA
            VB=OLDVB+DVB
            VC=OLDVC+DVC
            VD=OLDVD+DVD
C Sum total normalised volume fractions
            VOLA=OLDVOLA+DVOLA
            VOLB=OLDVOLB+DVOLB
            VOLC=OLDVOLC+DVOLC
            VOLD=OLDVOLD+DVOLD
```

```
      ENDIF

C Total volume transformed
      VTOTAL=VA+VB+VC+VD+VA3
C Prevent total volume exceeding 1.0
      IF (VTOTAL .GE. 1.0D+00) THEN
            IF (((VA+VB+VD).GT.0.5).AND.(VC.GT.(1.0D+00-VA-VB-VD)))
     &            VC=1.0D+00-VA-VB-VD
      ENDIF
      IF (VTOTAL .GT. 1.00D+00) VTOTAL=1.00D+00
C Remaining untransformed volume
      VUNTRANS=1.0D+00-VTOTAL
C Total volume of ferritic products (used to calc austenite enrichment)
      VFERRITE=VA+VB+VD

C Calculate ferrite grain size from total number of g.b. particles
      IF (PARTICLESUMA(I).GT.1.0D4) THEN
            DALPHA=(2.0/(3.0*SV*PARTICLESUMA(I)))**0.333D+00
            DALPHA=DALPHA*1.0D+06
            NUMPARTICLES=PARTICLESUMA(I)
      ENDIF

C Store current values needed for next iteration
      OLDEXVA=EXVA
      OLDEXVB=EXVB
      OLDEXVC=EXVC
      OLDEXVD=EXVD
      OLDVA=VA
      OLDVB=VB
      OLDVC=VC
      OLDVD=VD
      OLDVOLA=VOLA
      IF (OLDVOLA.GT.1.0D+00) OLDVOLA=1.0D+00
      OLDVOLB=VOLB
      OLDVOLC=VOLC
      IF (OLDVOLC.GT.1.0D+00) OLDVOLC=1.0D+00
      OLDVOLD=VOLD
      OLDIYMAX=IYMAX

      RETURN
      END
```

A.2 Nucleation Rate of Allotriomorphic Ferrite – NUC

```
C Nucleation rate of allotriomorphic ferrite per unit g.b. area
C Final version for thesis and MAP  23/7/97
C S.V. Parker and H.K.D.H. Bhadeshia
C KTEMP = absolute temperature (K)
C Q = activation energy for self-diffusion of iron (J)
C GSTAR = activation energy for grain boundary nucleation (J)
C BI = grain boundary nucleation rate per unit area (m^2s^-1)
C GV = Gibbs free energy change per unit volume, for nucleation (J/m^3)
C SIGMA = matrix/nucleus interfacial energy per unit area (J/m^2)
C SITE = fraction of active nucleation sites
C AA = atomic spacing (m)
C DGAMMA = austenite grain size (m)
C SV = austenite grain surface area per unit volume (m^-1)

      SUBROUTINE NUC(SITE,GSTAR,KTEMP,GV,SV,BI,BIFACE,BIEDGE,BICORN)
      IMPLICIT REAL*8(A-H,K-Z), INTEGER(I,J)
      DOUBLE PRECISION AA,AV,BOLTZ,BI,BIFACE,BIEDGE,BICORN,DGAMMA
      DOUBLE PRECISION GSTAR,GV,HH,KTEMP,KF,KE,KC,Q,SIGMA
      DOUBLE PRECISION SITE,SITEF,SITEE,SITEC,SV
      DOUBLE PRECISION ARGF,ARGE,ARGC
      AV=6.02217D+23
      BOLTZ=1.38062D-23
      HH=6.6262D-34
      DGAMMA=2.0/SV
      AA=2.5D-10
      SIGMA=0.05D+00
      Q=2.4D+05/AV
C shape factors for face (F), edge (E) and corner (C) nucleation sites
      KF=0.1
      KE=0.01
      KC=0.001
      GSTAR=SIGMA**3.0D+00/(GV**2)
C density of sites at faces, edges, corners (J.W. Christian, The Theory of
C Phase Transformations in Metals and Alloys, Part 1, 2nd ed., Pergamon,
C Oxford, 1965, 455)
      SITEF=SITE/(2*AA*AA)
      SITEE=SITE/(2*AA*DGAMMA)
      SITEC=SITE/(2*DGAMMA*DGAMMA)
C modify interfacial energy (via G*) with shape factors
      ARGF=((GSTAR*KF)+Q)/(BOLTZ*KTEMP)
      ARGE=((GSTAR*KE)+Q)/(BOLTZ*KTEMP)
      ARGC=((GSTAR*KC)+Q)/(BOLTZ*KTEMP)
C nucleation rate for each type of site
      BIFACE=(BOLTZ*KTEMP/HH)*DEXP(-ARGF)*SITEF
      BIEDGE=(BOLTZ*KTEMP/HH)*DEXP(-ARGE)*SITEE
      BICORN=(BOLTZ*KTEMP/HH)*DEXP(-ARGC)*SITEC
C Total nucleation rate is sum of face, edge and corner contributions
      BI=(BIFACE+BIEDGE+BICORN)
2     RETURN
      END
```

A.3 Displacive Nucleation Rate – WIDNUC

```
C Subroutine to calculate displacive nucleation rate per unit area
C Based on Rees and Bhadeshia, Mat. Sci. Tech., 1992, 985-993
C Final version for thesis and MAP 23/7/97   S.V. Parker

      SUBROUTINE WIDNUC3(WI,KTEMP,GMAX,SV)
      IMPLICIT REAL*8(A-H,K-Z), INTEGER(I,J)
      DOUBLE PRECISION ARG,K1,K1PRIME,K2,WI,WIVOL,WIAREA
      DOUBLE PRECISION SV,DGAMMA,U
C K1 is density of available nucleation sites
C AA is atomic spacing (m)
C KTEMP is absolute temperature (K)
C SV is austenite grain surface area per unit volume (m^-1)
C DGAMMA is austenite grain size (m)
C K2, K1PRIME are constants derived by Rees
C R is universal molar gas constant
C WIVOL is nucleation rate per unit volume (m^-3 s^-1)
C WIAREA is nucleation rate per unit area (m^-2 s^-1)
      AA=2.5D-10
      K2=2.098D+04
      R=8.31432D+00
      DGAMMA=2.0/SV
C U is volume of bainitic sub-unit
      U=1.0D-05*1.0D-05*0.2D-06
C K1PRIME from Rees and Bhadeshia
      K1PRIME=U*34.456D+06
      K1=1.0/(DGAMMA*K1PRIME)
      ARG=(K2/(R*KTEMP))*(1.0D+00 + (GMAX/2540.0D+00))
      WIVOL=K1*DEXP(-ARG)
C convert to nucln rate per unit area
      WIAREA=WIVOL/SV
      WI=WIAREA
      RETURN
      END
```

A.4 Widmanstätten Ferrite and Bainite Start Temperatures – WIDSTART

```
C Widmanstatten and bainite start temperature routine
C Final version for thesis and MAP 23/7/97  S.V. Parker
      SUBROUTINE WIDSTART(WS,BS,CTEMP,GMAX,FPRO,FTO,IWSNUC,IWSGROW,
     & IWSFLAG,IBSGROW,IBSFLAG)
      IMPLICIT REAL*8(A-H,K-Z), INTEGER(I,J)
      DOUBLE PRECISION CTEMP,F1,F2,FPRO,FTO,GMAX,GN,WS,BS
      INTEGER IWSNUC,IWSGROW,IWSFLAG,IBSGROW,IBSFLAG
C WS is the Widmanstatten ferrite start temp in Centigrade
C BS is the bainite start temperature in Centigrade
C GN is the Universal Nucleation function in J/mol
C GMAX is the driving force for ferrite nucleation
C FPRO is the driving force for reconstructive austenite-ferrite transfn
C FTO is the driving force for diffusionless austenite-ferrite transfn
C F1 is the stored energy for Wid ferrite growth in J/mol
C F2 is the stored energy for bainite growth in J/mo
C IWSNUC is a flag indicating if Wid nucleation is possible
C IWSGROW is a flag indicating if Wid growth is possible
C IBSGROW is a flag indicating if bainite growth is possible
C Once bainite starts growing, Wid growth is stopped
C IWSFLAG is set once WS has been determined
C IBSFLAG is set once BS has been determined
      F1=-50.00D+00
      F2=-400.0D+00
      IWSNUC=0
      IWSGROW=0
      IBSGROW=0
      GN=3.637D+00*CTEMP - 2540.00D+00
      IF (GMAX .LE. GN) IWSNUC=1
      IF (FTO .LT. F2) THEN
            IBSGROW=1
            IWSGROW=0
      ELSEIF (FPRO .LT. F1) THEN
            IWSGROW=1
            IBSGROW=0
      ENDIF
C Criteria for nucleation and growth satisfied
      IF ((IWSFLAG .EQ. 0) .AND. (IWSNUC .EQ. 1) .AND.
     &(IWSGROW .EQ. 1) .AND. (IBSFLAG .EQ.0)) THEN
            WS=CTEMP
            IWSFLAG=1
            WRITE(*,2) WS
2           FORMAT(/20X,'Widmanstatten ferrite start temperature = ',
     &      F6.2,' C'/)
      ENDIF
      IF ((IBSFLAG .EQ. 0) .AND. (IWSNUC .EQ. 1) .AND.
     &(IBSGROW .EQ. 1)) THEN
            BS=CTEMP
            IBSFLAG=1
            WRITE(*,3) BS
3           FORMAT(/20X,'Bainite start temperature = ',
```

```
&      F6.2,' C'/)
 ENDIF
 RETURN
 END
```

Appendix B

MAP Documentation

The FORTRAN routines in the previous Appendix are documented in a format consistent with the Materials Algorithms Project (MAP) [148]. This is a perpetual FORTRAN library of complete programs and elementary subroutines and functions relevant to materials science and metallurgy. It enables other researchers to more readily use and understand the code, and incorporate individual routines into their programs. The MAP FORTRAN library is available at:

`http://www.msm.cam.ac.uk/map/mapmain.html`

B.1 Subroutine MAP_STEEL_VOLSIMGB

0. Provenance of Source Code

S.V. Parker, Swinden Technology Centre, British Steel plc, Moorgate, Rotherham, S60 3AR, U.K. and Phase Transformations Group, Department of Materials Science and Metallurgy, University of Cambridge, Cambridge, U.K.

1. Purpose

MAP_STEEL_VOLSIMGB calculates the volumes of allotriomorphic ferrite, Widmanstätten ferrite, pearlite and bainite formed simultaneously from austenite as a function of time and temperature in a low alloy steel. It can be called from within an isothermal or continuous cooling transformation program at each time step during the transformation.

2. Specification

SUBROUTINE MAP_STEEL_VOLSIMGB(VTOTAL,VA,VB,VC,VD,STOTAL,SA,

```
SB,SC,SD,VFERRITE,DALPHA,NUMPARTICLES,ALP1,BI,VMAX,WI,VELPEARL,
PEARLI,BAINI,DT,TIME,SV,I,KTEMP,XBARN,BSGROW,THETA)
DOUBLE PRECISION ALP1,BAINI,BI,BSGROW,DALPHA,DT,KTEMP
DOUBLE PRECISION NUMPARTICLES,PEARLI,SA,SB,SC,SD,STOTAL,SV
DOUBLE PRECISION THETA,TIME,VA,VB,VC,VD,VELPEARL,VFERRITE
DOUBLE PRECISION VMAX,VTOTAL,WI,XBARN

INTEGER I
```

3. Description

The subroutine uses an extension of the Johnson-Mehl-Avrami overall transformation kinetics theory which enables the simultaneous transformation of several phases to be modelled [1,2,3]. Nucleation and growth rate parameters for each phase are required as inputs to the routine. Heterogeneous nucleation at the austenite grain boundaries is considered for each phase. The allotriomorphic ferrite is modelled as discs thickening at a parabolic rate parallel to the boundary plane [4], Widmanstätten ferrite as plates growing into the austenite grain, pearlite as hemispherical particles and bainite as autocatalytically nucleated sub-units which form the bainite sheaves [5].

4. References

1. S. V. Parker, *Modelling of Phase Transformations in Hot-Rolled Steels*, Ph.D. Thesis, University of Cambridge, (1997).

2. S. J. Jones and H. K. D. H. Bhadeshia, *Acta Materialia*, **45**, (1997), 2911-2920.

3. J. D. Robson and H. K. D. H. Bhadeshia, *Mat. Sci. Tech.*, **13**, (1997), 631-639, 640-644

4. H. K. D. H. Bhadeshia, L.-E. Svensson and B. Gretoft, *Proc. Conf. on Welding Metallurgy of Structural Steels*, ed. J.Y. Koo, TMS-AIME, Warrendale, PA, (1987) 517-530

5. G. I. Rees and H. K. D. H. Bhadeshia, *Materials Science and Technology*, **8**, (1992), 985-993

5. Parameters

Input parameters

ALP1 - real

ALP1 is the one-dimensional rate constant for parabolic thickening of ferrite allotriomorphs ($\mathrm{m\,s^{-\frac{1}{2}}}$). It can be calculated with subroutine MAP_STEEL_ALLL.

BAINI - real

BAINI is the displacive nucleation rate of bainite per unit area of austenite grain boundary ($m^{-2}\ s^{-1}$).

BI -real

BI is the nucleation rate of allotriomorphic ferrite per unit area of austenite grain boundary ($m^{-2}\ s^{-1}$). It can be calculated with subroutine MAP_STEEL_NUC.

BSGROW - real

BSGROW is a flag indicating whether bainite growth is thermodynamically possible. BSGROW = 1.0 for growth, BSGROW = 0.0 for no growth.

DT - real

DT is the time step (s).

I - integer

I is an index corresponding to the current time step. It should be incremented by an external program each time it calls MAP_STEEL_VOLSIMGB, so that the data on each phase stored within the subroutines' arrays at a particular transformation time or incubation time can be referenced.

KTEMP - real

KTEMP is the absolute temperature (K).

PEARLI - real

PEARLI is the nucleation rate of pearlite per unit area of austenite grain boundary ($m^{-2}\ s^{-1}$).

SV - real

SV is the austenite grain surface area per unit volume (m^{-1}). It can be calculated from the austenite grain size, d_γ, as $\frac{2}{d_\gamma}$.

THETA - real

THETA is the maximum fraction of bainite that can form at the current temperature. It can be determined from the phase diagram using the T_o composition using subroutine MAP_STEEL_MV.

TIME - real

TIME is the total elapsed time since the start of the transformations (s)

VELPEARL - real

VELPEARL is the pearlite growth rate ($m\ s^{-1}$).

VMAX - real

VMAX is the lengthening rate of Widmanstätten ferrite plates ($m\ s^{-1}$). It can be calculated with the subroutine MAP_STEEL_VEL4.

WI - real

WI is the nucleation rate of Widmanstätten ferrite per unit area of austenite grain boundary ($\mathrm{m}^{-2}\ \mathrm{s}^{-1}$).

XBARN - real

XBARN is the average mole fraction of carbon in the untransformed austenite.

Output parameters

DALPHA - real

DALPHA is the allotriomorphic ferrite grain size in microns, calculated at the austenite grain boundary as: $d_\alpha = \frac{2}{3S_vN_s}$ where S_v is the austenite grain surface area per unit volume and N_s is the number of allotriomorphic ferrite particles per unit area of austenite boundary.

NUMPARTICLES - real

NUMPARTICLES is the number of allotriomorphic ferrite particles per unit area of austenite grain boundary.

SA - real

SA is the amount of austenite grain boundary area transformed to allotriomorphic ferrite.

SB - real

SB is the amount of austenite grain boundary area transformed to Widmanstätten ferrite.

SC - real

SC is the amount of austenite grain boundary area transformed to pearlite.

SD - real

SD is the amount of austenite grain boundary area transformed to bainite.

STOTAL - real

STOTAL is the total amount of austenite grain boundary area that has been transformed to all phases. STOTAL=SA+SB+SC+SD.

VA - real

VA is the volume of allotriomorphic ferrite formed.

VB - real

VB is the volume of Widmanstätten ferrite formed.

VC - real

VC is the volume of pearlite formed.

VD - real

VD is the volume of bainite formed.

VFERRITE - real

VFERRITE is the total volume of ferritic phases formed. VFERRITE = VA+VB+VD. It can be used to calculate the carbon enrichment of the austenite.

VTOTAL - real

VTOTAL is the total volume of all phases formed. VTOTAL = VA+VB+VC+VD.

6. Error Indicators

None

7. Accuracy

The choice of time step DT is important. The smaller the time step, the greater the accuracy of the area and volume calculations. Fast cooling rates and fast transformations (*e.g.* those with large growth rates such as Widmanstätten ferrite) require small time steps so that the amount of transformation in one step is not too large (less than 5%, probably smaller at the start of a transformation). DT=1 s would be typical for 1 °C s^{-1} cooling.

8. Further Comments

None

9. Example

To calculate the microstructure of a steel isothermally transformed at 700 °C for 50 seconds.

9.1 Program text

```
      DOUBLE PRECISION ALP1,BAINI,BI,BSGROW,DALPHA,DT,HOLDTIME,KTEMP
      DOUBLE PRECISION NUMPARTICLES,PEARLI,SA,SB,SC,SD,STOTAL,SV,THETA,TIME
      DOUBLE PRECISION VA,VB,VC,VD,VELPEARL,VFERRITE,VMAX,VTOTAL,WI,XBARN
      INTEGER I,IMAX
      READ(5,*) KTEMP,HOLDTIME,DT,SV,XBARN,BSGROW,THETA
      READ(5,*) ALP1,BI,VMAX,WI,VELPEARL,PEARLI,BAINI
      IMAX=DABS(HOLDTIME/DT)
      WRITE(6,2)
2     FORMAT(/'   TIME    VA     VB     VC     VD   VTOTAL   ',
     & 'DALPHA  PARTICLES '/)

      DO 1 I=1,IMAX
          TIME=I*DT
          CALL VOLSIMGB(VTOTAL,VA,VB,VC,VD,STOTAL,SA,
```

```
     &     SB,SC,SD,VFERRITE,DALPHA,NUMPARTICLES,
     &     ALP1,BI,VMAX,WI,VELPEARL,PEARLI,BAINI,
     &     DT,TIME,SV,I,KTEMP,XBARN,BSGROW,THETA)

           WRITE(6,3) TIME,VA,VB,VC,VD,VTOTAL,
     &     DALPHA,NUMPARTICLES
3          FORMAT(F6.1,5F7.3,F7.2,D11.3)

1       CONTINUE
        STOP
        END
```

9.2 Program data

```
973    50    1    1.0D+5    0.0046    0    1
0.2D-5    0.3D+8    0.4D-5    0.6D+8    0.0    0.0    0.0
```

9.3 Program results

```
 TIME   VA     VB      VC      VD    VTOTAL  DALPHA  PARTICLES

  1.0  0.001  0.000  0.000  0.000  0.001  61.16  0.300D+08
  2.0  0.006  0.000  0.000  0.000  0.006  48.64  0.597D+08
  3.0  0.013  0.001  0.000  0.000  0.014  42.57  0.891D+08
  4.0  0.025  0.002  0.000  0.000  0.027  38.76  0.118D+09
  5.0  0.041  0.004  0.000  0.000  0.045  36.07  0.146D+09
  6.0  0.062  0.007  0.000  0.000  0.069  34.04  0.174D+09
  7.0  0.087  0.011  0.000  0.000  0.097  32.44  0.201D+09
  8.0  0.115  0.016  0.000  0.000  0.131  31.14  0.228D+09
  9.0  0.147  0.022  0.000  0.000  0.169  30.06  0.253D+09
 10.0  0.182  0.029  0.000  0.000  0.210  29.16  0.278D+09
 11.0  0.218  0.037  0.000  0.000  0.255  28.38  0.301D+09
 12.0  0.256  0.046  0.000  0.000  0.302  27.71  0.323D+09
 13.0  0.294  0.055  0.000  0.000  0.350  27.13  0.344D+09
 14.0  0.332  0.066  0.000  0.000  0.398  26.63  0.364D+09
 15.0  0.370  0.076  0.000  0.000  0.446  26.19  0.383D+09
 16.0  0.405  0.087  0.000  0.000  0.492  25.80  0.401D+09
 17.0  0.439  0.098  0.000  0.000  0.537  25.46  0.417D+09
 18.0  0.471  0.109  0.000  0.000  0.579  25.16  0.432D+09
 19.0  0.500  0.119  0.000  0.000  0.619  24.90  0.446D+09
 20.0  0.526  0.129  0.000  0.000  0.655  24.67  0.458D+09
 21.0  0.550  0.139  0.000  0.000  0.689  24.47  0.470D+09
 22.0  0.572  0.148  0.000  0.000  0.720  24.29  0.480D+09
 23.0  0.591  0.157  0.000  0.000  0.747  24.14  0.489D+09
 24.0  0.607  0.165  0.000  0.000  0.772  24.00  0.498D+09
 25.0  0.622  0.172  0.000  0.000  0.794  23.89  0.505D+09
 26.0  0.635  0.179  0.000  0.000  0.814  23.78  0.512D+09
 27.0  0.646  0.185  0.000  0.000  0.831  23.70  0.517D+09
 28.0  0.655  0.191  0.000  0.000  0.846  23.62  0.522D+09
 29.0  0.663  0.196  0.000  0.000  0.860  23.56  0.526D+09
 30.0  0.670  0.201  0.000  0.000  0.871  23.50  0.530D+09
 31.0  0.676  0.205  0.000  0.000  0.882  23.46  0.533D+09
 32.0  0.681  0.209  0.000  0.000  0.891  23.42  0.536D+09
 33.0  0.686  0.213  0.000  0.000  0.899  23.39  0.538D+09
 34.0  0.689  0.216  0.000  0.000  0.905  23.36  0.540D+09
 35.0  0.692  0.219  0.000  0.000  0.911  23.34  0.541D+09
 36.0  0.695  0.222  0.000  0.000  0.917  23.32  0.542D+09
 37.0  0.697  0.224  0.000  0.000  0.921  23.31  0.543D+09
 38.0  0.699  0.226  0.000  0.000  0.925  23.30  0.544D+09
 39.0  0.701  0.228  0.000  0.000  0.929  23.29  0.545D+09
 40.0  0.702  0.230  0.000  0.000  0.932  23.28  0.545D+09
 41.0  0.703  0.231  0.000  0.000  0.935  23.28  0.546D+09
 42.0  0.704  0.233  0.000  0.000  0.937  23.27  0.546D+09
 43.0  0.705  0.234  0.000  0.000  0.939  23.27  0.546D+09
 44.0  0.706  0.235  0.000  0.000  0.941  23.27  0.547D+09
 45.0  0.706  0.236  0.000  0.000  0.943  23.26  0.547D+09
 46.0  0.707  0.237  0.000  0.000  0.944  23.26  0.547D+09
 47.0  0.707  0.238  0.000  0.000  0.945  23.26  0.547D+09
 48.0  0.708  0.239  0.000  0.000  0.947  23.26  0.547D+09
 49.0  0.708  0.239  0.000  0.000  0.947  23.26  0.547D+09
 50.0  0.708  0.240  0.000  0.000  0.948  23.26  0.547D+09
```

10. Auxiliary Routines

MAP_UTIL_TRAPE

11. Keywords

allotriomorphic ferrite, Widmanstätten ferrite, pearlite, bainite, heterogeneous nucleation

B.2 Subroutine MAP_STEEL_NUCGB

0. Provenance of Source Code

S.V. Parker and H.K.D.H. Bhadeshia, Phase Transformations Group, Department of Materials Science and Metallurgy, University of Cambridge, Cambridge, U.K.

1. Purpose

MAP_STEEL_NUCGB calculates the heterogeneous nucleation rate per unit area for allotriomorphic ferrite nucleating at austenite grain boundaries.

2. Specification

SUBROUTINE MAP_STEEL_NUCGB(SITE, GSTAR, KTEMP, GV, SV, BI, BIFACE, BIEDGE, BICORN, HH, BOLTZ, AV)
DOUBLE PRECISION SITE,GSTAR,KTEMP,GV,SV,BI,BIFACE,BIEDGE,BICORN
DOUBLE PRECISION HH,BOLTZ,AV

3. Description

The nucleation rate per unit area is determined at three different sites on the austenite grain boundary – grain faces, edges and corners – using classical nucleation theory:

$$I_b^j = \frac{K_1^j}{a^2}\frac{k_B T}{h}\exp\left\{\frac{-(K_2^j G^* + Q)}{k_B T}\right\} \tag{B.1}$$

where a is the atomic spacing, G^* the activation energy barrier to nucleation and Q is the activation energy for self-diffusion of iron [1]. Site factors K_1^j (affecting the number of each site) and shape factors K_2^j (affecting the interfacial energy of each type of site) for the three sites are incorporated [2]. The overall grain boundary nucleation rate is obtained by summing the three rates for the individual sites:

$$I_b = I_b^f + I_b^e + I_b^c \tag{B.2}$$

4. References

1. R. C. Reed and H. K. D. H. Bhadeshia, *Mat. Sci. Tech.*, **8**, (1992), 421-435.

2. J.W. Christian, The Theory of Phase Transformations in Metals and Alloys, Part 1, 2nd edition, Pergamon, Oxford, 1965, 455.

5. Parameters

Input parameters

AV - real

AV is the Avogadro constant (mol^{-1}).

BOLTZ - real

BOLTZ is Boltzmann's constant (J K^{-1}).

GSTAR - real

GSTAR is the activation energy for grain boundary nucleation (J).

GV - real

GV is the free energy change per unit volume for nucleation (J m^{-3}).

HH - real

HH is Planck's constant (J s).

KTEMP - real

KTEMP is the temperature (K).

SITE - real

SITE is the fraction of active grain boundary sites for nucleation.

SV - real

SV is the austenite grain surface area per unit volume (m^{-1}).

Output parameters

BI - real

BI is the overall grain boundary nucleation rate per unit area (m^{-2} s^{-1}).

BIFACE - real

BIFACE is the grain boundary nucleation rate per unit area on grain faces (m^{-2} s^{-1}).

BIEDGE - real

BIEDGE is the grain boundary nucleation rate per unit area on grain edges (m^{-2} s^{-1}).

BICORN - real

BICORN is the grain boundary nucleation rate per unit area on grain corners (m^{-2} s^{-1}).

6. Error Indicators

None

7. Accuracy

8. Further Comments

None

9. Example

9.1 Program text

```
 DOUBLE PRECISION SITE,GSTAR,KTEMP,GV,SV,BI,BIFACE,BIEDGE
 DOUBLE PRECISION BICORN,HH,BOLTZ,AV
 INCLUDE 'map\_constants\_planck.f'
 INCLUDE 'map\_constants\_boltz.f'
 INCLUDE 'map\_constants\_av.f'
 READ(5,*) SITE,GSTAR,KTEMP,GV,SV
 CALL MAP\_STEEL\_NUCGB(SITE,GSTAR,KTEMP,GV,SV,BI,BIFACE,BIEDGE,BICORN,
& HH,BOLTZ,AV)
 WRITE (6,*) BI,BIFACE,BIEDGE,BICORN
 STOP
 END
```

9.2 Program data

```
1.0D-09   1.045D-19   973   -3.497D+07   3.20D+04
```

9.3 Program results

```
0.989D+10  0.989D+10  0.785D+05  0.336D+00
```

10. Auxiliary Routines

None

11. Keywords

allotriomorphic ferrite, nucleation, austenite grain boundaries

B.3 Subroutine MAP_STEEL_WIDNUC

0. Provenance of Source Code

S.V. Parker, Swinden Technology Centre, British Steel plc, Moorgate, Rotherham, S60 3AR, U.K. and Phase Transformations Group, Department of Materials Science and Metallurgy, University of Cambridge, Cambridge, U.K.

1. Purpose

MAP_STEEL_WIDNUC calculates the displacive nucleation rate of Widmanstätten ferrite and bainite.

2. Specification

SUBROUTINE MAP_STEEL_WIDNUC(WI,KTEMP,GMAX,SV)
DOUBLE PRECISION WI,KTEMP,GMAX,SV

3. Description

The activation energy barrier for displacive nucleation has been found to have a linear dependence on the chemical driving force for nucleation, unlike the case for classical nucleation theory [1]. The nucleation rate equation therefore differs accordingly. The nucleation rate per unit volume can be given by [2]:

$$I_{\alpha_b} = K_1 \exp\left\{-\frac{K_2}{RT}\left(1+\frac{\Delta G_m}{K_4}\right)\right\} \tag{B.3}$$

where K_1 is a constant expressing the density of nucleation sites as a function of austenite grain size,

$$K_1 = (\overline{L}K_1')^{-1} \tag{B.4}$$

$\overline{L}$ is the mean lineal intercept austenite grain size, $K_1' = 6.78 \times 10^{-10}$, $K_2 = 2065$ J mol^{-1} and $K_4 = 2540$ J mol^{-1}. ΔG_m is assumed to vary with the change in carbon concentration of the austenite as the transformation proceeds.

MAP_STEEL_WIDNUC calculates I_{α_b} and then divides it by S_v, the austenite grain surface area per unit volume, to obtain the displacive nucleation rate per unit area of austenite grain boundary.

4. References

1. H. K. D. H. Bhadeshia, *Bainite in Steels*, The Institute of Materials, London, (1992), 134-138

2. G. I. Rees and H. K. D. H. Bhadeshia, *Mat. Sci. Tech.*, **8**, (1992), 985-993

5. Parameters

Input parameters

GMAX - real

GMAX is the driving force for formation of a ferrite nucleus, ΔG_m (J mol^{-1}).

KTEMP - real

KTEMP is the absolute temperature (K).

SV - real

SV is the austenite grain surface area per unit volume (m^{-1}).

Output parameters

WI - real

WI is the displacive nucleation rate of Widmanstätten ferrite or bainite per unit area, I_{α_b} (m^{-2} s^{-1}).

6. Error Indicators

None

7. Accuracy

8. Further Comments

None

9. Example

9.1 Program text

```
      DOUBLE PRECISION WI,KTEMP,GMAX,SV
      READ(5,*) KTEMP,GMAX,SV
      CALL MAP\_STEEL\_WIDNUC(WI,KTEMP,GMAX,SV)
      WRITE(6,1) WI
1     FORMAT(/'Displacive nucleation rate = ', D10.3,
     & '  /m2s'/)
      STOP
      END
```

9.2 Program data

```
873 -400 3.2d+4
```

9.3 Program results

```
Displacive nucleation rate =  0.635D+08  /m2s
```

10. Auxiliary Routines

None

11. Keywords

Widmanstätten ferrite, bainite, nucleation

B.4 Subroutine MAP_STEEL_WIDSTART

0. Provenance of Source Code

S.V. Parker, Swinden Technology Centre, British Steel plc, Moorgate, Rotherham, S60 3AR, U.K. and Phase Transformations Group, Department of Materials Science and Metallurgy, University of Cambridge, Cambridge, U.K.

1. Purpose

MAP_STEEL_WIDSTART determines whether the thermodynamic criteria for the start of the Widmanstätten ferrite and bainite transformations have been satisfied.

2. Specification

```
SUBROUTINE MAP_STEEL_WIDSTART(WS,BS,CTEMP,GMAX,FPRO,FTO,IWSNUC,
IWSGROW,IWSFLAG,IBSGROW,IBSFLAG)
DOUBLE PRECISION CTEMP,FPRO,FTO,GMAX,WS,BS

INTEGER IWSNUC,IWSGROW,IWSFLAG,IBSGROW,IBSFLAG
```

3. Description

The universal nucleation function G_N, describes the free energy required to obtain a detectable degree of displacive transformation as a function of temperature [1]:

$$G_N = 3.637(T - 273) - 2540 \quad \mathrm{J\,mol^{-1}} \tag{B.5}$$

The subroutine MAP_STEEL_WIDSTART compares the driving force for the formation of a ferritic nucleus, ΔG_m, with G_N to determine if nucleation of Widmanstätten ferrite or bainite is thermodynamically possible. The subsequent development of the nucleus into either Widmanstätten ferrite or bainite is determined by the driving force available for growth, which must be sufficient to overcome the strain energies of the phases, 50 and 400 J mol^{-1}, respectively [1]. The criteria for formation of Widmanstätten ferrite or bainite are therefore:

$$\Delta G_m \quad < \quad G_N \tag{B.6}$$

and

$$\Delta G^{\gamma\rightarrow\gamma'+\alpha} \quad < \quad 50 \quad \mathrm{J\,mol^{-1}} \tag{B.7}$$

or

$$\Delta G^{\gamma\rightarrow\alpha} \quad < \quad 400 \quad \mathrm{J\,mol^{-1}} \tag{B.8}$$

where $\Delta G^{\gamma\rightarrow\gamma'+\alpha}$ is the driving force for the diffusional transformation of austenite to ferrite and $\Delta G^{\gamma\rightarrow\alpha}$ is the driving force for the diffusionless transformation of austenite to ferrite of the same composition.

4. References

1. H. K. D. H. Bhadeshia, *Acta Metall.*, **29**, (1981), 1117-1130

5. Parameters

Input parameters

CTEMP - real

CTEMP is the temperature (°C).

FPRO - real

FPRO is the driving force for the diffusional transformation of austenite to ferrite, $\Delta G^{\gamma\rightarrow\gamma'+\alpha}$ (J mol^{-1}).

FTO - real

FTO is the driving force for the transformation of austenite to ferrite of the same composition, $\Delta G^{\gamma\rightarrow\alpha}$ (J mol^{-1}).

GMAX - real

GMAX is the driving force for formation of a ferrite nucleus, ΔG_m (J mol^{-1}).

Output parameters

BS - real

BS is the bainite start temperature (°C).

WS - real

WS is the Widmanstätten ferrite start temperature (°C).

IWSNUC - integer

IWSNUC is a flag indicating if the displacive nucleation criterion is satisfied (equation B.6). IWSNUC=1 is set, IWSNUC=0 is unset.

IWSGROW - integer

IWSGROW is a flag indicating if the Widmanstätten ferrite growth criterion is satisfied (equation B.7). IWSGROW=1 is set, IWSGROW=0 is unset.

IWSFLAG - integer

IWSFLAG is a flag indicating if the Widmanstätten ferrite start temperature has been reached. IWSFLAG=1 is set, IWSFLAG=0 is unset.

IBSGROW - integer

IBSGROW is a flag indicating if the bainite growth criterion is satisfied (equation B.8). IBSGROW=1 is set, IBSGROW=0 is unset.

IBSFLAG - integer

IBSFLAG is a flag indicating if the bainite start temperature has been reached. IBSFLAG=1 is set, IBSFLAG=0 is unset.

6. Error Indicators

None

7. Accuracy

8. Further Comments

FTO can be calculated using the function MAP_STEEL_FTO1.

9. Example

9.1 Program text

```
      DOUBLE PRECISION CTEMP,FPRO,FTO,GMAX,WS,BS
      INTEGER IWSNUC,IWSGROW,IWSFLAG,IBSGROW,IBSFLAG
      READ(5,*) CTEMP,GMAX,FPRO,FTO
      CALL MAP\_STEEL\_WIDSTART(WS,BS,CTEMP,GMAX,FPRO,FTO,IWSNUC,IWSGROW,
     &IWSFLAG,IBSGROW,IBSFLAG)
      WRITE(6,1) CTEMP,WS,BS,IWSNUC,IWSGROW,IWSFLAG,IBSGROW,IBSFLAG
1     FORMAT(3F8.2,5I3)
      STOP
      END
```

9.2 Program data

```
Example 1

700 -400 -100 -200

Example 2

500 -1000 -100 -500
```

9.3 Program results

```
Example 1
               Widmanstatten ferrite start temperature = 700.00 C

700.00  700.00    0.00  1  1  1  0  0

Example 2
               Bainite start temperature = 500.00 C

500.00    0.00  500.00  1  0  0  1  1
```

10. Auxiliary Routines

None

11. Keywords

Widmanstätten ferrite, bainite

Bibliography

[1] J. S. Kirkaldy, B. A. Thomson and E. A. Baganis, *Hardenability Concepts with Applications to Steel*, ed. D. V. Doane and J. S. Kirkaldy, TMS-AIME, Warrendale, PA, (1978), 82-125

[2] J. S. Kirkaldy and D. Venugopalan, *Phase Transformations in Ferrous Alloys*, ed. A. R. Marder and J. I. Goldstein, TMS-AIME, Warrendale, PA, (1984), 125-148

[3] P. Maynier, J. Dollet and P. Bastien, *Hardenability Concepts with Applications to Steel*, ed. D. V. Doane and J. S. Kirkaldy, TMS-AIME, Warrendale, PA, (1978), 163-176

[4] R. K. Gibbs, B. A. Parker and P. D. Hodgson, *International Symposium on Low-Carbon Steels for the 90's*, ed. R. Asfahani and G. Tither, TMMMS, (1993), 173-179

[5] C. M. Sellars and J. H. Beynon, *Proc. Conf. on High Strength Low Alloy Steels*, ed. D. Dunne and T. Chandra, South Coast Printers, (1985), 142

[6] E. Anelli, M. Ghersi, A. Mascanzoni, M. Paolicchi, A. Aprile, F. Granato, G. Liguori and G. Rizzo, *HSLA Steels: Metallurgy and Applications*, ed. J. M. Gray, T. Ko, Zhang Shouhua, Wu Baorong and Xie Xishan, ASM International, (1986), 693-698

[7] M. Cohen and S. S. Hansen, *HSLA Steels: Metallurgy and Applications*, ed. J. M. Gray, T. Ko, Zhang Shouhua, Wu Baorong and Xie Xishan, ASM International, (1986), 61-71

[8] E. O. Hall, *Proc. Phys. Soc. Series*, **B64**, (1951), 747-753

[9] N. J. Petch, *J. Iron and Steel Institute*, **174**, (1953), 25-28

[10] C. M. Sellars, *HSLA Steels: Metallurgy and Applications*, ed. J. M. Gray, T. Ko, Zhang Shouhua, Wu Baorong and Xie Xishan, ASM International, (1986), 73-81

[11] F. B. Pickering, *Materials Science and Technology: Volume 7 – Constitution and Properties of Steels*, ed. R. W. Cahn, P. Haasen and E. J. Kramer, VCH Publishers, (1992), 335-399

[12] D. A. Porter and K. E. Easterling, *Phase Transformations in Metals and Alloys*, Van Nostrand Reinhold, NY, (1981)

[13] D. R. Gaskell, *Introduction to the Thermodynamics of Materials*, 3rd edition, Taylor and Francis Publishing, Washington DC, (1995)

[14] R. B. McLellan and W. W. Dunn, *J. Phys. Chem. Solids*, **30**, (1969), 2631-2637

[15] C. A. Dubé, H. I. Aaronson and R. F. Mehl, *Revue de Metallurgie*, **3**, (1958), 201-210

[16] S. M. Hodson, *MTDATA – Metallurgical and Thermochemical Databank*, National Physical Laboratory, Teddington, UK, (1989)

[17] B. Sundman, B. Jansson and J.-O. Andersson, *CALPHAD*, **9**, (1985), 153-190

[18] J. Ågren, *ISIJ International*, **32**, (1992), 291-296

[19] R. C. Reed, *The Characterisation and Modelling of Multipass Steel Weld Heat-Affected Zones*, Ph.D. Thesis, University of Cambridge, (1990)

[20] H. I. Aaronson, H. A. Domian and G. M. Pound, *Trans. Metall. Soc. of AIME*, **236**, (1966), 753-767

[21] J. R. Lacher, *Proc. Cambridge Phil. Soc.*, **33**, (1937), 528-545

[22] R. H. Fowler and E. A. Guggenheim, *Statistical Thermodynamics*, Cambridge University Press, New York, (1939)

[23] C. Zener, *Trans. AIME*, **203**, (1955), 619-630

[24] H. I. Aaronson, H. A. Domian and G. M. Pound, *Trans. Metall. Soc. of AIME*, **236**, (1966), 768-781

[25] H. K. D. H. Bhadeshia, *Metal Science*, **16**, (1982), 159-165

[26] J. S. Kirkaldy, *Can. J. Phys.*, **36**, (1958), 899, 907, 917

[27] G. R. Purdy, D. H. Weichert and J. S. Kirkaldy, *Trans. Metall. Soc. of AIME*, **230**, (1964), 1025-1034

[28] D. E. Coates, *Metall. Trans.*, **4**, (1973), 2313-2325

[29] A. Hultgren, *Jernkontorets Ann.*, **135**, (1951), 403-483

[30] H. K. D. H. Bhadeshia, *Bainite in Steels*, The Institute of Materials, London, (1992)

[31] L. Kaufman, S. V. Radcliffe and M. Cohen, *Decomposition of Austenite by Diffusional Processes*, John Wiley and Sons, New York, (1962), 313-352

[32] R. H. Siller and R. B. McLellan, *Trans. AIME*, **245**, (1969), 697-700

[33] H. K. D. H. Bhadeshia, *Metal Science*, **15**, (1981), 477-479

[34] S. S. Babu and H. K. D. H. Bhadeshia, *J. Mat. Sci. Letters*, **14**, (1995), 314-316

[35] J. R. Bradley, J. M. Rigsbee and H. I. Aaronson, *Metall. Trans. A*, **8**, (1977), 323-333

[36] J. R. Bradley and H. I. Aaronson, *Metall. Trans. A*, **12**, (1981), 1729-1741

[37] J. W. Christian, *The Theory of Phase Transformations in Metals and Alloys*, Part 1, 2nd edition, Pergamon, Oxford, (1965)

[38] R. W. K. Honeycombe and H. K. D. H. Bhadeshia, *Steels: Microstructure and Properties*, 2nd edition, Edward Arnold, London, (1995)

[39] H. K. D. H. Bhadeshia, *Progress in Materials Science*, **29**, (1985), 321-386

[40] W. T. Reynolds, M. Enomoto and H. I. Aaronson, *Phase Transformations in Ferrous Alloys*, ed. A. R. Marder and J. I. Goldstein, TMS-AIME, Warrendale, PA, (1984), 155-200

[41] H. I. Aaronson, M. Umemoto, T. Furuhara and W. T. Reynolds, *THERMEC 88*, Volume 1, ISIJ, Tokyo, (1988), 80-89

[42] M. Enomoto, *Trans. ISIJ*, **28**, (1988), 826-835

[43] J. W. Christian, *The Theory of Phase Transformations in Metals and Alloys*, Part 1, 2nd edition, Pergamon, Oxford, (1965), 418-475

[44] J. W. Christian, *ibid*, 85

[45] J. K. Lee, D. M. Barnett and H. I. Aaronson, *Metall. Trans. A*, **8**, (1977), 963-970

[46] J. W. Cahn, *Acta Metall.*, **4**, (1956), 449-459

[47] P. J. Clemm and J. C. Fisher, *Acta Metall.*, **3**, (1955), 70-73

[48] J. W. Christian, *ibid*, 455

[49] I. Tamura, *Trans. ISIJ*, **27**, (1987), 763-779

[50] R. C. Reed and H. K. D. H. Bhadeshia, *Mat. Sci. Tech.*, **8**, (1992), 421-435

[51] *"Atlas of Isothermal Transformation Diagrams of BS En Steels"*, BISRA Special Report No. 56, 2nd edition, The Iron and Steel Institute, London, (1956)

[52] C. M. Sellars, *Hot Working and Forming Processes*, ed. C. M. Sellars and G. J. Davies, The Metals Society, London, (1980), 3

[53] Y. Saito, M. Kimura, M. Tanaka, T. Sekine, K. Tsubota and T. Tanaka, *Kawasaki Steel Technical Report*, **9**, (1984), 12-21

[54] G. H. Gulliver, *J. Inst. Metals*, **19**, (1918), 145-149

[55] G. Abbruzzese, *Acta Metall.*, **33**, (1985), 1329-1337

[56] G. Abbruzzese and K. Lücke, *Acta Metall.*, **34**, (1986), 905-914

[57] E. Anelli, S. Amato and P. E. Di Nunzio, European Coal and Steel Commission (ECSC) Final Report no. 7210-EA/418 (D3.7/89), CSM, Rome, (1992)

[58] R. Priestner and P. D. Hodgson, *Mat. Sci. Tech.*, **8**, (1992), 849-854

[59] W. A. Johnson and R. F. Mehl, *Trans. Amer. Inst. Min. Met. Eng.*, **135**, (1939), 416-442

[60] M. Avrami, *J. Chem. Phys.*, **7**, (1939), 1103-1112

[61] M. Avrami, *J. Chem. Phys.*, **8**, (1940), 212-224

[62] M. Avrami, *J. Chem. Phys.*, **9**, (1941), 177-184

[63] R. F. Mehl and W. C. Hagel, *Progress in Metal Physics*, **6**, (1956), 74-134

[64] M. Takahashi, *Reaustenitisation of Bainite from Steels*, Ph.D. Thesis, University of Cambridge, (1992)

[65] N. Ridley, *Phase Transformations in Ferrous Alloys*, ed. A.R. Marder and J.I. Goldstein, TMS-AIME, (1984), 201-236

[66] M. Hillert, *Jernkontorets. Ann.*, **141**, (1957), 757-764

[67] C. Zener, *Trans. AIME*, **167**, (1946), 550-595

[68] M. Hillert, *The Mechanism of Phase Transformations in Crystalline Solids*, Institute of Metals, London, (1969), 231-247

[69] H. K. D. H. Bhadeshia, L.-E. Svensson and B. Gretoft, *Proc. Conf. on Welding Metallurgy of Structural Steels*, ed. J.Y. Koo, TMS-AIME, Warrendale, PA, (1987) 517-530

[70] M. Umemoto, A. Hiramatsu, A. Moriya, T. Watanabe, S. Nanba, N. Nakajima, G. Anan and Y. Higo, *ISIJ International*, **32**, (1992), 306-315

[71] J. W. Cahn and W. C. Hagel, *Decomposition of Austenite by Diffusional Processes*, ed. V. F. Zackay and H. I. Aaronson, Interscience Publishers, N.Y., (1962), 131-192

[72] H. K. D. H. Bhadeshia, *Acta Metall.*, **29**, (1981), 1117-1130

[73] W. Steven and A. G. Haynes, *J. Iron and Steel Institute*, **183**, (1956), 349-359

[74] H. K. D. H. Bhadeshia and J. W. Christian, *Metall. Trans. A*, **21**, (1990), 767-797

[75] A. Ali, *Widmanstätten Ferrite and Bainite in Ultra High Strength Steels*, Ph.D. Thesis, University of Cambridge, (1991)

[76] A. Ali and H. K. D. H. Bhadeshia, *Mat. Sci. Tech.*, **6**, (1990), 781-784

[77] H. I. Aaronson, P. G. Boswell and K. R. Kinsman, *Mechanical Properties and Phase Transformations in Engineering Materials*, ed. S. D. Antolovich *et al.*, TMS-AIME, Warrendale, PA, (1986), 467-473

[78] G. B. Olson and M. Cohen, *Metall. Trans. A*, **7**, (1976), 1897-1904, 1905-1914, 1915-1923

[79] H. K. D. H. Bhadeshia, *Journal de Physique*, **42(12) C4**, (1982), 443-448

[80] G. I. Rees and H. K. D. H. Bhadeshia, *Materials Science and Technology*, **8**, (1992), 985-993

[81] J. M. Oblak and R. F. Hehemann, *Transformations and Hardenability in Steels*, Climax Moly. Corp., Ann Arbor, MI, (1967), 15-30

[82] H. K. D. H. Bhadeshia and D. V. Edmonds, *Acta Metall.*, **28**, (1980), 1265-1273

[83] C. L. Magee, *Phase Transformations*, ASM, Metals Park, Ohio, (1970), 115-156

[84] R. Trivedi, *Metall. Trans.*, **1**, (1970), 921-927

[85] R. Trivedi and G. M. Pound, *J. Appl. Phys.*, **38**, (1967), 3569-3576

[86] A. Ali and H. K. D. H. Bhadeshia, *Mat. Sci. Tech.*, **5**, (1989), 398-402

[87] H. K. D. H. Bhadeshia, L-E. Svensson and B. Gretoft, *Acta Metall.*, **33**, (1985), 1271-1283

[88] H. K. D. H. Bhadeshia and D. V. Edmonds, *Metall. Trans. A*, **10**, (1979), 895-907

[89] K. W. Andrews, *J. Iron Steel Institute*, **203**, (1965), 721-727

[90] T. S. Hsu and C. Hongbing, *Acta Metall.*, **32**, (1984), 343-348

[91] H. K. D. H. Bhadeshia, *Metal Science*, **15**, (1981), 175-177

[92] G. J. Shiflet, J. R. Bradley and H. I. Aaronson, *Metall. Trans. A*, **9**, (1978), 999-1008

[93] H. K. D. H. Bhadeshia, *Metal Science*, **15**, (1981), 178-180

[94] J. C. Fisher, *Trans. AIME*, **185**, (1949), 688-700

[95] C. M. Wayman and H. K. D. H. Bhadeshia, *Physical Metallurgy*, 4th edition, eds. R. W. Cahn and P. Haasen, Elsevier, (1996), 1530-1531

[96] D. P. Koistinen and R. E. Marburger, *Acta Metall.*, **7**, (1959), 59-60

[97] S. A. Khan and H. K. D. H. Bhadeshia, *Mat. Sci Eng.*, **A129**, (1990), 257-272

(1975), 513-534

[98] G. P. Krielaart, M. Onink, C. M. Brakman, F. D. Tichelaar, E. J. Mittemeijer and S. van der Zwaag, *Zeitschrift für Metallkunde*, **85**, (1994), 756-765

[99] J. S. Kirkaldy, *Metall. Trans.*, **4**, (1973), 2327-2333

[100] T. Obara, W. F. Lange, H. I. Aaronson and B. E. Dom, *Solid→Solid Phase Transformations*, ed. H. I. Aaronson *et al.*, TMS-AIME, (1982), 1105-1109

[101] K. C. Russell, *Acta Metall.*, *17*, (1969), 1123-1131

[102] M. Enomoto, *ISIJ International*, **32**, (1992), 297-305

[103] E. H. Foo and C. H. P. Lupis, *Acta Metall.*, **21**, (1973), 1409-1430

[104] Y. Saito and C. Shiga, *ISIJ International*, **32**, (1992), 414-422

[105] K. L. Lee, J. K. Lee, K. B. Kang and O. Kwon, *ISIJ International*, **32**, (1992), 326-334

[106] M. Hillert and L. I. Staffanson, *Acta Chem. Scand.,* **24**, (1970), 3618-3626

[107] S. Nanba, M. Katsumata, T. Inoue, S. Nakajima, G. Anan and M. Umemoto, *CAMP-ISIJ*, **3**, (1990), 871

[108] M. Suehiro, K. Sato, Y. Tsukano, H. Yada, T. Senuma and Y. Matsumura, *Trans. ISIJ*, **27**, (1987), 439-445

[109] S. Denis, D. Farias and A. Simon, *ISIJ International*, **32**, (1992), 316-325

[110] Thermecmastor-Z Instruction Manual, Fujii Electronic Industrial Co. Ltd., (1986)

[111] P. H. Shipway and H. K. D. H. Bhadeshia, *Mat. Sci. Tech.*, **11**, (1995), 1116-1128

[112] *Annual Book of ASTM Standards*, **03.01**, ASTM, Philadelphia, (1989)

[113] J. W. Christian, *The Theory of Phase Transformations in Metals and Alloys*, Part 1, 2nd edition, Pergamon, Oxford, (1965), 545

[114] J. R. Bradley and H. I. Aaronson, *Metall. Trans. A*, **12**, (1981), 1729-1741

[115] A. A. Howe, F. R. Beckitt, Z. Hussain, D. Farrugia, P. M. Ingham and G. J. Watts, *Control of Microstructures and Properties of Wrought Transformable Steels*, European Coal and Steel Commission (ECSC) 7210.MA/815 (D3-F9.3/88), Final Report, British Steel plc, January 1992

[116] A. A. Howe, *Improvement of Hot-Rolled Product by Physical and Mathematical Modelling*, European Coal and Steel Commission (ECSC) 7210.EC/807 (D3.02a/94), Technical Report No. 3, British Steel plc, January 1996, Appendix 1

[117] A. A. Howe, *Improvement of Hot-Rolled Product by Physical and Mathematical Modelling*, European Coal and Steel Commission (ECSC) 7210.EC/807 (D3.02a/94), Technical Report No. 5, British Steel plc, February 1997, Appendix 2

[118] K. Hashiguchi and J. S. Kirkaldy, *CALPHAD*, **8**, (1984), 173-186

[119] R. C. Sharma, G. R. Purdy and J. S. Kirkaldy, *Metall. Trans. A*, **10**, (1979), 1129-1139

[120] M. Fourneret, *Theoretical and Experimental Investigations of the Kinetics of Pearlite Formation in Structural Steel*, Phase Transformations Group, University of Cambridge, June 1996

[121] L. C. Chang and H. K. D. H. Bhadeshia, *Mat. Sci. Tech.*, **11**, (1995), 874-881

[122] G. P. Krielaart, C. M. Brakman and S. van der Zwaag, *J. Mat. Sci.*, **31**, (1996), 1501-1508

[123] J. D. Robson and H. K. D. H. Bhadeshia, *Mat. Sci. Tech.*, **13**, (1997), 631-639, 640-644

[124] S. J. Jones and H. K. D. H. Bhadeshia, *Acta Materialia*, **45**, (1997), 2911-2920

[125] W. F. Lange III, M. Enomoto and H. I. Aaronson, *International Materials Reviews*, **34**, (1989), 125-157

[126] F. R. Beckitt, British Steel plc, private communication, June 1997

[127] R. L. Bodnar and S. S. Hansen, *Metall. Trans. A*, **25**, (1994), 665-675

[128] R. L. Bodnar and S. S. Hansen, *Metall. Trans. A*, **25**, (1994), 763-773

[129] W. Huang and M. Hillert, *Metall. Trans. A*, **27**, (1996), 480-483

[130] W. F. Lange III, M. Enomoto and H. I. Aaronson, *Metall. Trans. A*, **19**, (1988), 427-440

[131] A. Yoshie, M. Fujioka, H. Morikawa and Y. Onoe, *THERMEC-88*, Volume 2, ISIJ, Tokyo, (1988), 799-806

[132] G. R. Speich, L. J. Cuddy, C. R. Gordon and A. J. DeArdo, *Phase Transformations in Ferrous Alloys*, ed. A.R. Marder and J.I. Goldstein, TMS-AIME, Warrendale, PA, (1984), 341-389

[133] C. Ouchi, T. Sampei and I. Kozasu, *Trans. ISIJ*, **22**, (1982), 214-222

[134] B. Lopez and I. Gutierrez, *Improvement of Hot-Rolled Product by Physical and Mathematical Modelling*, European Coal and Steel Commission (ECSC) 7210.EC/807 (D3.02a/94), Technical Report No. 5, February 1997, Appendix 4

[135] M. Umemoto and I. Tamura, *HSLA Steels: Metallurgy and Applications*, ed. J. M. Gray, T. Ko, Zhang Shouhua, Wu Baorong and Xie Xishan, ASM International, (1986), 373-382

[136] A. K. Mukherjee, *Plastic Deformation of Metals*, Treatise on Materials Science and Technology, vol. 6, ed. R. J. Arsenault, Academic Press, New York, (1975), 187

[137] X. D. Liu and P. Karjalainen, *Proc. Conf. Mechanical Working and Steel Processing*, **33**, Iron and Steel Society, (1996), 769-774

[138] F. R. Beckitt, *Improvement of Hot-Rolled Product by Physical and Mathematical Modelling*, European Coal and Steel Commission (ECSC) 7210.EC/807 (D3.02a/94), Technical Report No. 3, January 1996, Appendix 4

[139] A. Sandberg and W. Roberts, *Thermomechanical Processing of Microalloyed Austenite*, ed. A. J. DeArdo, G. A. Ratz and P. J. Wray, TMS-AIME, Warrendale, PA, (1982), 405-430

[140] R. K. Amin and F. B. Pickering, *Thermomechanical Processing of Microalloyed Austenite*, ed. A. J. DeArdo, G. A. Ratz and P. J. Wray, TMS-AIME, Warrendale, PA, (1982), 377-402

[141] W. Liu, *Physical Metallurgy of Direct-Quenched Steels*, ed. K. A. Taylor, S. W. Thompson and F. B. Fletcher, The Minerals, Metals and Materials Society, (1993), 39-53

[142] M. Umemoto, H. Ohtsuka, H. Kato and I. Tamura, *Proc. Int. Conf. on Structure and Properties of HSLA Steels*, Woollongong, Australia, (1984), 107

[143] L. J. Cuddy, *Accelerated Cooling of Steel*, ed. P. D. Southwick, TMS-AIME, Warrendale, PA, (1986), 235-243

[144] L. J. Cuddy, *Metall. Trans. A*, **15**, (1984), 87-98

[145] I. Kozasu, C. Ouchi, T. Sampei and T. Okita, *Microalloying '75*, ed. M. Korchynsky, Union Carbide Corp., New York, (1976), 120-135

[146] T. Siwecki, A. Sandberg, W. Roberts and R. Lagneborg, *Thermomechanical Processing of Microalloyed Austenite*, ed. A. J. DeArdo, G. A. Ratz and P. J. Wray, TMS-AIME, Warrendale, PA, (1982), 163-192

[147] R. Benogochea, B. Lopez and I Gutierrez, submitted to Metall. Trans., 1997

[148] *Materials Algorithms Project*, http://www.msm.cam.ac.uk/map/mapmain.html